1-1-2011

Properties and biomedical applications of magnetic nanoparticles

Rajesh Kumar Regmi
Wayne State University,

PROPERTIES AND BIOMEDICAL APPLICATIONS OF MAGNETIC NANOPARTICLES

by

RAJESH KUMAR REGMI

DISSERTATION

Submitted to the Graduate School

of Wayne State University,

Detroit, Michigan

in partial fulfillment of the requirements

for the degree of

DOCTOR OF PHILOSHOPY

2011

Major: Physics

Approved by:

_____

Advisor Date

_____

_____

_____

DEDICATION

To my parents

ACKNOWLEDEMENTS

I would like to express my deepest and sincerest gratitude to my advisor, Dr. Gavin Lawes. His knowledge in broad area of research, logical way to deal with problems, and positive and encouraging attitude gave me a wonderful platform to interact with him and made my Ph.D. journey really blissful. On top of that, the courses he taught (Solid State Physics and Material Characterization) had also added great help for the Ph.D. research. Working under his outstanding supervision and great ideas lead to the present dissertation. His support and suggestions have always been rewarding for me. I am really greatly inspired from him and have learned many scientific and other things, which will certainly be a driving force for my future career. I would also like to express my deepest gratitude to Dr. Prem Vaishnava. His broad knowledge for biomedical aspects of Physics has greatly influenced me and have significant contribution to complete many research projects included in this dissertation. His guidence and sound advice have always been of great values for me. I also really appreciate his support being as a committee member. I am also deeply grateful to Dr. Paul Keyes for agreeing to be a committee member. I learned a lot of useful terms related to my research from the Soft Condensed Matter course he taught. In addition, his help to do the DLS measurement for nanoparticle samples in his lab was also really appreciable. I am also profoundly thankful to Dr. Ashis Mukhopadhyay for his approval to be a committee member. Also, I really appreciate his help to do the FCS measurement at his lab. I also earnestly thank Dr. Ratna Naik for being my previous committee

member. Her support and encouragement throughout my Ph.D. research have greatly helped me to come to this pleasant educational life time reward. My sincere thanks are also due to Dr. Jogindra Wadehra, Dr. Jhy-Jian Chang, Dr. Sean Gavin, Dr. Giovanni Bonvicini, Dr. Jagdish Thakur and all professors in the department, who directly or indirectly shaped my educational career..

Since my work was more related to biomedical application of magnetic nanoparticles, we had a great collaboration with Dr. David Oupicky at Department of Pharmaceutical Sciences, and Dr. Joseph T. Rakowski and Dr. Gilda Gali Hillman at Department of Radiation Oncology. I truly thank to Dr. David Oupicky for introducing and allowing me to do many measurements in his lab. His guidance for many biomedical applications was really appreciable. I would like to thank Dr. Shanta Raj Bhattarai at Dr. Oupicky's lab, who taught me how to run many useful instruments at his lab. My warm thanks also go to Amit Suresh Wani and Jing Li at Dr. Oupicky's lab. It gives me immense pleasure to thank Dr. Joseph Rakowski, who greatly helped to introduce the potential of magnetic nanoparticles for the application in radiation therapy. Discussion about the many aspects of radiation therapy with him was also really great. I also earnestly thank to Dr. Gilda Gali Hillman, who allowed us to use magnetic nanoparticles for the cell study in her lab. Her co-operation and many helpful discussions were also really appreciable. I also owe my thanks to Lindsay Runyan and Dr. Vinita Singh Gupta for being cooperative and doing cell study using magnetic nanoparticles. I would like to thank

Dr. Cornel Rablau from Kettering University for helping to perform light scattering experiments at his lab.

I would also like to give special thanks to Dr. Chandra thapa who helped me from the time I came to the US and has been also helping in both academia and outside academia with his best suggestion, as a brother. I also wish to thank Dr. Sudakar Chandran, Dr. Ronald J. Tackett, and Dr. Parashu Ram Kharel for helping me to learn many tools in the lab. In addition, I also like to thank Dr. Ambesh Dixit, Akila Kumarasiri, Correy Black, Vikas Gumber, David Kahn, Melissa Lavoie and Ajit Naik for sharing and being cooperative in the lab. Finally, I would like to thank my brother, Dinesh Regmi, parents and all other family members for their great help and encouragement to reach upto here.

With all the help in my life thus far, my journey has finally begun and I can now see the goal of my life – to serve those who needs my help.

TABLE OF CONTENTS

LIST OF TABLES

LIST OF FIGURES

CHAPTER 1

INTRODUCTION

1.1 BACKGROUND

The emerging area of nanotechnology includes the study of materials having a characteristic length scale less than 100 nm and their applications. One particularly exciting topic is the use of nanoscale magnetic materials for biomedical application [1]. Many interesting properties of magnetic nanoparticles have been investigated, and these studies have led to an expectation that these systems will have applications in biomedicine. Magnetic nanoparticles may be useful for these applications if they can be made biocompatible, stable, and biodegradable, possibly by coating them with suitable materials to allow them to be attached to antibodies, proteins and drugs. Generally, polysaccharides (like dextran) and polymers (like poly ethylene glycol) are used for such coating.

Magnetic nanoparticles have the potential to be delivered to a specific region in the body by applying an external magnetic field. For this use *in vivo*, one needs large magnetizations for the magnetic nanoparticles so that they respond to externally applied magnetic field at and above room temperature. Magnetite (Fe_3O_4) and Maghemite (γ-Fe_2O_3) are suitable particles for many biomedical applications, as they have bulk magnetization values of 82 emu/g and 75 emu/g respectively [2], and are relatively non-toxic [3]. Because of thermal fluctuations,

sufficiently small magnetic nanoparticles have no remanent magnetization at room temperature. This minimizes the possibility of aggregation, which could have harmful effects, and favors biological absorption and eventually the excretion of particles by the body. These particles can be prepared as isolated particles or dispersed in a carrier liquid, where they are called a "ferrofluid". We have investigated many physical properties of magnetic nanoparticles both in powder and solution form. In addition to understanding the physics of these nanoparticles, we have also investigated many biomedical applications of magnetic nanoparticles including magnetic hyperthermia, drug delivery, radiation therapy, and as a contrast agent in MRI.

1.2 MAGNETIC NANOPARTICLES

In ferromagnetic materials below the transition temperature the local magnetic moments of atoms are ordered with parallel alignment . The interactions producing this arrangement originate from the properties of the local moments and are called the *exchange interaction* [4]. This exchange from the coulomb interaction between two electrons and the fact that the wave function of two electrons must be antisymmetric under the exchange of all electron coordinates, space and spin [5]. Inside a ferromagnetic material there are a number of regions having parallel spins. These regions are called *magnetic domains*, and are illustrated in Figure 1.1.

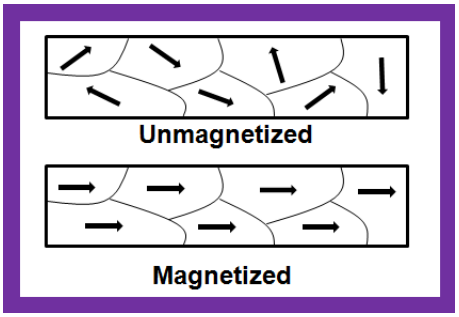

Figure 1.1: Magnetic domains

In each of these domains, a large number of atomic moments, typically 10^{12} to 10^{15}, are aligned parallel so that the magnetization within the domain is almost saturated [6]. However, the direction of this spin alignment varies from one domain to another, and will be randomly oriented in the absence of an external magnetic field. The formation of these domains is a consequence of minimizing the magnetic free energy. Magnetic domains will form in a sample until the energy cost of forming a domain wall exceeds the reduction in free energy gained from forming another domain. Domain walls are the transition region between domains, in which the local moments are not parallel but the direction of magnetization changes smoothly from one domain to another. The width of a domain wall is given by the relation [7];

$$\delta = \pi S\left[\frac{2J}{Ka}\right]^{1/2} \quad \text{.....(1.1)}$$

Where δ is width of domain wall, J is exchange integral, K is anisotropy constant, a is lattice spacing and S is the magnitude of spin. Equation (1.1) implies thatlarger

exchange interactions lead to wider domain walls, and larger magnetocrystalline energies lead to narrower domain walls.

When a ferromagnetic material containing a number of magnetic domains is magnetized with an external magnetic field, it will not relax back to zero magnetization after this external field is removed. The magnetization must be driven back to zero by applying a field in the opposite direction. If an alternating magnetic field is applied to the material, its magnetization will trace out a closed loop called a *hysteresis loop*. This irreversibility in the magnetization is called *hysteresis* and it is related to the existence of magnetic domains in the material that can be realigned in an external field. Once the magnetic domains are reoriented, it takes some external field cause a second reorientation. In a hysteresis curve (figure 1.2), the saturation magnetization (M_s) is the maximum magnetic moment per unit volume. The coercivity (H_c) is the magnitude of the magnetic field required to return the magnetization zero after being driven to saturation. The residual magnetization after removing magnetic field on it is called remanent magnetization or remanence (M_r) [8].

When the size of ferromagnetic material is decreased, a critical is size is reached, below which it is energetically unfavourable to form a domain boundary. Below this critical size, the ferromagnet exists only as single domain particles. This critical size can be estimated from the balance between the magnetostatic energy and energy to form a domain wall, which is given by [9]:

$$d_c = [9(AK_1)^{1/2}] / [2\pi M_s^2] \quad \text{.....(1.1)}$$

Here, A is the exchange constant (which is also referred to as the stiffness constant or Bloch wall coefficient), K is the magnetocrystalline anisotropy constant, and M_s is the saturation magnetization.

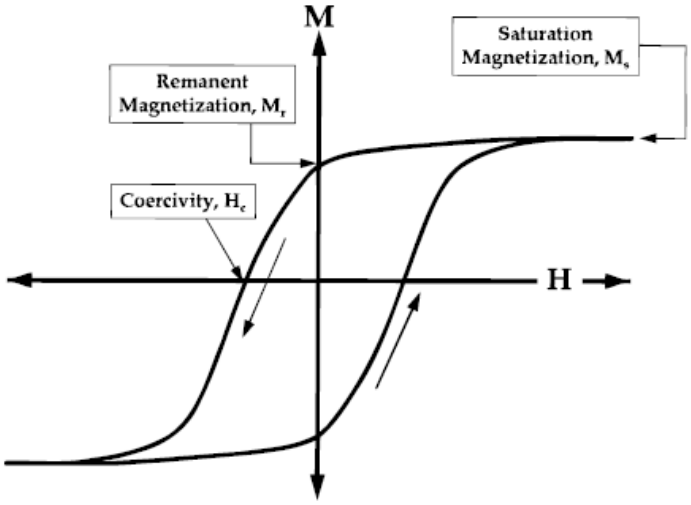

Figure 1.2: Hysteresis loop with M_s, M_r and H_c.

The value of the critical diameter is normally less than 100 nm. For example, magnetite has $d_c \sim 80$ nm and iron has $d_c \sim 12$ nm [10]. Thus, magnetic nanoparticles having a diameter on the order of a few nanometers have only a single magnetic domain. Since the individual spins in the nanoparticles are ordered ferromagnetically, they rotate coherently, leading to a single large effective moment.

Because of their crystal structures, magnetic nanoparticles have uniaxial anisotropy (or cubic anisotropy) and the magnetic moments are typically aligned

along one direction of the easy axis (or axes). The easy axis refers to the energetically favorable direction of magnetization in magnetic materials, which is determined by the crystal lattice and the interaction energies. At zero field, the actual direction of the magnetization will normally be point along one of the two directions defined by the easy axis. To change the direction of the magnetization, one has to overcome an energy barrier that is determined by the uniaxial anisotropy energy together with the external magnetic field. The energy barrier 'E_A' in the presence of external magnetic field H is given by [5]

$$E_A = V(K\sin^2\theta - MH\cos\varphi) \quad \ldots\ldots\ldots\ldots\ldots\ldots (1.2)$$

Where V is the volume of the nanoparticle, θ is the angle between magnetization and the easy axis, and φ is the angle between external magnetic field and magnetization as shown in Fig 1.3 a. In the absence of an external magnetic field, the maximum value of energy barrier is KV and a minima occurs along either of the easy axis directions (figure 1.3 b).

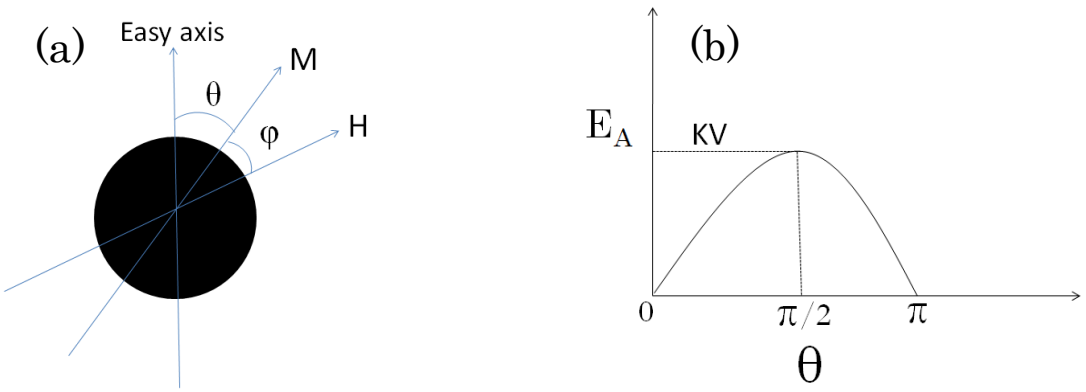

Figure 1.3: (a) Direction of easy axis, magnetization and external field in a magnetic nanoparticle (b) Energy barrier between two easy axis in a magnetic nanoparticle.

If the thermal energy K_BT is large compared to the value of the energy barrier, the direction of the nanoparticle moment can flip freely between the two directions defined by the easy axis. This leads to the moments being randomly oriented, while fluctuating, so the net magnetization is zero. This phenomenon of showing paramagnetic behavior in the magnetically ordered phase is called *superparamagnetism*. The flipping frequency of the nanoparticle moments is given by the relation:

$$f = f_0 \exp(-E_A/K_BT) \quad \ldots\ldots\ldots\ldots\ldots\ldots (1.3)$$

Where f_0 is the attempt frequency to overcome the energy barrier (E_A), having a value of ~ 10^{10} Hz. The relaxation time (τ), which is the average time it takes the system to jump from one minimum to the other, is the reciprocal of the flipping frequency (f). Typically, experimental measuring frequency is about 100 sec and at sufficiently high temperatures, f of nanoparticle moments is higher than the experimental measuring frequency because of the large thermal energy [4]. At high temperatures, no hysteresis is observed in the M-H curve, which shows superparamagnetic behaviour (figure 1.4). As the temperature is lowered, the flipping frequency (f) decreases, and a critical temperature is reached below which f becomes smaller than experimental measuring frequency. Below this temperature, the nanoparticles moments are frozen (on average), and the system shows a hysteresis loop in the M-H curve conistent with typical ferromagnetic behaviour. This critical temperature is called blocking temperature T_B.

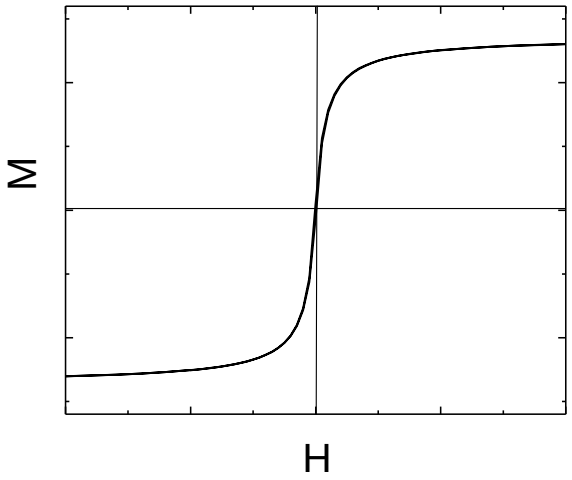

Figure 1.4: Single valued M-H curve of magnetic nanoparticles above their blocking temperature.

When a system of magnetic nanoparticles is cooled in a zero external magnetic field and the magnetization is measured on warming in a small applied field, the zero field cooled (ZFC) magnetization curve is obtained as shown in figure 1.5.

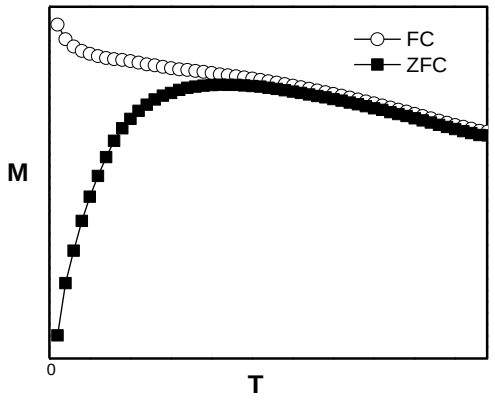

Figure 1.5: Typical ZFC and FC magnetization curves.

Starting from high temperatures, the magnetic moments of individual nanoparticles are randomly oriented because of thermal energy. When the system is cooled at zero fields, these moments are frozen in random direction blocking further reorientation below a certain temperature. This temperature is called the *blocking temperature* (T_B.). The peak of the ZFC curve corresponds to the blocking temperature. Since magnetic moments are frozen in random directions, the net magnetization is zero at sufficiently low temperatures in this ZFC curve. As temperature is increased, the moments begin to fluctuate because of increasing thermal energy, and these fluctuating moments tend to align in the direction of the external magnetic field. Above the blocking temperature the increasing thermal fluctuations tend to randomize the direction of the individual moments, so the magnetization decreases, as one observes for a conventional paramagnet. Note that the blocking temperature depends weakly on applied magnetic field, as can be inferred from Eq. (1.2).

The magnetization curve obtained by cooling a collection of magnetic nanoparticles in an applied field and then measuring the magnetization on warming in the same field is called the *field cooled* (FC) curve, as shown in Figure 1.5. In FC samples, the magnetic moment of each nanoparticle is approximately frozen along the applied field at low temperatures. The FC curve in Fig. 1.5 shows a small upturn at the lowest temperatures because of a small paramagnetic contribution to the signal. As the temperature increases, the alignment of the magnetic moments decreases as the thermal energy exceeds the anisotropy energy. Above the blocking temperature, the thermal energy is sufficient to overcome the

magnetocrystalline energy of nanoparticles. This is why both FC and ZFC curves show paramagnetic behavior ($M \propto 1/T$) above the blocking temperature.

1.3 BIOMEDICAL APPLICATIONS OF MAGNETIC NANOPARTICLES

Magnetic nanoparticles have great potential for applications in medicine. Some of the specific physical and chemical properties of magnetic nanoparticles that make them suitable for biomedical applications are: 1) they can be manipulated by non-invasive external magnetic field 2) they are superparamagnetic with no remnant magnetization 3) their surface can be easily modified to attach various molecules and surfactants 4) they are small enough to accumulate inside the living cells 5) they can be heated by applying an alternating magnetic field 6) they act as magnetic resonance imaging contrast agents and 7) iron oxide magnetic nanoparticles are biocompatible with FDA approval for use *in vivo*. With this background, magnetic nanoparticles have been used for many biomedical applications including magnetically targeted drug delivery, magnetic hyperthermia, radiation therapy, and as a contrast agent in magnetic resonance imaging (MRI).

1.3.1 DRUG DELIVERY BASED ON MAGNETIC NANOPARTICLES

In 1960, Freeman and collaborators pioneered the concept of magnetically guided drug delivery using iron nanoparticles [11]. Since this time, the idea of using magnetic nanoparticles to improve techniques for drug delivery has attracted tremendous interest. In conventional treatments, the drug is administered through

intravenous injection and then travels through the heart to be pumped all over the body [12]. As drugs are normally intended for only a small region in the body (for example, a cancerous tumor), this standard method for delivery is inefficient as it requires a larger amount of the drug and may lead to side effects on healthy systems. In order to overcome these problems, magnetically targeted drug delivery system (MTDDS) may be used to both limit the amount of drug used and deliver it to a more precisely controlled region. In MTDDS, biocompatible magnetic nanoparticles attached with drugs are injected into the blood stream, where they can be concentrated at specific locations in the body by an external magnetic field gradient at the targeted area. The drug is then released at the targeted region by some mechanism, such as changing the pH value, enzymatic action, or increasing temperature [13].

Magnetite (Fe_3O_4) and Maghemite (γ-Fe_2O_3) are the most commonly used magnetic nanoparticles for targeted drug delivery. These nanoparticles respond well to external magnetic fields because of their relatively large magnetization. Additionally, iron oxide is biocompatible and non-toxic. The force acting on a spherical magnetic nanoparticles in a magnetic field gradient is given by [14, 15]:

$$\mathbf{F} = (m.\nabla)\mathbf{B} = \tfrac{1}{2}(\chi V/\mu_0)\nabla B^2 \quad \text{.....(1.4)}$$

Where m is the magnetic moment, χ is the susceptibility and V is the volume of the magnetic nanoparticle. $\mathbf{B}$ is the external magnetic field acting on the system. At the

same time, the viscous force arising from the carrier liquid, which acts to oppose motion produced by the magnetic force, is given by stokes' law,

$$F_{visc} = 3\pi\eta d\mathbf{v} \text{.....(1.5)}$$

where d and $\mathbf{v}$ are the diameter and instantaneous velocity of the nanoparticle respectively, and η is the viscosity of suspending medium. Considering the one dimensional case, at steady state, the magnetic force and viscous force are equal which gives the velocity of nanoparticle $\mathbf{v}$,

$$\mathbf{v} = (\chi d^2/36\ \mu_0\eta)\nabla B^2 \text{ ..... (1.6)}$$

For example, taking typical values for the parameters involved in equation (1.6) including a magnetic field ~ 1T, velocity of magnetic nanoparticles of ~ 10 cm sec^{-1}, the viscosity of blood ~ 0.0028 Pa-sec, the susceptibility of magnetite ~ 650 and the diameter of magnetic nanoparticle ~ 10 nm , the magnetic field gradient required for controlling the motion of nanoparticles in vivo is approximately ~ 9.7×10^4 T m^{-1}.

1.3.2 MAGNETIC HYPERTHERMIA

Hyperthermia has the potential to be used for the treatment of malignant cancer cells. Blood flow is reduced in cancer cells, which makes them more acidic due to the formation of lactic acid [16]. These acidic tumor cells are temperature sensitive and are easily killed as the temperature is increased. Furthermore, the reduced blood flow to tumor cells limits their ability to dissipate heat. As a result, cancer cells can be eliminated by raising the local temperature between 41^0C to

45^0C at the site of tumor [17]. One of the problems associated with hyperthermia is the fact that healthy cells will generally also be killed if the temperature is increased significantly.

Different approaches for inducing hyperthermia have been developed, including: radio-frequency hyperthermia, microwave hyperthermia, whole-body hyperthermia and in vivo hyperthermia. Of these approaches, in vivo hyperthermia, in which magnetic nanoparticles are used as a hyperthermic agent, is of particular interest as these nanoparticles can be injected directly into a blood vessel and transported to the tumor site by an external magnetic field. Moreover, this localized hyperthermia is less likely to damage nearby healthy cells because tumor cells can be heated directly using embedded magnetic nanoparticles and there is a possibility of differentiating between tumor cells and healthy cells by using an antibody-antigen biological reaction. Magnetic nanoparticles generate heat in an alternating magnetic field through two relaxation mechanisms: (a) Brownian relaxation and (b) Néel relaxation. In Brownian relaxation, the whole particle rotates to align with the applied field and heat is generated because of the friction between particle and the suspending medium. The heat generation is characterized by a time constant τ_B

$$\tau_B = (3\eta V_B)/K_BT \quad \ldots\ldots\ldots\ldots\ldots\ldots\ldots\ldots(1.7)$$

Where V_B is the hydrodynamic volume (the total volume of the nanoparticle and coating in solution) and η is the viscosity of suspending medium. In Néel relaxation, the magnetic moment rotates away from the easy axis towards the external

magnetic field without any physical motion of the nanoparticle. In this case, the heat is produced by the internal magnetic viscosity opposing the change in magnetization. This heat generation is characterized by a time constant τ_N,

$$\tau_N = \tau_0 \exp(\Delta E/K_B T) \quad \text{.....(1.8)}$$

Where $\Delta E = KV$, K is anisotropy constant and V is the volume of magnetic nanoparticle. The resultant power generation by the AC magnetic field is given by [14]:

$$P = \pi \mu_0 \chi_0 H_0^2 f (2\pi f\tau) /[(1+(2\pi f\tau)^2] \quad \text{.....(1.9)}$$

Where f and H_0 are the frequency and amplitude of applied alternating magnetic field respectively, μ_0 is permeability of free space, χ_0 is the magnetic susceptibility and τ is effective time constant which is given by

$$\tau = (\tau_N \tau_B)/(\tau_N + \tau_B) \quad \text{.....(1.10)}$$

The different mechanisms associated with Néel and Brownian relaxation are shown in Figure 1.6 [14]. The heat produced from magnetic nanoparticles is usually referred in terms of specific (power) absorption rate (SAR). This quantity has units of Wg^{-1}. Mathematically, SAR is given by [18],

$$SAR = c\Delta T/\Delta t \quad \text{..... (1.11)}$$

where c is sample specific heat capacity (calculated as mass-weighted mean value of magnetic carriers and equivalent medium) and ΔT is increase in temperature in the

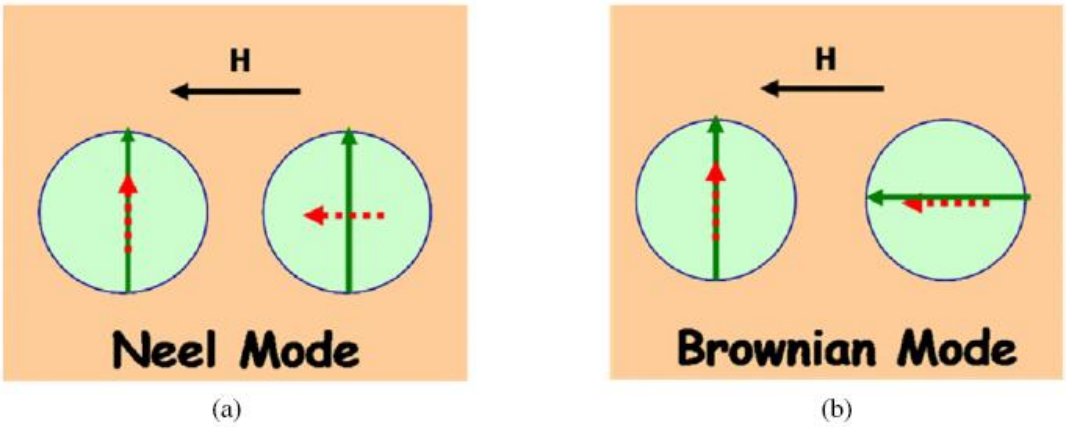

Figure 1.6: (a) Magnetic moment (dotted arrow) locked with crystal easy axis (solid arrow) rotates away from the easy axis towards the magnetic field. (b) The whole particle with magnetic moment locked with crystal easy axis moves toward magnetic field. Taken from reference [14].

time interval Δt. Since specific absorption also depends on applied field (H) and frequency (f), to compare the result with other experiment, SAR can be made independent of these quantities by dividing with the product of square of the applied field and frequency and the quantity is referred as intrinsic loss power (ILP) [19]. So, intrinsic loss power is given by,

$$ILP = \frac{SAR}{H^2 f} \quad \text{.....(1.12)}$$

1.3.3 MAGNETIC RESONANCE IMAGING

Magnetic resonance imaging (MRI) is one of the most powerful clinically used non-invasive imaging techniques, which is based on the principle that protons precess around the applied magnetic field, B, at the Larmor frequency given by;

$w = \gamma B$ ..... (1.13)

Here γ is the gyromagnetic ratio, having a value of 42.58 MHz/T for protons in water. A radiofrequency pulse is used to tip the precessing protons and they return to the original state through two relaxation mechanisms, namely, longitudinal relaxation, T_1, and transverse relaxation, T_2. T_1 and T_2 are also called spin-lattice relaxation and spin-spin relaxation time respectively. Since these relaxation times are sensitive to the local spin environment, they are used to generate bright and dark MR images.

Contrast agents are regularly used to enhance the image contrast between healthy and diseased tissue. Dipolar relaxivity ,$R_{1,2}$, the efficiency of a contrast agent that affects proton relaxation rate, is defined by [20]

$$R_{1,2} = R^0_{1,2} + r_{1,2}.C \quad \text{.....(1.14)}$$

Where $R_{1,2} = 1/T_{1,2}$ is the proton relaxation rate in the presence of contrast agent and $R^0_{1,2}$ is the relaxation rate in the absence of contrast agent . The suffix 1 and 2 correspond to the T_1 and T_2 relaxation times respectively. C is the concentration of the contrast agent and $r_{1,2}$ is the relaxivity, which measures the increase in relaxation rate per unit concentration of contrast agent. According to equation (1.14), the relaxation rate increases with an increase in concentration of the contrast agent. This allows one to correlate the observed MR signal with the concentration of contrast agents in tissue. The dipolar interaction between iron oxide nanoparticles and water proton increases the T_2 relaxation rate, which decreases the MR signal intensity producing a negative (dark) image. Iron oxide

also enhances T_2 relaxation rate because of the susceptibility effect. Susceptibility is the ratio of magnetization (M) of the substance in the presence of external magnetic field (H):

$$\chi = \frac{M}{H} \quad \text{.....(1.15)}$$

In the susceptibility effect, a magnetization difference due to the inhomogeneous distribution of magnetic nanoparticles *in vivo* produces a magnetic field gradient, which enhances the loss of phase coherence of the spins producing a dark image. In dipolar interaction, only nearby water protons interact with the nanoparticles while in the susceptibility effect, proton relaxation is affected far from the magnetic center. This makes the susceptibility effect an important mechanism to reduce T_2 relaxation time *in vivo* [20]. Iron oxide nanoparticles have an order of magnitude larger T_2-relaxivity than the gadolinium chelates currently being used for clinical applications. Iron oxide nanoparticles are also a good intravascular contrast agent since they do not leak into interstitium, unlike gadolinium chelates. Paramagnetic materials having an unpaired electron, such as gadolinium, reduces T_1 and give high intensity signal producing a positive (bright) image.

1.3.4 RADIATION THERAPY

Radiation can interact with, and damage, cells. While radiation produces ionization, there are two separate mechanisms through which radiation damages cells; direct and indirect effects. In direct effects, radiation removes the electrons

shared by base pairs of DNA. If this interaction affects enough DNA molecules, the chromosome will not be able to replicate properly, which results in the destruction of these cells. In indirect effects, radiation ionizes the water in cells to produce positively charged water molecules ($H2O^+$), which in turn gives a hydrogen ion (H^+) and a hydroxyl radical (OH*). The electron produced by the ionization of water reacts with another water molecule to give negatively charged water molecule ($H2O^-$), which further decomposes to give a hydroxyl ion (OH^-) and a hydrogen radical (H*). This hydroxyl radical may react with a hydrogen radical to form a water molecule. However, since the hydroxyl radical is very reactive, it may also react with another hydroxyl radical forming hydrogen peroxide (H_2O_2). This hydrogen peroxide is toxic and destroys the cells. Energy required for the ionization of water is 1018 kJ/mole [21] and the absorption cross-section for 500 keV photon in water is 0.1 cm^2/g. The reaction induced in the indirect effect is as follows [22]:

$$H_2O \longrightarrow H_2O^+ + e^-$$

$$H_2O^+ \longrightarrow H^+ + OH^*$$

$$e^- + H_2O \longrightarrow H_2O^-$$

$$H_2O^- \longrightarrow H^* + OH^-$$

$$H^* + H^* \longrightarrow H_2$$

$$H^+ + OH^- \longrightarrow H_2O$$

$$OH^* + OH^* \longrightarrow H_2O_2$$

The effects of radiation therapy can be localized using biocompatible metal or metal oxide nanoparticles, such as gold and iron oxide. When relatively higher energy radiation is incident on these nanoparticles, ideally accumulated inside tumor cells, they produce lower energy X-rays and auger electrons with higher linear energy transfer. Linear energy transfer (LET) is defined as energy lost per unit path traveled by particles or radiation:

$$LET = \frac{dE}{dx} \qquad \text{.....(1.16)}$$

Since these secondary X-rays and electrons have lower energy and higher absorption cross-sections, they will not travel as far as higher energy photons to damage the surrounding healthy cells.

CHAPTER 2

SYNTHESIS AND CHARACTERIZATION TECHNIQUES

2.1 SYNTHESIS

Because of the vast potential applications of magnetic nanoparticles, particularly iron oxide nanoparticles, in medicine, a number of different techniques have been developed to synthesize γ-Fe_2O_3 and Fe_3O_4 nanoparticles in a range of sizes and shapes. Modifying the Massart method of co-precipitation [23] by varying the temperature and reaction time, iron oxide nanoparticles of sizes between 4 to 10 nm can be prepared [24]. The arrested precipitation method, where a molecule added into the salt mixture acts as a growth inhibitor, is also used to synthesize nanoparticles of smaller sizes [25]. Reverse microemulsion is also used to obtain iron oxide nanoparticles of size less than 10 nm [26]. For high crytallinity and narrow size distribution, thermal decomposition of organometallic compounds is often a suitable synthesis technique [27]. As a single step preparation, laser and spray pyrolysis of vapour and aerosols have been also reported as a path for synthesizing nanoparticles [28,29]. Varying the precursor, surfactants and solvents, the high temperature decomposition method allows the production of nanoparticles in the range of 10 to 30 nm. Particles with diameters greater than 30 nm can be also synthesized by co-precipitation while controlling the ratio of ferrous and ferric salts,

and hexanediamine as a base instead of ammonium hydroxide [30]. Particles having sizes up to 300 nm can be also obtained by using the oxidizing agent KNO_3 in a mixture of water/ethanol to oxidize ferrous salt [31,32]. Using different solvents, changing the nature and concentration of precursors, and adding impurities during the synthesis can lead to particles having different shapes such as spherical, cubic, triangular, tetrahedral, and diamond [29]. However, among these many techniques for synthesizing iron oxide, we use co-precipitation because of its simplicity, and capacity to produce superparamagnetic iron oxide nanoparticles of reasonable size. Moreover, the co-precipitation technique is compatible with different approaches for functionalizing the nanoparticles with organic surfactants. We describe the co-precipitation technique in detail in the following.

2.1.1 SYNTHESIS OF Fe_3O_4 NANOPARTICLES

We synthesized iron oxide nanoparticles by co-precipitation. This is simple and efficient technique that was carried out under a fume hood at ambient conditions. $FeCl_2{\cdot}4H_2O$ and $FeCl_3{\cdot}6H_2O$ were mixed in a 1:2 molar ratio to ensure proper stoichiometry and the Fe_3O_4 nanoparticles were precipitated from solution by the addition of NH_4OH. For a typical synthesis, 10.811 g of $FeCl_3{\cdot}6H_2O$ in 40 mL of 2 M HCl was mixed with 3.976 g of $FeCl_2{\cdot}4H_2O$ in 10 mL of 2 M HCl in a 1 L beaker. After stirring the mixture with magnetic stirrer for about 5 min, 500 mL of 1 M NH_4OH was added dropwise. Initially, the solution turned brown but eventually changed to black with the formation of Fe_3O_4 nanoparticles. The resultant iron oxide nanoparticles were washed several times with de-ionized (DI)

water until the supernatant becomes neutral, which was confirmed by litmus paper. Then, in many cases, a portion of the ferrofluid sample was lyophilized to produce a powder, which is desirable for many applications. This involved freezing ferrofluid and keeping the frozen ferrofluid under very low vacuum such that ice directly convert into water vapor, which is referred to as sublimation. Since drying ferrofluid at higher temperature may change some properties of iron oxide and coating, lyophilizing ferrofluid has the advantage of preserving those properties. These iron oxide nanoparticle obtained from the co-precipitation method has particle diameters in the range of 10-12 nm. The chemical reaction can be represented by the following [33]:

$$FeCl_2 + 2FeCl_3 + 8NH_4OH \rightarrow Fe_3O_4 + 8NH_4Cl + 4H_2O \quad (2.1)$$

Iron oxides form agglomeration unless they are coated with some surfactants. Since we want to use iron oxide nanoparticles for biomedical application, we have used a number of different biocompatible surfactants to coat the iron oxide nanoparticles.

2.1.2 FATTY ACIDS COATED IRON OXIDE

Smaller diameter nanoparticles stay longer in the blood stream and have greater accumulation in the lymph nodes, which is crucial for the diagnosis of lymph nodes affected by metastases [34]. Since fatty acids have short chain length, their coating on magnetic nanoparticles makes overall hydrodynamic diameter smaller as compared long chain length polymer, which make fatty acid coated nanoparticles useful for the diagnosis of disease. In order to coat the nanoparticles

with myristic acid (MA), 2 g of the Fe_3O_4 was mixed with 2 g of myristic acid dissolved in 50 mL of acetone. This mixture was stirred for 30 minutes, rinsed with methanol and then dispersed in cyclohexane to make ferrofluid of myristic acid coated Fe_3O_4 (MA-Fe_3O_4). Since fatty acid doesn't dissolve in water we couldn't suspend fatty acid coated nanoparticles in aqueous solution. We used the same approach to coat the nanoparticles with lauric acid (LA). To coat with oleic acid (OA), we added 0.4 g of oleic acid into 275 ml of iron oxide solution synthesized in section 2.1.1 before rinsing. The solution contains about 2 g of iron oxide. The mixture was continuously stirred with a magnetic stir rod and boiled for half an hour at a temperature of 85 ^oC. The mixture was then rinsed several times until the litmus paper shows pH of the supernatant neutral. OA coated Fe_3O_4 (OA-Fe_3O_4) was also dispersed in cyclohexane to make ferrofluid. We expect that while myristic acid and lauric acid coated nanoparticles may be useful for some applications, the high temperature preparation required for oleic acid coating may be incompatible with a number of biologically relevant molecules.

2.1.3 DEXTRAN COATED IRON OXIDE

Dextran is biocompatible and its coating on iron oxide nanoparticles makes these nanoparticles long circulating without recognized by immune system of body, which makes dextran coated iron oxide nanoparticle a good contrast agent for magnetic resonance imaging. In addition, dextran is easy to functionalize and label with some optically, biologically, and therapeutically relevant molecules. In order to coat the iron oxide nanoparticles with dextran surfactant, 2 g of magnetite

nanoparticles were dispersed in 25 ml of 0.5 M NaOH and 2 g of 15-20 kDa dextran (or other molecular weight dextran) was dispersed in a separate 25 ml of 0.5 M NaOH solution. The iron oxide solution was added dropwise to the dextran solution under sonication for half an hour and the resulting mixture was left under sonication for 24 h. Dextran coated iron oxide are not stable in water. However, they are stable in 0.5 M NaOH and cell growth medium.

2.1.4 FUNCTIONALIZING IRON OXIDE TO ATTACH FITC AND TAT PEPTIDE

In many cases, it is desirable to introduce new properties to the magnetic nanoparticles by attaching different functional groups. Fluoro isothiocyanate (FITC) is a widely used fluorescent dye, frequently used for imaging in confocal microscopy [35], and tat peptide has been shown to selectively target the cell nucleus [35]. To add FITC and tat peptide to dextran coated nanoparticles, 0.5 ml of Dextran coated Fe_3O_4 nanoparticles were added to a solution containing 2.5 ml of 5 M NaOH, 1 ml of DI water and 1 ml of epichlorohydrin[36]. The mixture was incubated at room temperature for 24 h with shaking to promote the interaction between organic phase of epichlorohydrin and aqueous phase of dextran Fe_3O_4 colloid. After 24 hr of incubation, the mixture was dialyzed several times using 10 kDa cut off filters to remove the excess of epichlorohydrin. Subsequently, 1.25 ml of concentrated ammonium hydroxide was added and the mixture was left for

sonication overnight [35]. The resulting solution is amino functionalized dextran Fe_3O_4.

To label dextran coated Fe_3O_4 with FITC, 1 ml of 0.01 M FITC (10 µmol) in phosphate buffer saline (PBS) with pH 7.4 was added to 1 ml of amino functionalized dextran Fe_3O_4 [37]. The mixture was allowed to stand for 1 hr at room temperature. Excess FITC was then removed by dialysis using using 10 kDa cut off filters.

To attach tat peptide to the FITC labeled dextran Fe_3O_4, we added 90 µL of tat peptide solution in PBS (803 µM) to 110 µL of Fe_3O_4-Dex-NH_2-FITC and the mixture was allowed to react overnight at room temperature. We also tried to attach tat peptide using the heterobifunctional crosslinker N-succinimidyl 3-(2-pyridyldithio) propionate (SPDP) [32]. 50 µL of N-succinimidyl 3-(2-pyridyldithio) propionate (SPDP, 25 mM) in dimethyl sulfoxide (DMSO) was added to 60 µL of Fe_3O_4-Dex-NH_2-FITC and the mixture was allowed to stand for 1 hr at room temperature. 90 µL of tat peptide solution in PBS (803 µM) was then added to the mixture of SPDP and Fe_3O_4-Dex-NH_2-FITC and the mixture was allowed to react overnight at room temperature. However, since the tat peptide did not have a thiol group (sulfhydride), the crosslinker did not attach the tat peptide. We also attempted to attach tat peptide to amine functionalized dextran Fe_3O_4 without FITC. 50 µL of N-succinimidyl 3-(2-pyridyldithio) propionate (SPDP, 25 mM) in DMSO was added to 60 µL of Fe_3O_4-Dex-NH_2 in PBS and the mixture was allowed to stand for 1 hr at room temperature. 90 µL of tat peptide solution in PBS (803 µM)

was then added to the mixture of SPDP and Fe_3O_4-Dex-NH_2 and the mixture was allowed to react overnight at room temperature. In this case as well, the crosslinker did not attach tat peptide because of the absence of thiol group.

2.1.5 HYALURONIC ACID COATED IRON OXIDE

Hyaluronic acid (HA) is a major component of vertebrate tissue and body fluid, which has been used to target tumor cells in various nanomedicine studies [38]. In order to coat the iron oxide nanoparticles with hyaluronic acid, 80 mg of magnetite nanoparticles were dispersed in 1 ml of 0.5 M NaOH and 80 mg of hyaluronic acid was dispersed in a separate 1 ml of 0.5 M NaOH solution. The iron oxide solution was added dropwise to the hyaluronic acid solution, which was sonicated over a period of 15 minutes, with the resulting mixture being held under sonication for 24 h.

2.1.6 IRON OXIDE ADSORBED ON PNIPAM

Poly-N-isopropylacrylamide(PNIPAM) is a thermosensitive polymer which absorbs water and swells below a critical temperature, referred as lower critical solution temperature (LCST), and shrinks and releases water above LCST. This property has been used to load and release the drug from these microgels [39]. PNIPAM microgels were synthesized by a free radical polymerization technique [40]. In this process, 550 mg of N-isopropylacrylamide and 50 mg of N,N-methylenebis-acrylamide were dissolved in 40 ml of de-ionized water to which 5 ml of an aqueous solution having 250 mg ammonium persulfate (50 mg/ml) was added

as an initiator. The mixture was stirred for 15 min under a nitrogen atmosphere at a constant temperature of 343 K, which was maintained by using hot plate and oil bath. After 15 min, 5 ml of an aqueous solution with 35 mg sodium acrylate was added to increase the density of carboxylic groups to promote iron oxide nanoparticle attachment. The mixture was refluxed (condensing water vapor using cold water) under the same conditions for 4 h. After this procedure, the microgels were dialyzed in de-ionized water for two days, freeze dried, and preserved at room temperature. The microgel sample obtained after adding sodium acrylate on PNIPAM is designated as PNIPAM-SA. We mixed 467 mg of magnetite nanoparticles with 200 mg of PNIPAM-SA for 24 h using a non-magnetic stirrer to avoid promoting agglomeration. In order to increase the colloidal stability of the composite, we added 60 mg of sodium poly(styrene-sulfonate) (PSS) to the magnetic microgels and stirred the resulting mixture for 48 h at room temperature. Finally, the mixture was centrifuged, and washed several times.

2.1.7 TETRAMETHYLAMMONIUM HYDROXID COATED IRON OXIDE

Tetramethylammonium hydroxide (TMAH) coating creates negative charge on the surface of nanoparticles and makes stable ferrofluid. TMAH coating also facilitate silica coating on these nanoparticles. In addition, it may be also helpful to disperse TMAH coated iron oxide for the electron transport study where polymer coating is not needed. 280 mg of iron oxide nanoparticles synthesized in section

2.1.1 were dispersed in 10 mL stock solution of tetramethyl ammonium hydroxide (TMAH). 20 mL of DI water was then added into the mixture, which was agitated for 10 min to ensure the dispersion and stability of iron oxide nanoparticles.

2.1.8 SYNTHESIS OF Mn_3O_4 NANOPARTICLES

In addition to the iron oxide nanoparticles used for biomedical studies, we also prepare Mn_3O_4 nanoparticles for investigations on magnetodielectric coupling in nanomaterials. We used a co-precipitation method to synthesize Mn_3O_4 nanoparticles by mixing 19.8 g of $MnCl_2$ in 100 mL of HCl and de-ionized water in a 1:9 ratio. We then added 50 mL of NH_4OH drop wise to produce a light brown precipitate. We rinsed this precipitate a number of times using de-ionized water to remove any residual ions before filtering the solution and drying the sample in air for 1 hr at a temperature of 100 ^{0}C. The dried precipitate was again heated in air for 1 hr maintaining a temperature of 500 ^{0}C, at which time the powder changed to a dark brown.

2.1.9 EFFECT OF CARRIER LIQUID ON FERROFLUID

Surfactants need to be soluble in the carrier liquid to form a well dispersed ferrofluid. We had tried to disperse fatty acids (MA, LA and OA) coated iron oxide in water but the particles settled down since the fatty acids were not soluble in water. However, these nanoparticles form a stable ferrofluid in cyclohexane because MA, LA and OA are soluble in cyclohexane. In some cases, even the surfactant is soluble in the carrier liquid, it is necessary to develop some charge on the surface of

nanoparticles to ensure good solubility. Dextran is soluble in water so we initially tried to disperse dextran coated iron oxide nanoparticles in DI water but found that they settled down quickly. We then dispersed dextran coated iron oxide in 0.5 M NaOH, which created negative charge on the surface of dextran coated nanoparticles, and the particles were well dispersed in the solution because of electrostatic repulsion. Similarly, iron oxide nanoparticles labeled with tat peptide could be well dispersed in 0.01 M growth medium with pH 7.4 whereas they settled down in 0.01 M phosphate buffer saline (PBS) with pH 7.4 in few hours.

2.2 CHARACTERIZATION TECHNIQUES

We need to characterize the sample to confirm that we have prepared materials having the required properties for different applications. We have used different characterization techniques to study structure, size and composition of the samples prepared for many biomedical applications, among others. Various techniques that we used for the characterization are described in the following:

2.2.1 X-RAY DIFFRACTION

X-rays are electromagnetic radiation with the wavelength of 0.01 to 10 nm. Hard X-rays (short wavelength X-rays) have wavelength comparable to the size of atoms and can be used to probe the arrangement of atoms and molecules inside the crystalline materials. Generally, X- rays of wavelength 1.54 Å and 0.8 Å produced by Cu and Mo targets respectively are used in diffractometers. When X-rays interact with atoms of the materials, diffracted waves from different layers of atoms

interfere with one other to produce sharp maxima in the intensity if atoms are arranged periodically. The X-ray diffraction pattern gives the arrangement of atoms and structure of the crystalline solid in reciprocal space. Conditions of diffraction is given by Bragg's law [41],

$$2d\sin\theta = n\lambda \quad \text{.....(2.2)}$$

Where d is the spacing between the crystal planes, λ is the wavelength of incident X-ray beam and n is the order of diffraction. The characteristic length scale for the crystalline structure 'L' can be calculated from the diffraction peak width using the Debye-Scherrer's equation [42],

$$FWHM = \frac{0.9\lambda}{L\cos\theta} \quad \text{.....(2.3)}$$

Where FWHM is full width half maximum of the diffraction peak and θ is the diffraction angle. This neglects effects from instrumental broadening, among other effects, which limits the size determination to nanoparticles less than approximately 40 nm for the diffractometer used in this study. We used Cu Kα radiation on a Rigaku Ru2000 rotating anode diffractometer operating at a voltage of 40 kV and current of 150 mA to collect X-ray diffraction (XRD) patterns of different powder samples.

2.2.2 TRANSMISSION ELECTRON MICROSCOPY (TEM)

The transmission electron microscope (TEM) operates on the same principles as that of optical microscope but the TEM uses electrons instead of light. TEM uses

electrons as the “light source” and their much smaller wavelength make it possible to get a resolution a thousand times better than with a light microscopes. TEM can be used to see objects to the order of a few angstrom (10^{-10} m). Because of its high magnifications, TEM has been a valuable tool in medical, biological, and materials research. A "light source" at the top of the microscope emits the electrons that travel through vacuum in the column of the microscope. Instead of glass lenses focusing the light in the light microscope, the TEM uses electromagnetic lenses to focus the electrons into a very thin beam. The electron beam then travels through the specimen we want to study. Depending on the density of the material present, some of the electrons are scattered and disappear from the beam. At the bottom of the microscope the unscattered electrons hit a fluorescent screen, which gives rise to a "shadow image" of the specimen with its different parts displayed in varied darkness according to their density. We used JOEL HR TEM 2010, operated at 200 kV, to image the particles. Ferroflud was diluted using its carrier liquid and a drop of dilute solution of ferrofluid was put in the copper grid and the sample was dried before imaging. We note that this process of drying the ferrofluid can lead to some agglomeration of the nanoparticles, which is then observed in TEM images of the sample.

2.2.3 SCANNING ELECTRON MICROSCOPY (SEM)

Scanning electron microscopy is an excellent technique for characterizing the surface morphology of materials. It uses electrons instead of light to form an image. SEM has a large depth of field, which allows more of a specimen to be in focus at

one time. SEM has also much higher spatial resolution, so closely spaced specimens can be magnified to much higher levels of about 300 thousand times. Because the SEM uses electromagnets rather than glass lenses, it offers more control in the degree of magnification. A beam of electrons with 25 keV is produced at the top of the microscope by an electron gun. The electron beam follows a vertical path through the microscope, which is held under vacuum. The beam travels through electromagnetic fields and lenses, which focus the beam toward the sample. Once the beam hits the sample, electrons and X-rays are ejected from the sample. Detectors collect these X-rays, backscattered electrons, and secondary electrons and convert them into a signal that is sent to a screen, which produces the final image. We used a Hitachi S-2400 Scanning Electron Microscope to image the particles. The sample was prepared by dispersing small amount of loosely spaced particles on top of the conducting silicon wafer and the particles were lightly coated with gold to avoid charge accumulation while imaging the particles.

2.2.4 THERMOGRAVIMETRIC ANALYSIS (TGA)

Thermogravimetric (TGA) analysis is used for measuring endotherms, exotherms, and weight loss on heating or cooling [43]. Thermogravimetric analysis uses heat to force reactions and physical changes in the material under investigation. TGA provides a quantitative measurement of the mass change in a system associated with reactions and thermal degradation. TGA records the change in mass from dehydration, decomposition, and oxidation of a sample with time and temperature. Characteristic thermogravimetric curves are measured for specific

materials and chemical compounds due to unique sequence from physicochemical reactions occurring over specific temperature ranges and heating rates. These unique characteristics are related to the molecular structure of the sample. We typically used 5 to 10 mg of powder sample when running TGA analyses. The TGA instrument used for the measurement was from Perkin Elmer.

2.2.5 FOURIER TRANSFORM INFRARED SPECTROSCOPY (FTIR)

Fourier transform infrared spectroscopy (FTIR) is used to identify unknown materials, measure the quality or consistency of a sample, and determine the amount of component in a mixture. In infrared spectroscopy, IR radiation of wavelength 25 μm is passed through a sample. A portion of this infrared radiation is absorbed by the sample with the remainder passing through potassium bromide (KBr). The resulting spectrum represents the molecular absorption and transmission [44]. This makes infrared spectroscopy useful for several types of analysis, including the identification of specific materials or chemical complexes. We used approximately 1 mg of powder sample which was mixed with about 10 mg of KBr powder to make a very thin pellet for infrared spectroscopy.

2.2.6 DYNAMIC LIGHT SCATTERING (DLS)

Dynamic Light Scattering is used to determine the hydrodynamic size of particles in solution. When a monochromatic beam of light, such as a laser, passes through a solution, Brownian motion of the particles in solution causes time dependent fluctuation in the intensity of scattered light. It is possible to determine

the size distribution for a collection of nanoparticles by finding the diffusion coefficient using the autocorrelation function. The autocorrelation curve can be fit using a single exponential function, $C(\tau)=A\exp(-2\Gamma\tau)+B$, with $\Gamma=Dq^2$ [45]. The diffusion coefficient, D, is related to hydrodynamic size by the relation [46],

$$D = K_BT/3\pi\eta d \quad \text{.....(2.4)}$$

Where η is the viscosity of the medium and d is hydrodynamic diameter of the particle. Dynamic light scattering (DLS) measurements were performed using a 90 Plus particle size analyzer from Brookhaven Instrument Corporation. The system typically operates at an angle of 90° and uses a laser of wavelength 632.8 nm. We used solutions with concentrations of about 150 µg/ml for these measurements.

2.2.7 FLUORESCENCE CORRELATION SPECTROSCOPY (FCS)

FCS is minimally invasive technique used to determine the concentration, chemical reaction rate, and diffusion coefficient of fluorescently labeled molecules from the fluctuation of fluorescence signal. The concentration of the molecules should be very low, on the order of nanomolar, so that multiple particles do not contribute to the measured correlation signal. A fluorescent dye, such as fluoro isothiocyanate (FITC), rhodamine and alexa fluor, is used to label the particles. The fluorescence intensity is detected from a microscopic volume of about 10^{-15} L defined by the beam of laser light. The time dependent fluorescence intensity is quantified in terms of temporal autocorrelation function, which is related to the diffusion coefficient by the relation [47],

$$G(\tau) = \frac{G(0)}{(1+8D\tau/{\omega_0}^2)(1+8D\tau/{z_0}^2)^{1/2}} \quad \text{.....(2.5)}$$

with G(0) the autocorrelation at t=0, ω_0 is the (half) width in lateral direction, and z_0 is the (half) length in the axial direction of the laser focus. From the diffusion coefficient, we can calculate the hydrodynamic diameter of the particles using the relation (2.4).

2.2.8 SUPERCONDUCTING QUANTUM INTERFERENCE DEVICE (SQUID)

A magnetometer is used to measure magnetization as a function of magnetic field and temperature, which gives the insight of magnetic properties of materials. Using a Josephson junction, a superconducting quantum interference device (SQUID) can measure extremely weak magnetic signals. A Josephson junction is made up of two superconductors, separated by thin normal layer. A direct current (DC) SQUID consists of two Josephson junctions in parallel so that electrons tunneling through the junctions demonstrate quantum interference, dependent upon the strength of the magnetic field within a loop. Schematic diagram of DC Josephson effect is shown in Fig 2.1. DC SQUIDs show a large change in response to even tiny variations in a magnetic field. We used both powder and liquid sample for the magnetic measurement. We put about 20-30 mg of powder sample into a gel capsule which is further packed by cotton to avoid any motion of particles inside the capsule. We keep this capsule inside the drinking straw at fixed distance so that the

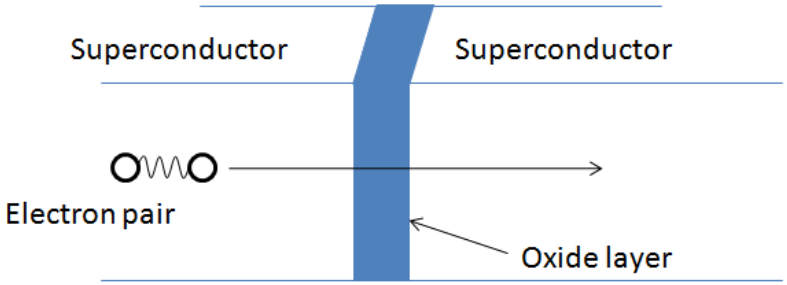

Figure 2.1: Shematic diagram of DC Josephson effect.

sample centers well during the measurement. The gel capsule is also fixed inside the straw by sewing with nylon thread to avoid any motion during the measurement. Since liquid dissolves gel capsule, we make epoxy capsule by mixing stycast 1266 part A and B in 100:28 ratio by weight. After curing the mixture of epoxy in drinking straw, we cut about 1 cm of epoxy and drill a hole to load the liquid sample, which is further sealed by epoxy cap to avoid any leakage of ferrofluid. Loading the epoxy capsule into the straw for the measurement is same as we do for gel capsule.

2.2.9 PHYISCAL PROPERTY MEASUREMENT SYSTEM (PPMS)

Physical property measurement system (Quantum Design) is a multifunctional device which is used for the measurement of specific heat, AC and DC magnetization, and electric and thermal transport in the temperature range from 1.8 to 400 K with magnetic fields up to 9 T. The PPMS consists of a cryostat unit having superconducting magnetic coil. Different sample holders can be

mounted in the cryostat for different measurements, which can be controlled by proprietary software. The PPMS can detect AC and DC signal upto 10^{-8} and 10^{-5} emu. We used the system for different measurements including AC magnetization, DC magnetization, specific heat capacity, and temperature and field sweep for dielectric measurements. We used both liquid and solid samples for various characterization using PPMS.

2.2.10 RAMAN SPECTROSCOPY

Raman spectroscopy is the technique in which the frequency of incident photon of monochromatic light changes due the inelastic scattering with local modes in the sample. Local modes may be both phonons and magnons. Phonons are the quanta of vibration energy of atoms in crystal lattice whereas magnons are the excitation of spins wave. In case of an interaction with these local modes, the reemitted light can have a higher or lower frequency than the incident photon, which is called the Raman effect [48]. The spectrum for the energy-shifted scattered light gives the information about the vibrational and rotational transition in the molecule or phonons in the crystal. In many cases, the scattered light may not have also any change in frequency (elastic scattering), which is referred as Rayleigh scattering, which does not give information about the molecule. Raman scattering is non-invasive technique having very weak effect (10^{15} times smaller than Rayleigh scattering), which has very useful application in studying phase transition in crystal, investigating defect in crystal, measuring stress, and fingerprinting molecules. Since the impurities introduced into the crystal change the vibration

modes of phonons which is detected very well in Raman Spectrocopy and is also better techniques to detect defects in crystal as compared to XRD. We used solid samples by making the pellet to collect Raman spectra. Ar+ ion-laser (514.5 nm) with a Triax 550 detector was used to collect the Raman spectra.

2.2.11 MÖSSBAUER SPECTROSCPY

Mössbauer spectroscopy is a technique that has been used in different area of Physics, Chemistry, Biology and Metallurgy and is based on the Mössbauer effect. When atoms are fixed in a crystal lattice, the emission and absorption of gamma radiation due to the transition in nuclear ground and excited state is recoil free because of the coupling to the entire mass of the crystal. This allows one to investigate the hyperfine structure of nuclear energy levels and different valence state of elements. Source, sample, detector and a drive to move the source or absorber, are the basic component in the Mössbauer spectroscopy instrument. Generally, source is moved toward the sample to shift the energy level. For example, ^{57}Fe source moving toward a sample with a velocity of 1 mm/sec increases the emitted photon by ten natural linewidths. Mössbauer spectra are described by the isomer shift (δ), quadrupole splitting (Δ) and hyperfine splitting. The isomer shift is related to the difference in energy of absorber and source, which arises from the difference in electron density at the nucleus. Quadrupole splitting is caused by the interaction between the nuclear quadrupole moment and electric field gradient produced by nearby electron. This results the splitting of individual peak into doublet in the absorption spectrum. The isomer shift moves the resonance

absorption away from zero velocity while the quadrupole splitting introduces a separation between the two component peaks of the absorption doublet. Isomer shift and qudrupole splitting are generally evaluated with respect to reference material. In magnetic materials, due to the presence of magnetic field at nucleus, hyperfine splitting occurs and produces sextet pattern, as the hyperfine energy levels depend on the quantum numbers of the Fe ions. The combination of isomer shift, quadrupole splitting and hyperfine field is sufficient to provide information about site occupancy and valence state of Fe atom. Since Mössbauer parameters are temperature sensitive, measurements at lower temperatures can provide better peak resolution. We used a solid sample of about 70 mg to obtain the Mössbauer spectra at 78 and 300 K as described in section 3.3.1.

CHAPTER 3

PHYSICAL PROPERTIES OF NANOPARTICLES IN SOLUTION

3.1 INTRODUCTION

Because superparamagnetic iron oxide nanoparticles have potential technological [49] and biomedical [1] applications, it is of great importance to understand the static and dynamic magnetic behavior of these nanoparticles dispersed in carrier liquid. To make iron oxide nanoparticles well dispersed in solution, the surface of these nanoparticles needs to be sterically stabilized by coating with a suitable organic or inorganic surfactant. The hydrodynamic size, which is the size of core and surfactant layer together, plays an important role for biomedical applications of these nanoparticles. The hydrodynamic size of the coated nanoparticles is typically determined by estimating the diffusion constant of the system in solution and then relating this to the particle size through the Stokes Einstein relation [50]. A number of techniques, including dynamical light scattering (DLS) and fluorescence correlation spectroscopy (FCS) can be used to determine the diffusion constant in solution [51,52]. Other approaches can also be used to estimate the hydrodynamic size, including using magnetic susceptibility to measure the relaxation time in a particular solvent [53]. All of these techniques consider only single particle effects, since the threshold concentration for changes in the effective

viscosity is larger than that typically considered in ferrofluids [54]. This also assumes that magnetic interactions can be neglected, which is reasonable as dipolar interactions will be very weak for dilute solutions.

In some previous studies, the hydrodynamic diameter estimated using DLS significantly exceeds the expected size. A factor of two difference was found between the hydrodynamic diameter of octadecyltrichlorosilane coated nanoparticles determined using DLS measurements, approximately 90 nm, and the diameter estimated from atomic force microscopy studies, 54 nm, with the difference being attributed at least in part to solvents [55]. In another study, 10 nm magnetite nanoparticles coated with polydimethylsiloxane were found to have a diameter of 53 nm using DLS, while theoretical calculations based on chain extension predict a size of 28 nm [56]. These results have important implications for measurements of particle size, as having accurate particle size information is crucial for determining the suitability of different polymer coated nanoparticles for specific applications. In order to address this point, we have measured the hydrodynamic diameter of Fe_3O_4 nanoparticles coated with a monolayer of dextran in solution using different techniques and compared these results together with other estimates for the particle sizes.

Since the surfactant coating also changes charge, functionality, reactivity of the nanoparticles, and can enhance the stability and dispersion of nanopaticles in carrier liquid, it is also important to investigate other effects of surfactant coatings including magnetohydrodynamic response. Surface coating with dextran [57],

deoxyribonucleic acid (DNA) [58], yeast alcohol dehydrogenase (YADH) [59], polyethyleneglyocol (PEG) [60], silica [61], polyvinyl alcohol (PVA) [62], heparin [63], phospholipids [64] and alkyl phosphonate/phosphate [65] on iron oxide nanoparticles can improve their biocompatibility for in-vivo applications. Numerous investigations have been reported on the effects of surface coatings on the magnetic properties of the nanoparticles. Fu et al [66] found no significant effect on the coercivity or blocking temperature of Fe_3O_4 nanoparticles coated with lauric acid or decanoic acid. However, for 6 nm Fe_3O_4 nanoparticles coated with gold [67], the blocking temperature increased from 80 K to ~130 K when the particles were coated with methoxypolyethylene glycol (MPEG). The difference in the blocking temperature was attributed to the interaction between the iron oxide nanoparticles and the polymer coating.

The saturation magnetization of Fe_3O_4 nanoparticles coated with oleic acid can exhibit an anomalous temperature dependence, believed to be caused by the modification of the superexchange interaction between the iron ions from the surface layer of the nanoparticles in presence of the surfactant [68,69]. There has, however, been limited work on investigating the effects of the surface coating thickness on the magnetohydrodynamic and Brownian relaxation mechanism of magnetic nanoparticles. In one recent study, Vekas et al [70] have examined the stability of magnetite nanoparticles coated with surfactants of different chain lengths, such as lauric acid, myristic acid, dodecyclbenzene sulphonic acid, and oleic acid dispersed in transformer oil and water. It was found that the oleic acid

surfactant with 18 carbon atoms and a double bond was more effective in producing a stable dispersion than the shorter chain length surfactants such as lauric acid (12 carbon atoms) and myristic acid (14 carbon atoms). The thickness of the surfactant molecules will modify the hydrodynamic radius of the nanoparticles, and is expected to play an important role in determining the ac magnetic response of the system. The loss component of the magnetic susceptibility in ferrofluids depends strongly on both Brownian relaxation, with the entire nanoparticle rotating in the carrier liquid, and on Néel relaxation, with the magnetic moment of the nanoparticle reversing direction with no physical rotation of the nanoparticle. These relaxation mechanisms depend on the size of the magnetic nanoparticles (Néel) or on the hydrodynamic size of the coated nanoparticles (Brownian). Additionally, the magnetohydrodynamic response of ferrofluids to external dc magnetic fields, which leads to chain formation, depends strongly on both the size of the magnetic nanoparticle core as well as the overall hydrodynamic size.

Within this framework, preparing nominally identical Fe_3O_4 nanoparticles coated with surfactants having different chain lengths would allow the effects of Brownian relaxation to be distinguished from the effects of Néel relaxation. The similar Fe_3O_4 core size would ensure similar Néel relaxation behavior, while the Brownian relaxation, which depends on hydrodynamic radius, would lead to a different ac magnetic response in the nanoparticles. With these motivations in mind, we studied magnetohydrodynamic response of luaric acid (LA), myristic acid

(MA) and oleic acid (OA) coated Fe3O4 nanoparticles in the presence of both AC and DC magnetic field.

Another interesting property of magnetic nanoparticles in solution is that they produce heat in the presence of alternating magnetic field through Néel and Brownian relaxation, which is referred as *magnetic hyperthermia*. While majority of studies on magnetic nanoparticle hyperthermia have been targeting biomedical applications [71-74], as heating neoplastic cells to 41-45 ^{o}C can produce the preferential death of cancer cells, there are a number of other intriguing possibilities, including magnetically controlled curing of epoxies [75] and the selective heating of nanoparticles for catalysts in synthesis reactions [76]. Furthermore, the mechanisms expected to contribute to magnetic heating have well-defined temperature dependences, so it is important to experimentally investigate temperature dependent magnetic hyperthermia in order to test these specific models.

The relaxation of nanoparticle magnetic moments in a liquid ferrofluid, responsible for heat generation in magnetic nanoparticles exposed to ac magnetic field, occurs through two primary mechanisms; Néel and Brownian relaxation. Both of these relaxation mechanisms occur concurrently, but independently, in liquid suspensions of nanoparticles, but only Néel relaxation persists for nanoparticles embedded in a rigid matrix, including a frozen solid. A number of studies have explored the Néel and Brownian relaxation mechanisms near room temperature by studying the magnetic response for nanoparticles samples in liquid and solid

matrices [77-79]. Typically, the Néel relaxation is investigated by restricting Brownian relaxation using epoxy, wax, or similar agent to eliminate nanoparticle motion. While there is considerable interest in understanding the details of magnetic hyperthermia in nanoparticles, the majority of studies, both theoretical and experimental, have focused on exploring the dependence of magnetic heating on particle size [80,81] and frequency [82]. Rosensweig has theoretically investigated the heating rate as a function of both particle size and viscosity in great detail [80], while Seehra and coworkers have demonstrated that the magnetic susceptibility of 3 nm and 9 nm FePt nanoparticles, directly affecting the magnetic heating, depends strongly on particle size [81]. Studies by Lacroix and co-authors on FeCo nanoparticles on magnetic losses in the frequency range from 2 kHz to 100 kHz have explored the frequency dependence of the magnetic heating [82].

Our investigations on the temperature dependence of the magnetic heating complement these earlier studies, and provide an additional check on the underlying validity of the magnetic relaxation models. These studies are particularly relevant given the recent interest in testing the range of validity for the Néel relaxation model [83]. Our work aims to explore the effects of magnetic hyperthermia on frozen ferrofluids and to investigate the temperature dependence of the Néel, present in both the solid and liquid states, and Brownian, present in only the liquid state, relaxation mechanisms.

3.2 DEXTRAN COATED IRON OXIDE NANOPARTICLES

Dextran is a long chain polysaccharide made up of glucose units. The molecular weight of dextran varies from 1 kDa to 2000 kDa. Dextran is neutral, easily soluble in water, stable, biocompatible, and biodegradable. It can be functionalized with many charged groups, such as amine and carboxylic groups to attach biological entities including drugs, fluorescent dyes, and peptides. Dextran is used clinically for replacing lost blood, plasma substitution, as a volume expander in anemia, in solutions for storing organs for transplantation, and as a carrier for vaccines, among other applications [84]. Dextran is also used as a starting and intermediate reagent for the wide range of synthesis in biotechnological and technical industries, including in the photographic industry to improve the quality of silver emulsions of photograph. Because of biocompatibility, ease of functionalization, freedom to choose different molecular weight, and wide ranges of applications, we chose dextran to coat the iron oxide nanoparticles. These dextran coated nanoparticles were used to determine the hydrodynamic size by different techniques, such as, dynamic light scattering (DLS), fluorescent correlation spectroscopy (FCS) and AC magnetization measurements. This allowed us to investigate which technique of determining hydrodynamic size gives theoretically expected hydrodynamic size. We also used the dextran coated nanoparticles to investigate the magnetic heating in both frozen and liquid ferrofluid to investigate the behavior of magnetic heating with temperature.

3.2.1 EXPERIMENTAL DETAILS

Dextran coated iron oxide nanoparticles were synthesized as described in section 2.1.3. We used different chain lengths of dextran, 5 kDa, 15-20 kDa, 60-90 kDa and 670 kDa, to coat the iron oxide nanoparticles and dispersed these dextran coated iron oxide nanoparticles in 0.5 M NaOH. The crystalline structure and size of the iron oxide nanoparticles was determined from X-ray diffraction patterns collected using Cu *Ka* radiation on a Rigaku Ru2000 rotating anode diffractometer. Transmission electron microscope (TEM) images were also taken using a JOEL HR TEM 2010 operating at 200 kV to confirm the core size of the nanoparticles. Dynamic light scattering on a 90 Plus particle size analyzer from Brookhaven Instrument Corporation was used to estimate the hydrodynamic size of the nanoparticles. For the FCS measurement, 15-20 kDa dextran coated iron oxide was crosslinked with epichlorohydrin, aminated and labeled with fluorescein isothiocyanate (FITC) as described in section 2.1.4. For the hyperthermia measurements, we used the set up shown in Figure 3.1. This hyperthermia apparatus, shown in figure 3.1, consists of a parallel LC tank circuit, with a capacitor having a capacitance of 0.02 μF and coil made from 1/8" Cu tubing having an inductance of 8 μH. Though the current passing into and out of the tank circuit is small, the current inside the parallel LC circuit is high because of the reactive current, which is an advantage of this configuration as compared to a simple series LC circuit. Since the current coming out of the system is small because of the

cancellation of the reactive current passing in opposite directions through the inductor and capacitor, it also avoids the use of a high power resistance and larger

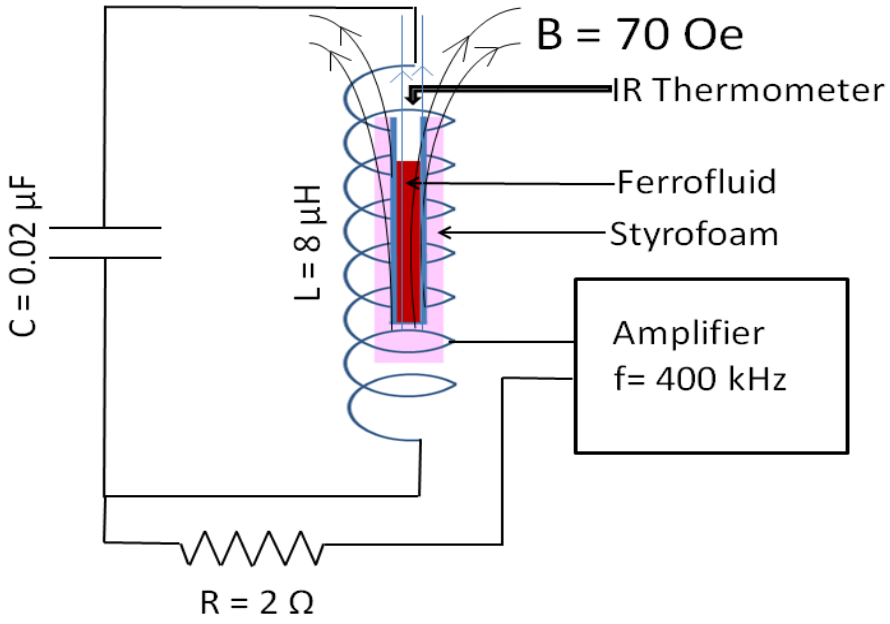

Figure 3.1: Magnetic hyperthermia set-up.

heat sink as required for a series LC circuit. Since the magnetic field is directly proportional to the current flowing through the coil, higher currents gives higher magnetic fields, which are desirable for most applications.

We used the RF generator model CLX-2750 from COMDEL, which can deliver a power of 2500 W. We used only 200 W of delivered power, which gave a current of roughly 18 A through the coil, which was measured using the mutual inductance to a separate pick-up coil, producing an alternating magnetic field of 70 Oe. If the circuit is not in resonance, the amplifier is unable deliver the required power because of the impedance mismatch. In order for the tank circuit to be on

resonance, we had to connect the power supply to the proper tapping point on the coil, as illustrated in Figure 3.1. The circuit was in resonance at about 395 kHz, which was the operating frequency for the hyperthermia measurements discussed in this work. Since a relatively high current was passing through the coil, we used a small pump to flow water continuously through the copper tubing to provide cooling. This also served to minimize possible radiative heat transfer from the coil to the sample. For the hyperthermia measurements on frozen and liquid ferrofluid, we used 10 ml of ferrofluid in a plastic vial having a diameter and height of about 2 inches. The vial was also insulated with cotton padding and styrofoam to minimize the heat exchange with environment. We used liquid nitrogen to freeze the sample, but started measurements only at– 45 ^{o}C. The sample was kept inside the coil and rise in temperature of the ferrofluid in the presence of alternating magnetic field was measured by IR thermometer from Extech Instruments. This thermometer was positioned to ensure that the beam area covered the largest possible fraction of the top surface of the sample, without impinging on the walls of the container. In practice, this corresponded to a distance of approximately 8.5" above the sample.

3.2.2 RESULTS AND DISSCUSSIONS

The results of the structural and magnetic characterizations on the dextran coated iron oxide nanoparticles are shown in Fig 3.2. Figs 3.2 a, b, c and d show the X-ray diffraction patterns, TEM images, thermogravimetric analysis (TGA) curve and the room temperature magnetization curve of the dextran coated Fe_3O_4 nanoparticles

respectively. From TEM images, diameter of the iron oxide nanoparticles is 12 nm with standard deviation of 2 nm .

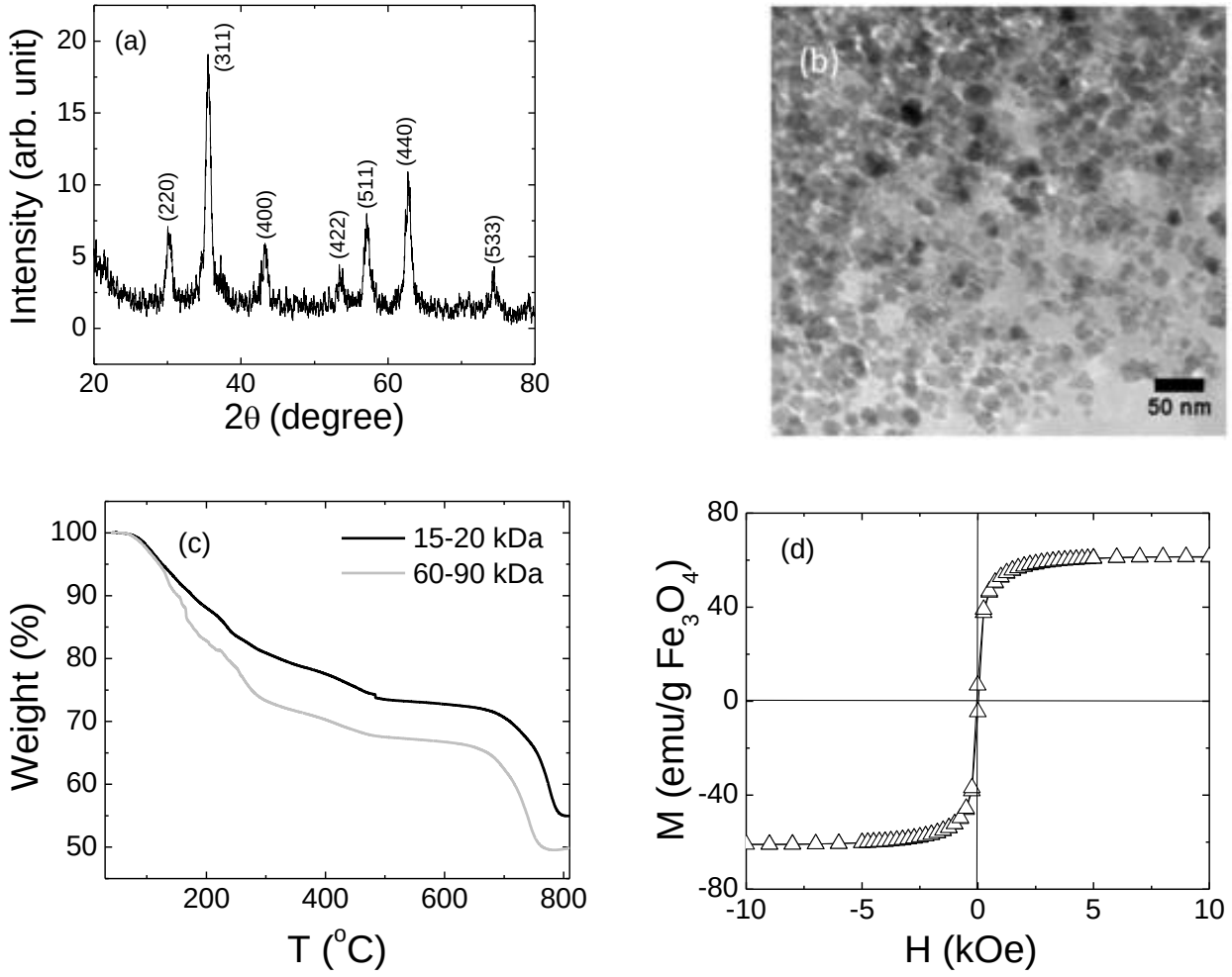

Figure 3.2: (a) X-ray diffraction spectrum of freeze dried 15-20 kDa dextran Fe_3O_4 (b) TEM images of 15-20 kDa dextran coated Fe_3O_4 nanoparticls (c) Thermogravimetric analysis data for the 15-20 kDa and 60-90 kDa molecular mass dextran coated nanoparticles and (d) room temperature M(H) curve of 15-20 kDa dextran dextran coated Fe_3O_4 ferrofluid.

Thermogravimetric analysis (TGA) on 15-20 kDa and 60-90 kDa dextran coated samples showed single step sharp drop in weight close to 770 °C and 730 °C respectively, providing evidence that there is a monolayer coating on these samples

[85]. Previous reports suggest that two sharp transitions should be seen in TGA for bilayer polymer coatings [86]. There was a weight loss of 45 % and 50% for the 15 - 20 kDa and 60 – 90 kDa dextran coated sample respectively, consistent with the lower molecular mass polymer making a smaller contribution to the total mass of the composite. We also expect the geometry of these polymer coated nanoparticles to depend on the molecular mass of the coating. The XRD peaks can be fully indexed to the Fe_3O_4 crystal structure, with no evidence for impurity phases. Transmission electron microscopy images show the core. Since lower molecular weight dextran, up to approximately 10 kDa, is known to extend linearly in solution while higher molecular weight dextran is coiled [87], the geometry of lower and higher molecular weight dextran coated sample are expected to differ. These nanoparticles have single valued M (H) curves at room temperature and exhibit separation between ZFC and FC curves with a peak in the FC magnetization curve, showing they are superparamagnetic. The saturation magnetization of these nanoparticles is about 61 emu/g of Fe_3O_4. This is smaller than the saturation magnetization for bulk Fe_3O_4, 93 emu/g, but consistent with other studies on iron oxide nanoparticles, which typically show smaller magnetizations than bulk [88].

Since the hydrodynamic size of the nanoparticles is crucial for both magnetic heating as well as biomedical application, we determined hydrodynamic size of different chain length dextran coated sample using a number of different techniques including dynamic light scattering (DLS), AC magnetization, and fluorescent correlation spectroscopy (FCS). For dynamic light scattering, to give

enough scattering of light but avoid the agglomeration of nanoparticles, we diluted the original solution by 1:250, giving a volume fraction of nanoparticles ϕ=0.2% in the solution.

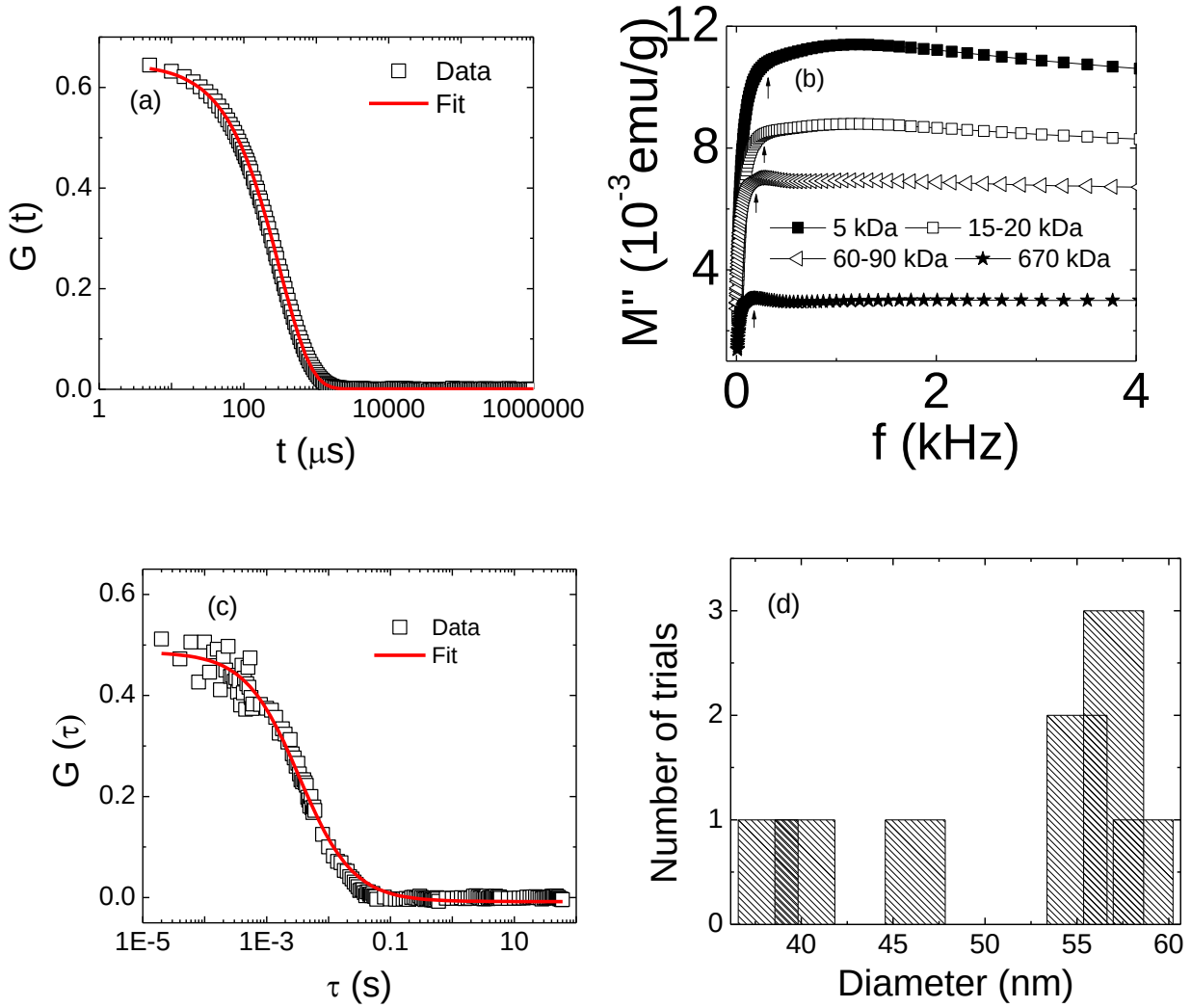

Figure 3.3 (a) Autocorrelation curve measured using DLS for 5 kDa dextran coated sample. The dashed line is the fit to an exponential function having a single exponent. (b) Imaginary part of the ac magnetic susceptibility as a function of frequency for the different chain length dextran coated sample. The arrow indicates the peak in magnetic relaxation associated with Brownian relaxation. (c) Representative correlation curve measured for a 15-20 kDa dextran coated nanoparticle measured using FCS. (d) Histogram showing the frequency distribution of nanoparticle sizes using repeated FCS measurements.

The DLS system was calibrated before doing the measurement by using polystyrene beads of know size of about 10 nm suspended in water. This helped to to rule out any possibility of instrumental error. A representative curve for the 5 kDa dextran coated sample, with DLS data and fit of single exponential function, $C(\tau)=Aexp(-2\Gamma\tau)+B$, where $\Gamma=Dq^2$, is shown in Fig 3.3a. This autocorrelation curve fit, using a refractive index 1.34 for the 0.5 M NaOH solution [89], gives the diffusion constant D. From this, we calculated the hydrodynamic diameter of the nanoparticles using the Stokes-Einstein equation [90]:

$$D=\frac{k_B T}{3\pi\eta d} \quad \text{.....(3.1)}$$

This considered a viscosity of η=0.96 cp, for the NaOH solution at room temperature, T=298 K. We found the hydrodynamic diameter of 5 kDa dextran coated sample to be 91 nm. Similar analysis on higher chain length dextran coated sample gave sizes up to 132 nm. The DLS sizes for different chain length dextran coated sample are shown in Fig. 3.4, which also includes the sizes estimated using different techniques, as discussed in the following. Because the relaxation rate for particles depends on the hydrodynamic radius, the size of magnetic nanoparticles can also be indirectly determined from the magnetic loss. For these AC magnetic susceptibility measurement, we sealed 37 mm^3 of as-prepared solution in epoxy capsules for each of the different chain length dextran coated samples, and measured the out of phase component of the magnetic response as function of

frequency at room temperature, using Quantum Design PPMS equipped with the ACMS option. These curves are shown in Fig 3.3b.

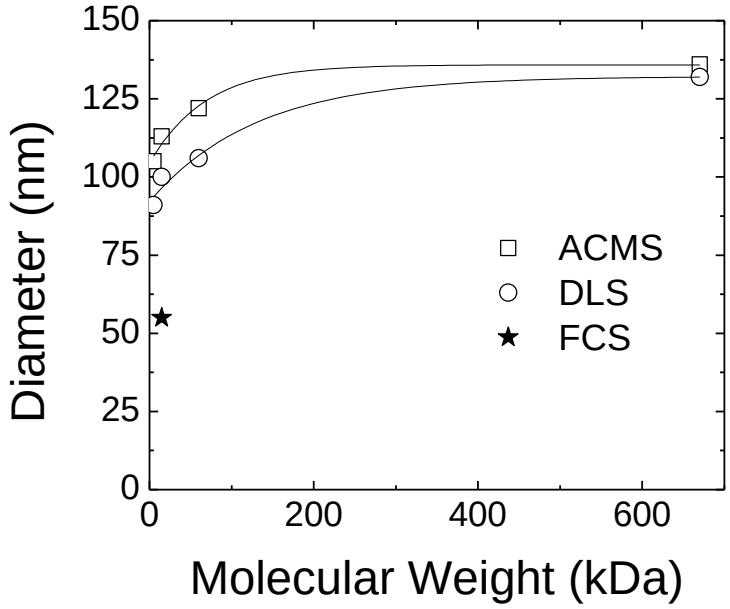

Figure 3.4. Hydrodynamic size for the dextran coated nanoparticles as determined using dynamical light scattering (DLS) and ac magnetic susceptibility measurements (ACMS) as a function of the molecular weight of dextran. The fluorescence correlation spectroscopy (FCS) measurement on the single representative 15-20 kDa dextran coated nanoparticle sample is shown as the open star for comparison. The solid lines show a decaying exponential fit to the data.

The relaxation peak corresponding to Brownian relaxation, where $\omega\tau_B=1$, is shown by arrow. Brownian relaxation is related with the hydrodynamic size of the nanoparticles by following relation:

$$\tau_B = \frac{\pi\eta d^3}{2k_B T} \quad \text{.....(3.2)}$$

Again, using the viscosity of 0.5 M NaOH, η = 0.96, we found a hydrodynamic diameter of 105 nm to 132 nm for 5 kDa to 670 kDa dextran coated sample

respectively, consistent with the size obtained from DLS measurement. These values are also potted in Fig 3.4.

As a final check on the hydrodynamic size of the nanoparticles, we did FCS measurement on the FITC labeled 15-20 kDa dextran coated sample, with volume fraction of ϕ=0.004%. This is 50 times more dilute than the sample used for DLS and magnetization measurement. We require such dilute solutions for FCS studies to ensure that only a single nanoparticles is in the focus of the laser. A representative curve of autocorrelation function, G(τ) as a function of time (τ) is shown in Fig. 3.3 (c). We fit these data to the equation [47]:

$$G(\tau) = \frac{G(0)}{(1+8D\tau/\omega_0{}^2)(1+8D\tau/z_0{}^2)^{1/2}} \quad \text{.....(3.3)}$$

We note that the autocorrelation function is related to the diffusion coefficient D, which in turn depends on the hydrodynamic size of the nanoparticle. In equation (3.3), G(0) is the autocorrelation at τ=0, ω_0 is the (half) width in lateral direction, and z_0 is the (half) length in the axial direction of the laser focus. We estimated $\omega_0 \approx$ 0.45 μm and $z_0 \approx$ 2 μm by a calibration experiment using the well-studied dye rhodamine 6G, whose diffusion coefficient is known to be $\approx 280 \times 10^{-12}$ m^2/s in water. From our fit, D, is 7.7 μm^2/s for the 15-20 kDa dextran coated nanoparticles and we calculated hydrodynamic diameter this sample to be 57 nm using equation (3.1). We also repeated the measurement several times and have plotted the statistical distribution of size of nanoparticles as a histogram in Fig 3.3 (d). This size distribution implies majority of the size of 15-20 kDa dextran coated sample lies

within the range of 55 ± 5 nm. The size from FCS measurement is also plotted in Fig 3.4 along with size from DLS and magnetic measurements.

The size from DLS and magnetic measurement as a function of molecular weight can be fit to the decaying exponential, $y = A[\exp(-x/B)]+C$, shown by solid line in Fig 3.4. Studies on pure dextran in solution show the diameter of the coiled polymer increases rapidly with molecular mass to 10 kDa then increases more slowly with a further increase in molecular weight [87]. Thus, this shallow increase in hydrodynamic size for nanoparticles samples coated with higher molecular mass dextran is consistent with results on pure dextran. However, while the hydrodynamic size determined using DLS and magnetic measurements approximately follow the functional form expected for dextran, the magnitude of hydrodynamic diameter differs greatly from what is expected based on physical considerations. Since the chain length of 5 kDa dextran in solution is 18 nm [87], the hydrodynamic diameter of iron oxide nanoparticles of core diameter 12 nm coated with a monolayer of 5 kDa dextran should be 48 nm. This is a factor of two smaller than the size obtained from DLS and magnetic measurement, and well outside the expected uncertainties for these characterization techniques. Similarly, the diameter of 20 kDa dextran in solution is 22 nm [87], so the size of the12 nm iron oxide nanoparticle coated with a monolayer 15-20 kDa molecular mass dextran should be approximately 56 nm, again about a factor of two smaller than measured using DLS.

We find, however, much better agreement between the hydrodynamic size measured using FCS and the size expected from such physical considerations. The diameter for the 15-20 kDa coated nanoparticles is approximately 55 +/- 5 nm, which is completely consistent with the expected size of 56 nm found by combining the independently measured sizes for the iron oxide nanoparticles and dextran in solution. Since the DLS unit was properly calibrated before the measurement, and the results are consistent with the independent magnetic measurements, we believe that the anomalously large size obtained from DLS not due to any instrumental error. Furthermore, the discrepancy is not due to the well-known dependence of viscosity on volume fraction [91] since for a factor of two error in size, the volume fraction should be two orders of magnitude greater than that we used (ϕ=0.2%) for these DLS measurement. Similar discrepancies in size have been also observed in previous studies using DLS to size polymer coated nanoparticles in solution, although the origin of this difference has not been discussed [55,56]. Considering our results, we suggest that for polymer coated iron oxide nanoparticles samples, FCS yields the accurate hydrodynamic size while DLS may overestimate the size by the factor of two.

We did magnetic hyperthermia measurement on a ferrofluid with 15-20 kDa dextran coated iron oxide. The ferrofluid was heated in the presence of an alternating magnetic field of 70 Oe from -45 to 45 ^{o}C in 2000 s and the rise in temperature was measured as a function of time, which is plotted in Fig 3.5a. Plateau feature seen in the Fig 3.5a is associated with the melting of frozen

ferrofluid. Rise in temperature of ferrofluid was affected by both ambient and magnetic heating. We also measured the rise in temperature of the ferrofluid as a function of time without applying magnetic field, which is plotted in Fig 3.5b in different time scale along with the result of Fig 3.5a for comparison. Time taken by ferrofluid at the melting phase due to ambient heating alone is about six times larger as compared to that the time taken due to ambient and magnetic heating. We also let the ferrofluid cool under ambient condition after heating it magnetically from room temperature to 40 ^{o}C to estimate the contribution of ambient heat loss in it. This is shown in Inset of Fig 3.5b. The temperature of ferrofluid as a function of time in the absence of magnetic field allows us to calculate the ambient heat exchange with ferrofluid.

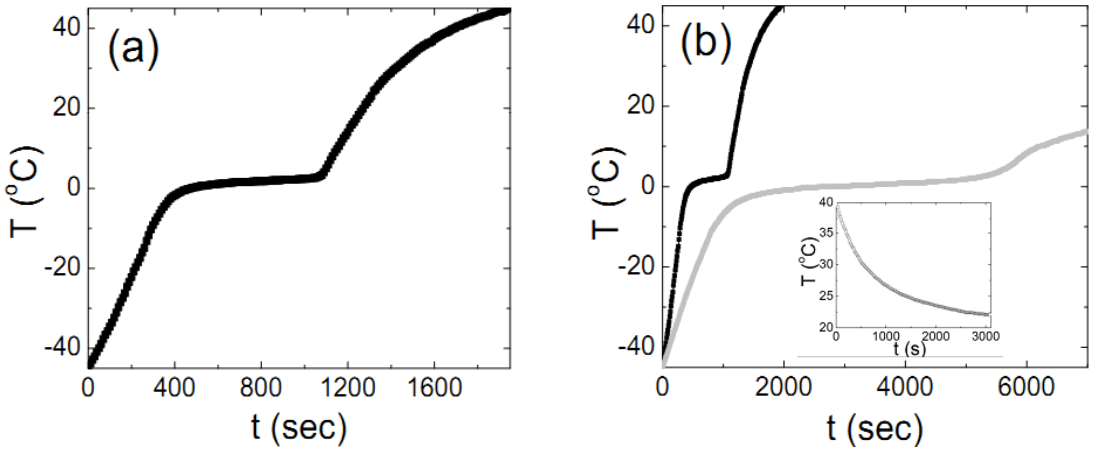

Figure 3.5: Temperature versus time for the ferrofluid heated magnetically from -45 to 45 ^{o}C (dark curve) and due to ambient heating from -45 ^{o}C to room temperature (gray curve). (a) with magnetic field (b) with and without a magnetic field. Inset: Thermal relaxation in a ferrofluid heated to +45 ^{o}C and allowed to cool to room temperature in zero applied magnetic field.

We first calculated the ambient heat transfer on frozen ferrofluid assuming that the heat transfer is radiative rather than ambient. We also assumed that the

temperature is uniform throughout the sample. The heating equation for the sample is given by:

$$-MC\frac{dT}{dt}+\varepsilon\sigma A\left(T_R^4-T^4\right)=0\,, \qquad \text{.....(3.4)}$$

Here M, C and T are the mass, specific heat and temperature of the frozen sample, respectively. The Second term in equation (3.4) represents the radiative heat transfer from room temperature (T_R) to the sample. σ is the Stefan-Boltzmann constant, A is the total area of the sample surface ($4x10^{-3}$ m^2) and ε is the emissivity, which is equatl to 0.98. We solved the equation (3.4) and obtained the transcendental equation for T as:

$$\frac{1}{2}\ln\left(\frac{T_R+T}{T_R-T}\right)+\tan^{-1}\left(\frac{T}{T_R}\right)=\frac{1}{2}\ln\left(\frac{T_R+Ti}{T_R-Ti}\right)+\tan^{-1}\left(\frac{Ti}{T_R}\right)+\frac{2T_R^3\varepsilon\sigma A}{MC}t\,, \qquad \text{..... (3.5)}$$

Where T_i is the temperature of the sample at t = 0. We fitted this equation to the ambient heating data of Fig 3.5b by taking T_i = 228 K, T_R = 295 K and specific heat capacity ice as a function of temperature. The fit (solid line) with data is shown in Fig 3.6a. Since the fit agrees with experimental data, it implies that there is radiative heat transfer in frozen ferrofluid. We calculated the magnetic heating power by subtracting ambient heating power in frozen ferrofluid obtained from Fig 3.6 a and plotted as a function of temperature in Fig 3.6b. The magnetic heating shows clear temperature dependence. In the frozen ferrofluid, only Néel heating contributes since the particles are fixed and Brownian relaxation is absent. We

fitted the magnetic heating power in frozen ferrofluid with theoretical power contributed by Néel

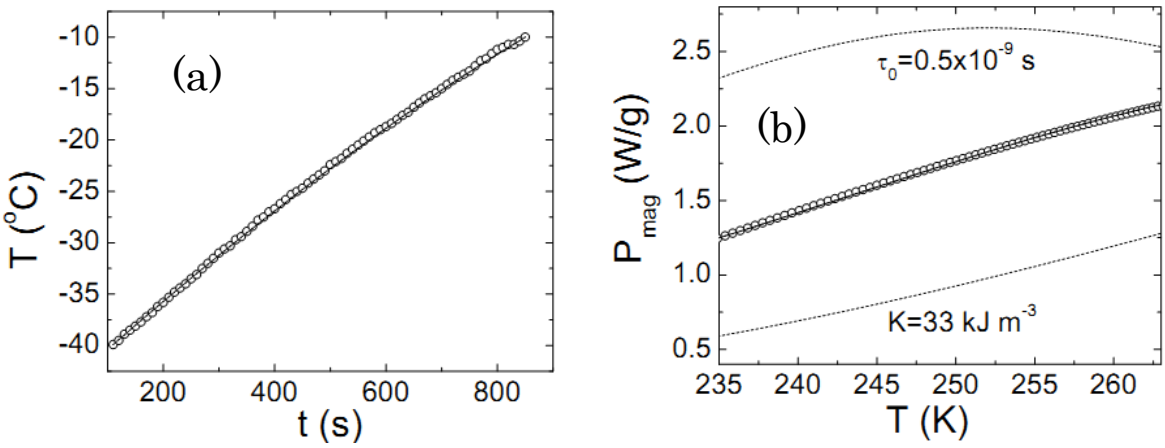

Figure 3.6: (a) Ambient heating from -40 to -10 °C (open circle) and fit to equation 3.5 (solid line) (b) Magnetic heating after subtracting background in frozen ferrofluid (open circle); solid line – theoretical Néel heating, dashed line – theoretical Néel heating at slightly lower τ_0 and higher K as compared to the values obtained from solid line fit.

relaxation only by taking τ_o =1.1x10^{-9} s, a magnetocrystalline anisotropy of K=31x10^3 kJ m^{-3}, and a magnetic core size of 12 nm. With the selection of these parameters, theoretical Néel heating power fit very well with the experimental data. However, the fit is very sensitive with the selection of these parameters since the slight change of these parameters lead to different power, which is shown in Fig 3.6b for the slightly lower value of τ_o and higher value of K. Ambient heating at low temperature in frozen ferrofluid is described very well by the radiative heat transfer. However, at the melting phase, where latent heat of melting is associated,

and above melting phase, where convective heat transfer may be dominant, we couldn't fit equation (3.5).

We have plotted experimental zero field (open circle) and field applied (closed triangle) heating data in Fig 3.7a. Thes data were obtained by taking the derivative of experimental data, temperature versus time, and multiplying dT/dt by the heat capacity and mass of the sample. For the frozen ferrofluid, we took the heat capacity of ice as 2108 $Jkg^{-1}{}^{o}C^{-1}$ and for liquid ferrofluid, we took heat capacity of of water as 4187 $Jkg^{-1}{}^{o}C^{-1}$. The mass of ferrofluid was 10 g. As expected, zero field power decreases with increasing temperature and becomes zero at room temperature. Also, the power is positive below room temperature and negative above room temperature indicating heat gain and loss by the sample below and above room temperature respectively. Field applied heating data shows higher power as compared to zero field heating due to the presence of additional heating caused by Néel and Brownian relaxation. Since we are unable to calculate the fraction of ice remaining as a function of temperature, we haven't calculated the power at the range of -2.5 to 2.5 ^{o}C. We have also calculated the magnetic heating power on frozen ferrofluid and liquid ferrofluid by using polynomial fits to model the data. Both zero field and field applied data on Fig 3.5b were fitted with polynomial and power of heating was calculated as mentioned for Fig 3.7 a. After subtracting the ambient power, only magnetic heating has been plotted in Fig 3.7b. In the frozen ferrofluid, the magnetic heating, which is due to only Néel relaxation, increases with increase in temperature upto approximately -15 ^{o}C, consistent with Fig 3.6 b.

The magnetic heating in liquid ferrofluid is greater than that in frozen ferrofluid, which is due to presence additional Brownian relaxation in liquid ferrofluid. However, the magnetic heating in liquid ferrofluid varies from 8 W/g near 10 °C to

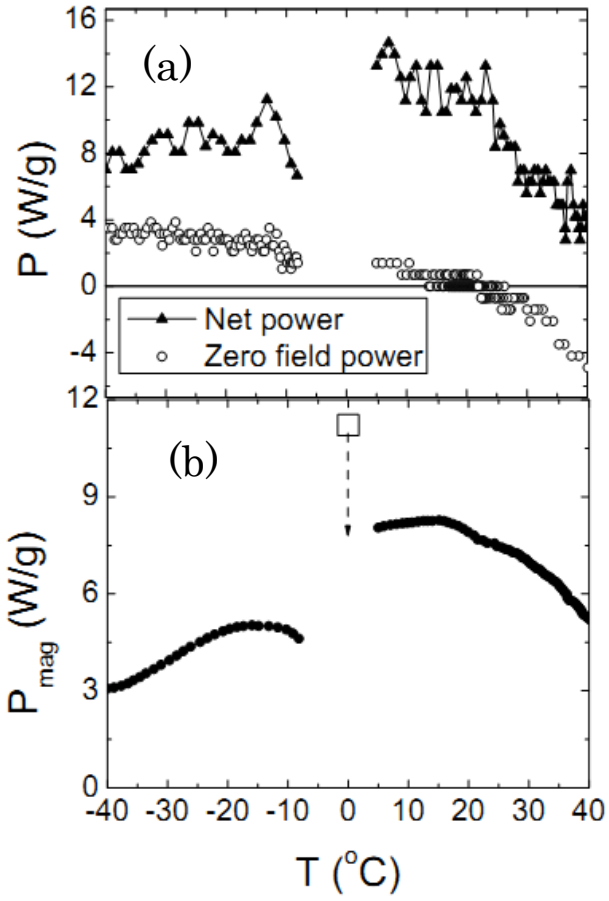

Figure 3.7: (a) Experimental heating power for ferrofluid with (closed triangle) and without (open circle) magnetic field. No background correction. (b) Magnetic heating power of ferrofluid after doing background correction using polynomial fit. Open square is the magnetic heating power at 0 °C.

just about 5 W/g at 40 °C. This decrease in magnetic heating in liquid ferrofluid is due to the temperature dependence of Néel and Brownian relaxation and also change in viscosity with temperature. We also calculated magnetic heating power at

0 °C by considering all the ferrofluid melted at 0 °C and is shown as a large square in Fig 3.7b.

3.2.3 CONCLUSIONS

We synthesized iron oxide nanoparticles coated with dextran having molecular weights of 5 kDa, 15-20 kDa, 60-90 kDa and 670 kDa. Their hydrodynamic size was measured using DLS, AC magnetization and FCS measurement. DLS and magnetic measurement gave sizes ranging from 90 to 140 nm, which is a factor of two larger than the size expected on the basis of physical consideration. FCS measurement on 15-20 kDa dextran coated sample gave a hydrodynamic diameter of about 55 nm, which is close to the expected value. We conclude that FCS measurement provide a more accurate estimate of particle size in dilute solutions than DLS and magnetic measurement. It is important to obtain accurate size of nanoparticles since there are many biomedical application where the size of nanoaprticles play a crucial role [92,93].

We did the magnetic hyperthermia measurement on ferrofluid from frozen state to liquid state and calculated power produced by Néel heating alone in frozen ferrofluid, and due to Néel and Brownian heating in liquid ferrofluid on the same sample. We found that ambient heating in frozen ferrofluid can be modeled by radiative heat transfer. We determined temperature dependent Néel heating in frozen ferrofluid, maximum magnetic heating in melting ferrofluid, and temperature dependent Néel and Brownian heating in liquid phase of ferrofluid. .

3.3 FATTY ACIDS COATED IRON OXIDE NANOPARTICLES

Fatty acids are carboxylic acid with long chains of hydrocarbon. Their chain lengths vary from 10 – 30 carbons. There are two types of fatty acids: saturated and unsaturated. Fatty acids having only single bonds between carbon atoms are called saturated since they are saturated with hydrogen and include lauric acid, myristic acid, palmitic acid, and stearic acid, among others. Fatty acids with one or more double bond between carbon atoms are referred as unsaturated since they need hydrogen to saturate. Unsaturated fatty acids include oleic acid, erucic acid, sapienic acid, and elaidic acid, among others. Unsaturated fatty acids have two configuration, namely, cis and trans. In cis configuration, two adjacent hydrogen aotms are on the same side of the double bond and offer flexibility to the chain whereas in trans configuration two hydrogen atoms are on opposite side of the double bond, which make the chain rigid. Fatty acids are not highly soluble in water and this limited solubility decreases with an increase in chain length. Since fatty acids are non polar, they dissolve readily in organic solvents such as cyclohexane, benzene, chloroform, and toluene. Fatty acids play an important role in many metabolic functions, such as moving oxygen through the bloodstream, assisting the function and development of cell membranes, and preventing early aging among others. Because of the many biomedical applications of fatty acids, we chose lauric

acid, myristic acid, and oleic acid to coat iron oxide nanoparticles and studied the magneto hydrodynamic properties of these nanocomposites.

3.3.1 EXPERIMENTAL DETAILS

We synthesized lauric acid (LA), myristic acid (MA) and oleic acid (OA) coated iron oxide nanoparticles as described in section 2.1.2. X-ray diffraction pattern of fatty acids coated iron oxide were taken using Cu Kα radiation on a Rigaku Ru2000 rotating anode diffractometer to confirm the crystal structure of nanoparticles. TEM images were taken using JOEL HR TEM 2010, operated at 200 kV, to get the core size of nanoparticles. Dynamic light scattering (DLS) measurements were performed to determine the hydrodynamic size of LA, MA and OA coated iron oxide nanoparticles dispersed in cyclohexane. These DLS measurement used a 632.8 nm He-Ne laser with the scattered light collected at 90^{o}. A 128-channel counter with 60 μs bin size was used to determine the correlation function, which can determine particles size down to 10 nm.

We used a Quantum Design Superconducting Quantum Interference Device (SQUID) to measure the DC magnetization as a function of temperature and magnetic field, while the AC magnetization was measured using a standard option in a Quantum Design Physical Property Measurement System (PPMS). For the magnetic measurements, we used 30 mg of powder sample mounted in a gelatin capsule and the sample was pressed with cotton to avoid any motion during the measurement. We used slightly different set-up for the magnetic hyperthermia than

the version presented section 3.2.1. These measurements used a 5 cm long coil with 80 turns. The current passing through the coil was 15 A at a frequency of 100 kHz, which produced an alternating magnetic field of 300 Oe.

The Mössbauer spectra were collected in the transmission geometry using both sides of a (Wissel) transducer coupled to cobalt 57 in Rh matrix sources of about 50 mCi (29 Oct. 2007) or approximately 13 mCi at the time of the measurements, and 256 channels of multichannel analyzers. A thin iron foil was used for the velocity calibration and the linearity verification. Janis VT series Cryostat was used to collect the Mössbauer spectra at 78 K. Approximately 70 mg of the sample were uniformly distributed in a Teflon circular cell of 1.7 cm diameter for the Mössbauer measurement. The isomer shift values are reported with reference to iron and the spectra were least square fitted with MossWin program.

For magneto-optic measurements, 0.4 ml of liquid ferrofluid in a standard quartz suprasil spectrophotometer cuvette having a 1 mm path length was placed between a pair of water-cooled Helmholtz coils, which could produce a DC magnetic field of 400 Oe. A He-Ne laser beam (λ = 632.8 nm) of power 10 mW was transmitted through the sample perpendicular and parallel to the applied field and the scattered light patterns were collected on a 220 mm x 220 mm translucent screen placed at distance of 500 mm from the sample. The time dependent images of field induced scattering patterns on the screen were taken and analyzed by image analysis software to produce 2D map of scattered light intensity.

3.3.2 RESULTS AND DISCUSSIONS

X-ray diffraction patterns of LA, MA and OA coated iron oxide nanoparticles are shown in Figs 3.8 a, b and c respectively. All the peaks can be labeled to the

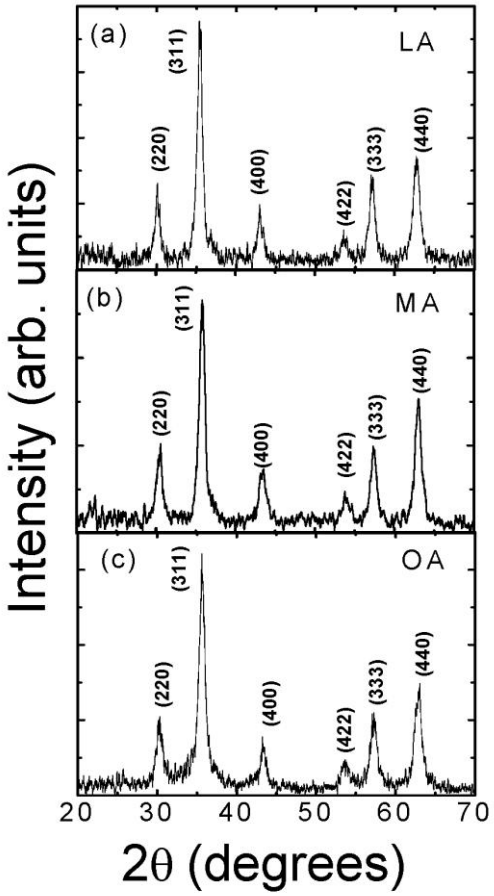

Figure 3.8. XRD patterns for (a) lauric acid (LA), (b) myristic acid (MA), and (c) oleic acid (OA) coated Fe_3O_4 nanoparticles. Taken from R. Regmi et al., *J. Appl. Phys.* **106**, 113902 (2009).

Bragg reflections expected for Fe_3O_4. We also calculated the size of nanoparticles from the most intense peak, the (311) reflection, using the Debye Scherrer equation, $d=(0.9\lambda)/\beta\cos\theta$, where β is the full width half maximum (FWHM) of the peak. This yielded values of 12.3, 11 and 10.5 nm for the crystallite size for

LA, MA and OA coated samples respectively. We also calculated the size of the nanoparticles from two more intense peaks, (440) and (333), and found an uncertainty of approximately 2 nm on the size of nanoparticles. TEM images of LA, MA and OA coated iron oxides are shown in Figs 3.9a, b and c respectively. We measured the size of many nanoparticles manually to plot the histogram, which was fitted by a log normal distribution, shown in the inset of Fig 3.9a, b and c for corresponding particles. All the nanoparticles were about 12 nm with a standard deviation of 2 to 3 nm. The sizes of nanoparticles along with standard deviation are given in Table I.

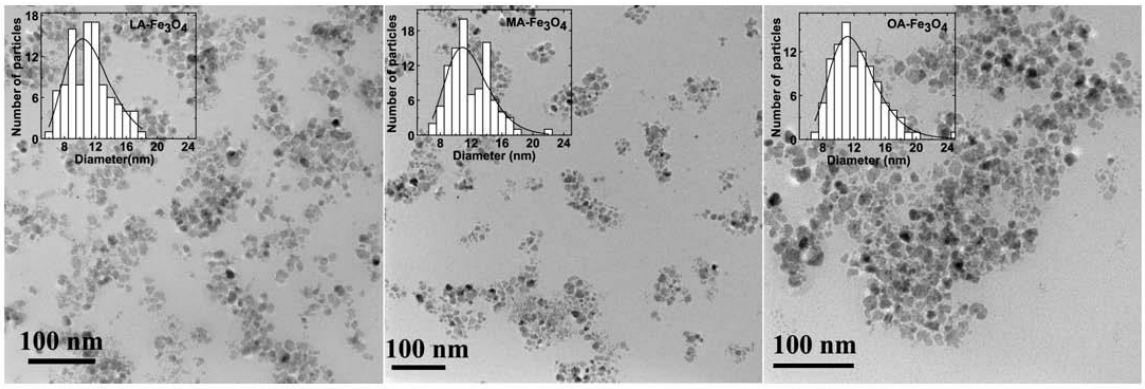

Figure 3.9. TEM images for (a) lauric acid, (b) myristic acid, and (c) oleic acid coated Fe_3O_4 nanoparticles. For all images the scale bar shows a length of 100 nm. The insets show a histogram of the particle sizes, with the solid line showing a fit to a log-normal distribution. Taken from R. Regmi et al., *J. Appl. Phys.* **106**, 113902 (2009).

We did thermogravimetric analysis (TGA) measurements for all three fatty acid coated nanoparticles along with bare Fe_3O_4 to determine the amount and number of coated layers of surfactants for these nanocomposite materials. The TGA curves for these samples are shown in Fig. 3.10. For the LA, MA and OA coated

samples, there is a weight loss of 12, 15, and 31% respectively, showing single step transition close to 400 ^{o}C. This single step transition implies that there is a monolayer coating of LA, MA, and OA on the corresponding particles. We also found a 3-4% loss in weight in the bare Fe_3O_4 nanoparticles at lower temperatures. We attribute this decrease to adsorbed moisture or hydroxyl groups on the surface of the bare Fe_3O_4. Although these measurements were done in a nitrogen atmosphere, we found a weight gain for these nanoparticles at higher temperature due to the oxidation of nanoparticles.

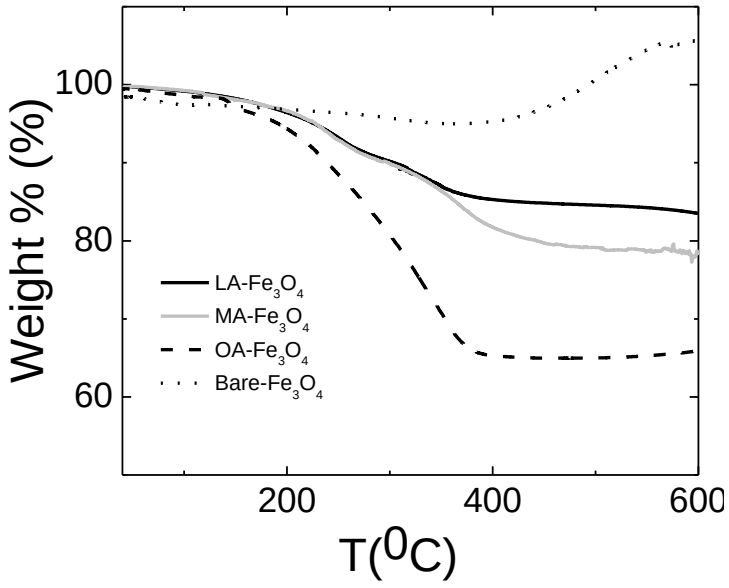

Figure 3.10. Thermo Gravimetry Analysis (TGA) for bare Fe_3O_4 nanoparticles, lauric acid, myristic acid, and oleic acid coated samples.

We used DLS to determine the hydrodynamic size of fatty acid coated nanoparticles in the cyclohexane solvent. We fitted the autocorrelation function obtained from the DLS measurement and extracted the relaxation rate Γ at the wave vector $q=(4\pi n\sin(\theta/2))/\lambda_0$, where $\theta=90^{o}$, $\lambda_0=632.8$ nm and refractive index of

cyclohexane, n=1.44. Using $\Gamma=Dq^2$ and $D=k_BT/6\pi\eta R$, we calculated the hydrodynamic radius of each nanoparticle by using the viscosity of cyclohexane 0.98 cP. The DLS sizes of LA, MA and OA coated nanoparticles are given in Table 3.1. Since the chain lengths of LA, MA and OA are 1.6, 1.8 and 2.0 nm respectively, the hydrodynamic diameter of these polymer coated nanoparticles are approximately twice that calculated on the basis of the chain length of a single layer coating of surfactant added to the core size of the nanoparticles. We repeated the DLS measurement on these samples after a six month period and found the same result,

Samples	M_s (emu/g) ±3 emu/g	D_{XRD} (nm) ±2 nm	D_{DLS}(nm)	D_{TEM} (nm)	σ_H (nm) TEM
Fe_3O_4 LA	58	12.3	32	11.6	3.3
Fe_3O_4 MA	62	11	34	11.9	2.9
Fe_3O_4 OA	58	10.5	36	12.3	3.1

Table 3.1: Properties of ferrofluid nanoparticles coated with surfactants of varying chain lengths; M_s – saturation magnetization, scaled by the Fe_3O_4 mass fraction in the composite; D_{XRD} – crystalline diameter from XRD; D_{DLS} – hydrodynamic diameter from DLS as discussed in the text; D_{TEM} – solid diameter from TEM; σ_H – standard deviation in D_{TEM}.

precluding the possibility of agglomeration accounting for the overestimation of the size. Similar discrepancies in the measured size of polymer coated nanoparticles have been reported in the literature previously [55,56]. Since the hyperfine field is

sensitive to Fe valence, we collected Mössbauer spectra to differentiate Fe_3O_4, which contains both divalent and trivalent Fe, from γ-Fe_2O_3, which contains only trivalent Fe. We show the data for only the LA coated sample in Fig. 3.11, as the Mössbauer spectra of all LA, MA and OA coated samples were qualitatively and quantitatively similar. The values of the fitted Mössbauer parameters for LA-Fe_3O_4 are listed in Table 3.2. As described in section 2.2.11, the isomer shift (δ), quadrupole splitting (Δ) and hyperfine field (H) give information about the valence states of iron and their occupancy in the crystal lattice.

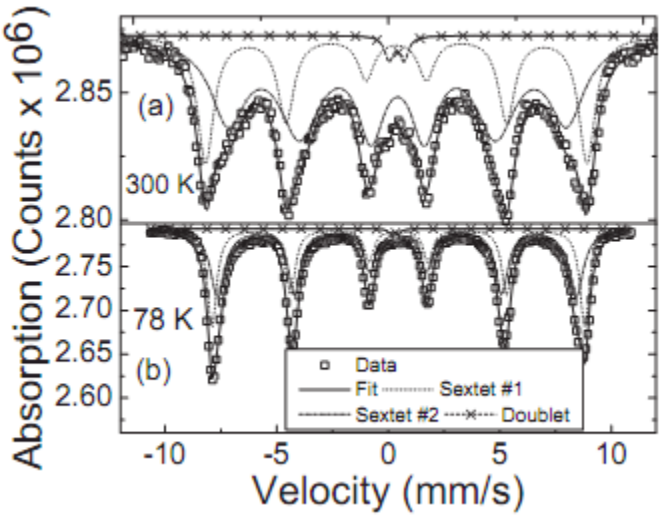

Figure 3.11: ^{57}Fe Mossbauer spectra for lauric acid coated Fe_3O_4 nanoparticles at (a) 300 K (b) 78 K. Open rectangle, dot, dash dot, cross and solid line represent experimental data, 1st sextet, 2nd sextet, doublet and fitted to two sextets and one doublet respectively. Taken from R. Regmi et al., *J. Appl. Phys.* **106**, 113902 (2009).

The flipping frequency of the net magnetization in non-interacting magnetic nanoparticles is given by $f = f_0 \exp(-KV/k_BT)$ where K is the magnetocrystalline anisotropy constant, V is the volume of a nanoparticle, f_0 is the microscopic attempt frequency (typically in the order of 10^{12} Hz), and T is the temperature. For $f << f_{obs}$,

the observation frequency during the experiment (10^8 Hz for ^{57}Fe), superparamagnetic fluctuations are suppressed, and a six line Mössbauer pattern is observed. For $f>>f_{obs,}$ the superparamagnetic fluctuations are dominant, and the six line pattern collapses into a quadrupole doublet or a singlet. However, because of the exponential dependence of *f* on the nanoparticle volume and the size polydispersity of these nanoparticles, both six line patterns and quadrupole doublets can be observed in the same spectrum.

Samples	T = 300 K			T = 78 K		
	H ±1.5 (kOe)	δ ±0.04 (mm/s)	Δ±0.04 (mm/s)	H ±1.5 (kOe)	δ ±0.04 (mm/s)	Δ±0.04 (mm/s)
Fe_3O_4 LA	466	0.31	0.01	520	0.45	0.01
	414	0.36	0.02	499	0.40	0.10

Table 3.2- Mossbauer parameters for LA coated Fe_3O_4 nanoparticles; H- hyperfine magnetic field; δ - isomer shift; Δ – quadrupole splitting.

At 300 K, where the nanoparticles moments have sufficient thermal energy to fluctuate freely, the Mössbauer spectra of the lauric acid coated sample shown in Fig. 3.11a were fitted using two sextets at hyperfine field of H_1 = 466 kOe and H_2 = 414 kOe. H_1 is produced by Fe^{3+} at a tetrahedral A-site and the octahedral B-site of

a spinel ferrite whereas H_2 is produced by a mixed valence state, $Fe^{2.5+}$, at octahedral B-site due to the electron hopping mechanism between Fe^{2+} and Fe^{3+} [94]. Additionally, the spectrum also has a quadrupole doublet with isomer shift (δ) = 0.33 mm/s and quadruple splitting (Δ) = 0.58 mm/s, which is characteristic of the presence of superparamagnetic Fe_3O_4 nanoparticles.

There are no thermal fluctuations at 78 K because of the freezing of the nanoparticles moments below the blocking temperature of about 150 K for lauric acid coated nanoparticles. The Mössbauer spectra of the lauric acid coated sample shown in Fig. 3.11b were fitted using two sextets at hyperfine field of H_1 = 520 kOe and H_2 = 499 kOe. These values are in agreement with the literature value of magnetite phase [94]. This observation also precludes the presence of other phases of iron oxide, such as hematite or goethite, where iron is present at only one crystallographic site. Also, it discounts the presence of γ-Fe_2O_3 since Fe^{3+} on both A and B sites have same value of hyperfine field, 510 kOe.

We did DC magnetization measurements for the LA, MA, and OA coated nanoparticles. The magnetizations as a function of DC magnetic field for all three samples are shown in the inset of Fig 3.12. The LA, MA and OA coated nanoparticles have saturation magnetization of 58, 62, and 58 emu/g of Fe_3O_4 respectively, excluding the mass contribution from surfactants determined from TGA. These values are given in Table I with an uncertainty of 3 emu/g of Fe_3O_4, which is due to the uncertainty in weight of the sample for TGA and magnetic measurements. The saturation magnetization of these nanoparticles is smaller than

the bulk value of Fe_3O_4, 90 emu/g, which can be attributed to the presence of a disordered surface spin layer in nanoparticles [95].

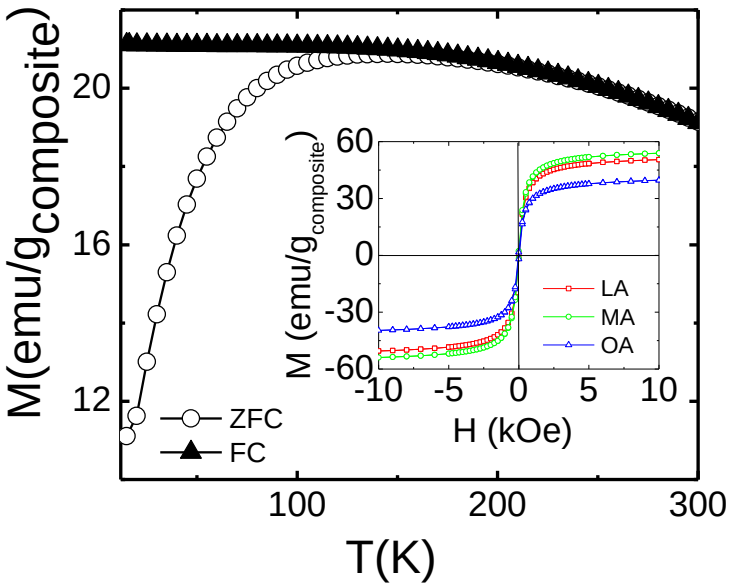

Figure 3.12: Zero-Field cooled (ZFC) and Field cooled (FC) magnetization curves for lauric acid coated Fe_3O_4. Inset: Room temperature magnetization as a function of field for lauric acid, myristic acid, and oleic acid coated Fe_3O_4. These plots show the magnetization scaled by the total mass of the composite system.

Also, the surfactant coating can further reduce the saturation magnetization of magnetic nanoparticles by making more disordered surface spins [96].

The single valued M(H) curve at room temperature implies that these nanoparticles are superparamagnetic. This is also confirmed by superparamagnetic blocking crossover observed in the field cooled (FC) and zero field cooled (ZFC) magnetization measurements. Since all the fatty acids coated nanoparticles showed similar behavior, we have shown representative ZFC and FC curves under a measuring field of 200 Oe for the LA coated iron oxide nanoparticles. The ZFC curve

shows a broad maxima at 150 K, indicating a ploydispersity of the nanoparticles, consistent with TEM images and the room temperature Mössbauer results.

We also did the AC magnetization measurement on lyophilized samples of LA, MA and OA coated nanoparticles to probe the dynamics of the blocking transition. Again, we show only a representative curve for the LA coated sample. The imaginary part of the AC susceptibility as a function of temperature at three different frequencies is shown in Fig. 3.13.

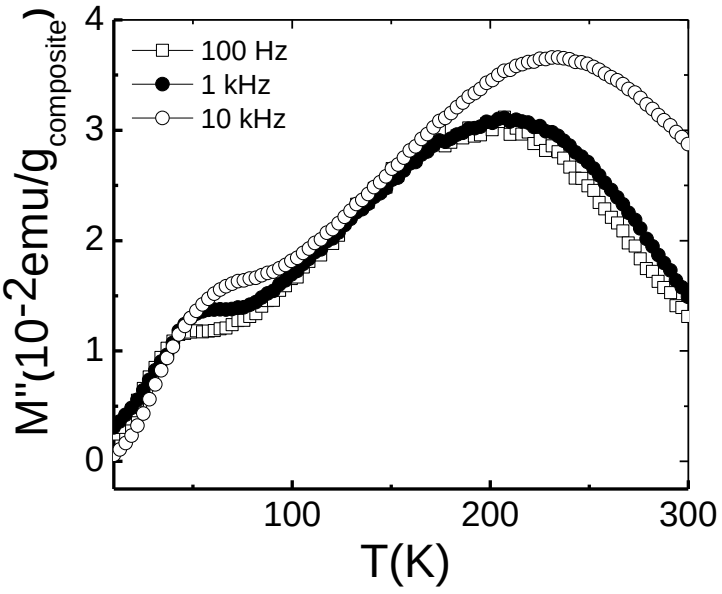

Figure 3.13: Temperature dependence of the out-of-phase component of the ac susceptibility of lauric acid coated Fe_3O_4 nanoparticles measured at 100 Hz, 1 kHz, and 10 kHz.

Since the sample was lyophilized,Brownian relaxation is completely suppresses so the peak in AC loss is associated only with Néel relaxation. As the peak temperature increases with increasing frequency, we used the Arrhenius equation, $f = f_0 \exp(-E_A/k_BT)$, to estimate the activation energy (E_A) and characteristic frequency

(f_0) of the moment reversal. We found E_A~ 570 meV with f_0~2.8 x 10^{16} Hz for the LA coated sample, E_A~ 490 meV with f_0~1.6 x 10^{14} Hz for MA coated sample and E_A~ 530 meV with f_0~1.1 x 10^{14} Hz for OA coated sample. We had also done AC magnetization measurement for bare Fe_3O_4 yielding E_A= 348 meV with f_0=7.2 x 0^{10} Hz, which are systematically smaller than the values obtained for the fatty acids coated samples. The difference may be due to the change in surface spin properties for surfactant coated nanoparticles. The peak at lower temperature, 50 K, is likely due to the disordered surface spins freezing into spin-glass-like state [97].

These AC and DC magnetization and Mössbauer measurements show that the magnetic properties of nanoparticles are independent of surfactant coating, which allows us to investigate how the magneto hydrodynamic properties depend on the surfactant, without concern to differences in the magnetic reponse of the nanoparticles. As a first study, we investigated the magneto hydrodynamic response of different chain length fatty acids coated samples by magnetic hyperthermia. We applied a 300 Oe alternating magnetic field at the frequency of 100 kHz to 1 mL of LA, MA and OA coated iron oxide dispersed in cyclohexane. The rise in temperature is shown in Fig 3.14. We also calculated the specific absorption rate (SAR) using the following relation:

$$\text{SAR} = \frac{C_L \rho_L}{\varphi}\left(\frac{\Delta T}{\Delta t}\right) \quad \text{.....(3.6)}$$

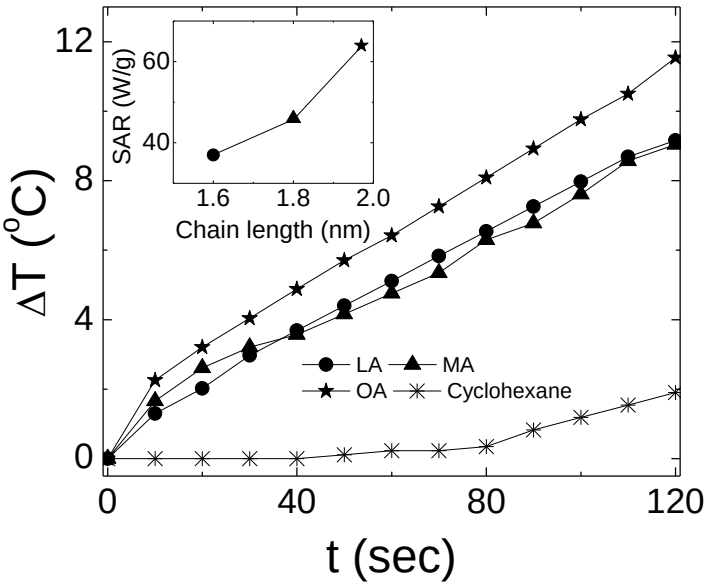

Figure 3.14: Rise in temperature as a function of time for lauric acid (open rectangle), myristic acid (open circle) and oleic acid (open star) coated Fe_3O_4 along with carrier liquid cyclohexane(open triangle). Inset: SAR plotted against chain length.

where C_L and ρ_L are the specific heat and density of the carrier liquid, φ = weight concentration of the magnetic nanoparticles in the ferrofluid, and $\frac{\Delta T}{\Delta t}$ is the rate of increase in the temperature. Substituting C_L=1.83 kJ/kg-K and ρ_L= 0.78 g/cm^3 for cyclohexane, ϕ = 5 mg/ml, and $\frac{\Delta T}{\Delta t}$ as the initial slope of the curve, we found the SAR for LA, MA and OA coated sample to be 37, 46, and 64 W/g respectively. The differences in these values reflect the contribution of Brownian relaxation, which depends on the chain length and hydrodynamic size of the nanoparticles. Since the magnetic properties are similar for all fatty acid coated samples, the contributions from Néel relaxation are practically identical for all samples. The SAR values are

plotted as a function of chain length in the inset of Fig. 3.14, which implies that the SAR increases approximately linearly with the chain length of the surfactants.

The magneto-hydrodynamic response of the ferrofluids was also investigated by dc magnetic-field-induced anisotropic light scattering patterns. An anisotropic interaction between the induced dipoles of nanoparticles in the presence of the dc magnetic field caused them to from chain like structure. These chain like structures have been studied extensively both theoretically and experimentally [98-100]. The self-assembly results in a strong anisotropy of the scattering patterns for the light propagating through the ferrofluid in the presence applied magnetic field [98,101]. The time evolution of these patterns is used to investigate the hydrodynamic response of nanoparticles in solution [98,101].

We observed strong anisotropy for all three samples for the light propagating perpendicular (Figure 3.15a) to the direction of applied field as compared to the light propagating parallel to the direction of applied field (Figure 3.15b). We used the framework and system notations introduced in reference [98] for a quantitative description of the patterns. The time-dependent optical anisotropy factor *A(h,t)* is defined as:

$$A(h,t) = 2\frac{I_{\perp}(h,t) - I_{\parallel}(h,t)}{I_{\perp}(h,t) + I_{\parallel}(h,t)} \quad \text{.....(3.7)}$$

where $I_{\perp} = I(h, \alpha = \pm\pi/2)$ is the intensity of light scattered perpendicular to the field and $I_{\parallel} = I(h, \alpha = 0) = I(h, \alpha = \pi)$ is the intensity of light scattered parallel to the

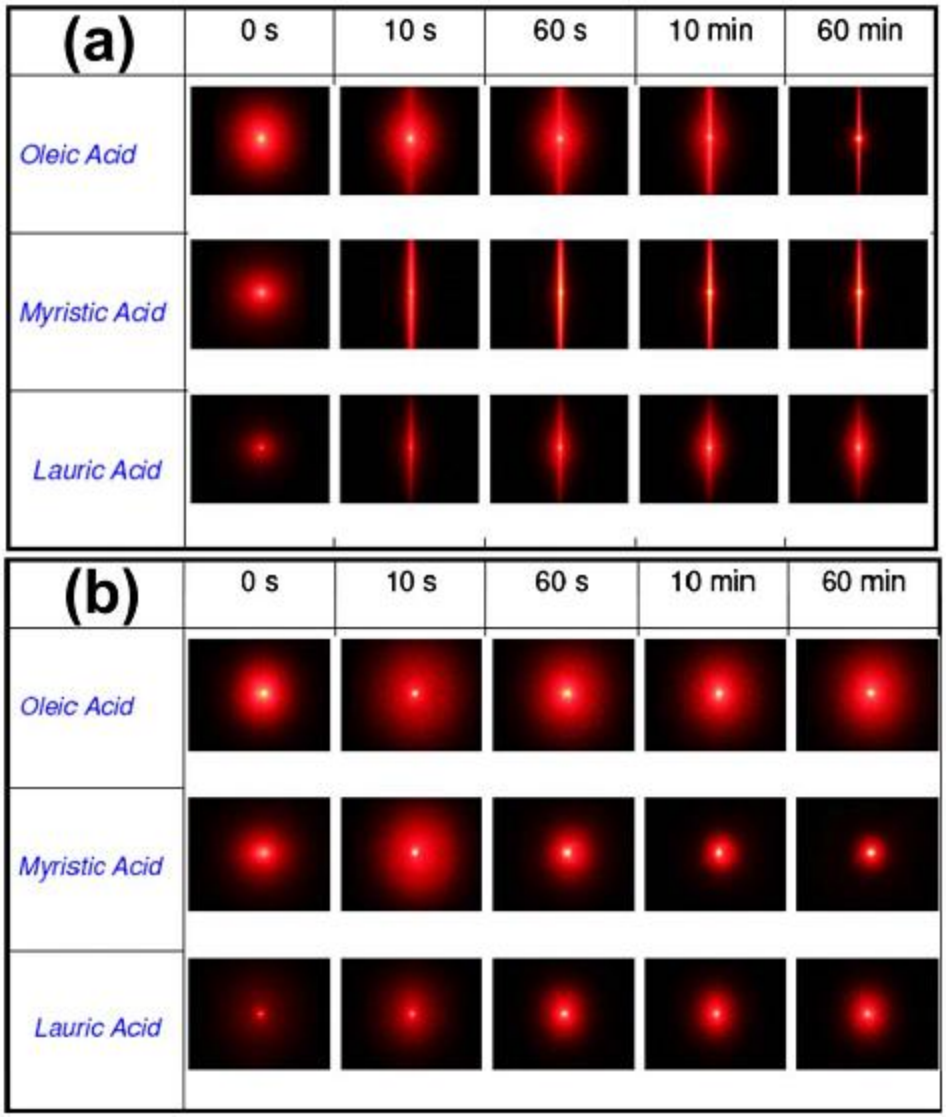

Figure 3.15: Time dependent light scattering patterns in a 400 Oe applied magnetic field at representative instants of time after turning ON the magnetic field for light propagating (a) **perpendicular** to the field and (b) **parallel** to the field. Taken from R. Regmi et al., *J. Appl. Phys.* **106**, 113902 (2009).

magnetic field. These notations are explained in reference [98]. Scattering patterns (Figures 3.15a and 3.15b) show that $I_{\parallel}(h) < I_{\perp}(h)$, which is also is reflected in the angular dependence of the scattered intensity of MA coated sample shown in Figure

3.16 for several value of scattering vector h. This suggests the development of anisotropic nanoparticle chains and columns.

Time evolution of optical anisotropy factor A for LA, MA and OA coated sample is shown in Fig 3.17 for the median value of scattering vector h = 60 mm. We observed correlation between the kinematics of chain formation and optical anisotropy constant depending on the chain length of the surfactant. We found that the time evolution of larger chain length OA coated sample is slower than other samples. We also observed fluctuations of A for LA and OA coated samples for time $0 < t < 1500$ s after turning the magnetic field ON. Similar fluctuations in A (Figure 3.17) were

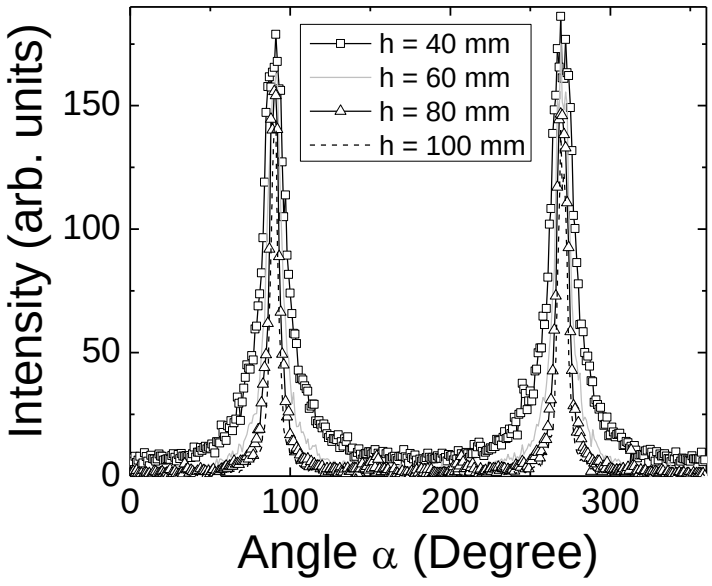

Figure 3.16: Angular dependence of the intensity of scattered light for the myristic-acid coated sample.

observed for all three surfactant coated sample while turning the field OFF. Shorter chain length LA (C_{12} chain length) coated sample has shown larger fluctuations while switching the field OFF whereas longer chain length OA coated sample (C_{18}

chain length) has shown more fluctuations while switching the field ON. We also observed remnant magnetism in all there sample after removing external magnetic field persisting to a time scale of hours. OA coated sample has shown maximum remanance and anisotropic properties as compared to other samples. The theory of fluctuation-mediated long range lateral chain interaction was first proposed by Halsey and Torr [99], and have also further investigated by others [102-104].

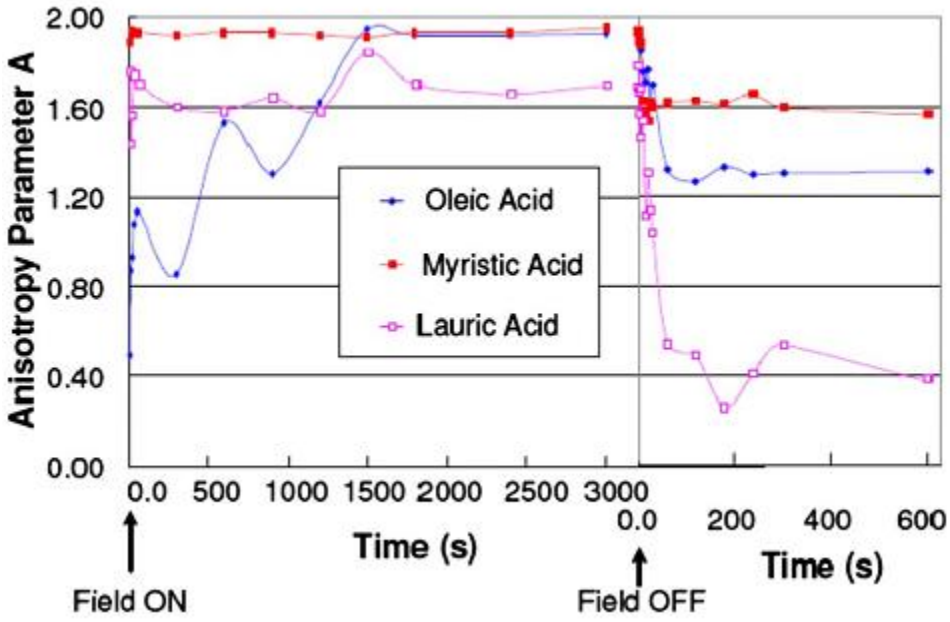

Figure 3.17: (Color on-line) Time dependence of the optical anisotropy parameter A at the median value (h = 60 mm) of the scattering vector for the oleic acid, myristic acid and lauric acid coated nanoparticles with field ON and OFF. Taken from R. Regmi et al., *J. Appl. Phys.* **106**, 113902 (2009).

Since the scattering pattern is sensitive to chain-chain separation, the fluctuation in OA and LA coated sample reflects the chain formation during field ON and deformation during field OFF.,

3.3.3 CONCLUSION

We investigated the magnetic and magnetohydrodyanmic properties of lauric acid, myristic acid, and oleic acid coated iron oxide nanoparticles. The magnetic properties did not vary significantly among the different surfactant coating. Conversely, the magnetic heating and magneto-optic properties did depend on the hydrodynamic size, which varied over the different chain length fatty acids coated iron oxide nanoparticles. In magnetic heating, the specific absorption rate (SAR) increases with increase in chain length. Magneto-optic measurement also suggested strong surfactant dependent optical anisotropy. This implies that magnetic nanoparticles with different hydrodynamic size respond differently in the presence of both AC and DC magnetic field, which allows us to control the magnetohydrodynamic properties of magnetic nanoparticles by coating them with different chain length surfactants.

3.4 SUMMARY

We synthesized iron oxide nanoparticles coated with different chain lengths of dextran varying from 5 kDa to 670 kDa. Measurement of hydrodynamic size on these nanoparticles by three different techniques namely DLS, AC magnetization and FCS suggests that FCS measurements on polymer coated nanoparticles give the most accurate hydrodynamic size whereas DLS and magnetic measurement find diameters a factor of two larger than expected from physical considerations.

We also did magnetic hyperthermia measurement on the 15-20 kDa dextran coated sample continuously from the frozen to the liquid phase to differentiate the contributions of Néel and Brownian heating. These measurements suggested that magnetic heating due to Néel and Brownian relaxation are temperature dependent. We also found significant magnetic heating in the inhomogeneous melting phase of the nanoparticles as compared to the heating on frozen and liquid ferrofluid, which may be because of enhanced Brownian relaxation due to finite size effects, capillary forces in inhomogeneous melting phase, and increased viscosity at low temperature.

We studied the magnetohydrodynamic properties of different chain length fatty acids (lauric, myristic and oleic acid) coated iron oxide nanoparticles. We found that the magnetic properties of these nanoparticles do not vary with different surfactant coating, unlike the magnetohydrodynamic properties. Different chain length surfactants change the hydrodynamic size of nanoparticles, which modifies the Brownian relaxation. This means that the magnetic heating and magneto-optic properties of liquid ferrofluid, both of which depend on Brownian relaxation of nanoparticles, also vary with the chain lengths of surfactant coatings. This provides another handle to tune the response of magnetic nanoparticles in solution without changing the magnetic response of the particles.

CHAPTER 4

DRUG DELIVERY USING MAGNETIC NANOPARTICLES

4.1 INTRODUCTION

Delivering drug to specific sites and at specific concentrations *in vivo* increase their therapeutic effects and minimizes potentially dangerous side effects. Many non-magnetic drug carriers have been used for the targeted drug delivery, but most of these lack good targeting and are cleared up by the reticuloendothelial system (RES). The RES is a part of immune system and engulfs foreign object, harmful bacteria and virsues, and also ingests abnormal and old cells in our body. Magnetic nanoparticles have a number of advantages for targeted drug delivery, including: 1) they can be controlled by non-invasive external magnetic field to accumulate at specific site *in vivo* 2) their surface can be modified to attach ligands to target specific site *in vivo* 3) they are small enough to accumulate inside cells 4) they can be heated by applying non-invasive external alternating magnetic field to release the drug 5) they acts as contrast agent and their distribution inside body can be monitored by using magnetic resonance imaging and 6) iron oxide magnetic nanoparticles are biocompatible and has food and drug administration (FDA) approval to use *in vivo*. Given the great potential of iron oxide nanoparticles for targeted drug delivery, we have studied drug release from a thermosensitive

polymer Poly-*N*-isopropylacrylamide (PNIPAM) triggered by magnetic hyperthermia. In addition, we have also studied the drug release from different molecular mass dextran coated iron oxide nanoparticles to investigate the effect of chain length on the drug release profile.

4.2 HYPERTHERMIA CONTROLLED DRUG RELEASE FROM MAGNETIC MICROGELS

Poly-*N*-isopropylacrylamide (PNIPAM) is a biocompatible and stimuli-responsive polymer having a number of biomedical application including controlled drug delivery, artificial muscles, cell adhesion mediators, and precipitation of proteins [105-109]. PNIPAM shows a reversible volume changing phase transition associated with a structural coil-to-globule conformational change in solution above the lower critical solution temperature (LCST) of 305 K (32 ^{o}C) [110-113]. PNIPAM absorbs water and swells below the LCST while it shrinks and release hydrophobically bound water above the LCST. This property has been used for studies of controlled drug release using PNIPAM [114,115]. There has been considerable interest to synthesize nanocomposites with stimuli-responsive polymer and metal and metal oxide for chemotherapy drug release [116-122]. In these nanocomposites, nanoparticles are embedded in cavities or polymer shells and immobilized by entanglement or covalent bonding with the chains. In the proposed chemotherapy delivery vehicle, the hybrid composite material consisting of PNIPAM and iron oxide nanoparticles is loaded with the drug to be delivered and

injected in the vasculature surrounding the target tumor. Incorporating iron oxide nanoparticles in the polymer matrix provides a number of benefits, including: 1) the ability to determine the distribution profile of the drug attached to the PNIPAM/magnetite composite using Magnetic Resonance Imaging 2) the possibility of remotely and controllably releasing the drug by the non-invasive application of an external magnetic field, and 3) increasing the efficacy of the drug by locally heating the tumor site.

In a recent study by Purushotham *et al.* [120] magnetite was incorporated in the PNIPAM matrix and the composite showed the drug release at the rate 0.001 mg/ min when heated from 310 to 321 K (37 to 48 ^{o}C) over a total time of 47 min. Hoare *et al.* [119] showed drug release of ~0.012 mg/min in the same system over a time interval of 35-75 min. These studies show substantial drug release can be produced solely by magnetic heating, but the timescales involved are relatively long. However, if this targeted drug release is to be combined by magnetic hyperthermia therapy, the elevated temperatures should be maintained only for much shorter time periods to avoid damaging the surrounding cells. The objective of our study is to investigate the *in vitro* burst release of chemotherapy drugs loaded into a PNIPAM/nanoparticles composite, driven solely by the heating produced by an external magnetic field in a *short interval of time*. We selected mitoxantrone as the model anti cancer drug because its effectiveness increases at 316 K (43 ^{o}C), making it a suitable candidate for combined targeted drug release/hyperthermia applications [123].

4.2.1 EXPERIMENTAL DETAILS

Magnetite nanoparticles having a diameter of roughly 12 nm were prepared by a co-precipitation method described in detail in section 2.1.1. The PNIPAM microgels were synthesized by a free radical polymerization technique as described in section 2.1.6. Thermogravimetric analysis between 315 K and 1000 K, shown in Figure 1, established that the resulting PNIPAM-SA-Fe_3O_4 composite contained 50 % iron oxide by mass, as indicated by the sharp drop in sample weight at the polymer dissociation temperature. This dissociation temperature can be determined more precisely by plotting the temperature derivative of the thermogravimetric response (also shown in Figure 4.1). This decomposition temperature is found to be very close to 600 K.

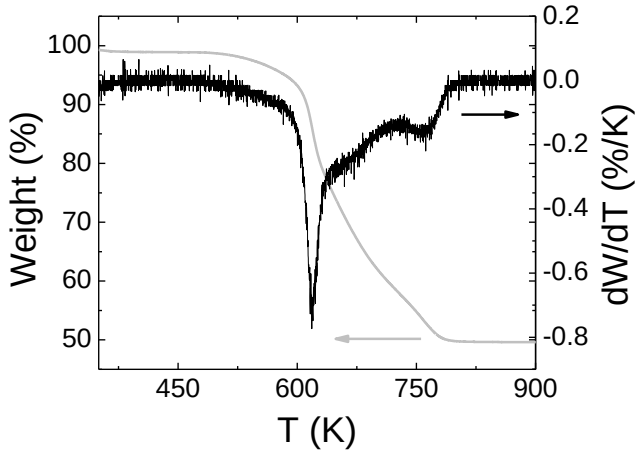

Figure 4.1: Thermogravimetric weight as a function of temperature for PNIPAM-SA-Fe_3O_4 (lighter line) and the temperature derivative of the weight (dark line).

In order to increase the colloidal stability of the composite, we had added 60 mg of sodium poly(styrene-sulfonate) (PSS) to the magnetic microgels since PSS has a

sulfonate group (SO_3^-), which creates negative charge on the surface of the PNIPAM-SA-Fe_3O_4 and helps to avoid agglomeration by electrostatic repulsion making well dispersed ferrofluid. We imaged the PNIPAM-SA parent microgels and PNIPAM-SA-Fe_3O_4 magnetic microgels using a Hitachi S-2400 Scanning Electron Microscope (SEM) and a Jeol-2010 FasTEM Transmission Electron Microscope (TEM). The dynamic light scattering (DLS) measurements were performed using a 90 Plus particle size analyzer from Brookhaven Instrument Corporation to investigate samples of PNIPAM-SA and PNIPAM-SA-Fe_3O_4 dissolved using deionized water as a solvent. We measured the dc magnetization of dry PNIPAM-SA-Fe_3O_4 and ac magnetization of a solution PNIPAM-SA-Fe_3O_4, using DI water as the carrier liquid, using the standard ACMS option on a Quantum Design Physical Property Measurement System (PPMS). The thermodynamics of the phase transition of the PNIPAM/nanoparticle composites was investigated using a Q 2000 DSC system (TA Instruments, Delaware, USA). Samples of PNIPAM-SA, PNIPAM-SA-Fe_3O_4 and bare Fe_3O_4 nanoparticles were prepared at concentration of 5 mg/ml in DI water. The samples were scanned from 283 to 323 K at a scan rate of 3 K/min under a continuous nitrogen stream. TA universal analysis software extracted both the transition temperature and ΔH, which was determined from the area under each peak.

The magnetic heating was accomplished using an RF generator model CLX-2750 (COMDEL) to produce an alternating magnetic field having an amplitude of approximately 130 Oe at a fixed frequency of 380 kHz. The samples, consisting of 50

mg of PNIPAM-SA-Fe_3O_4 loaded with the anticancer drug mitoxantrone dispersed in 0.5 ml phosphate buffer solution with pH 7.4, was placed inside a 40 turn induction coil of length 8.5 cm and surrounded by a high density Styrofoam insulation to prevent direct heat transfer from the coil to the sample. The temperature of the solution was measured using an IR thermometer having a temperature resolution of +/- 0.6 ^oC. The amount of drug released from the magnetic microgel at different points in the experiment was determined by using a Cary 50 Bio, UV-Visible spectrophotometer to measure the transmission of liquid decanted from the sample. A phosphate buffer with a pH 7.4 was used as the solvent. In order to compare the magnetically induced drug release with conventional heating methods, we also investigated the release from PNIPAM-SA loaded with mitoxantrone heated in a standard water bath.

4.2.2 RESULTS AND DISCUSSIONS

We imaged the PNIPAM-SA and PNIPAM-SA-Fe_3O_4 microgels using scanning electron microscopy and the PNIPAM-SA-Fe_3O_4 sample using transmission electron microscopy, as shown in Fig. 4.2. Figs 4.2a and b present SEM images for PNIPAM-SA and PNIPAM-SA-Fe_3O_4 respectively, showing the typical lengthscale for these polymer globules, being 360 nm for PNIPAM-SA and 200 nm for PNIPAM-SA-Fe_3O_4. While it is difficult to unambiguously establish the sample morphology, the TEM images of PNIPAM-SA-Fe_3O_4, Figs 4.2c and d, suggest that the Fe_3O_4 nanoparticles partially coat the polymer. Some PNIPAM-SA

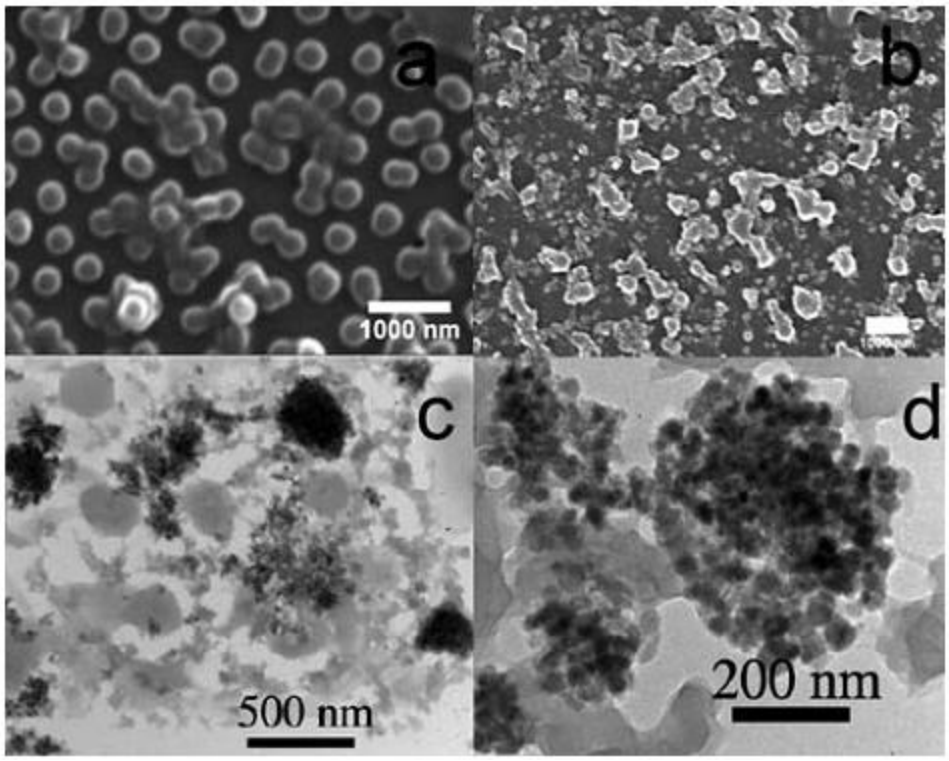

Figure 4.2: (a) SEM image of PNIPAM-SA (b) SEM image of PNIPAM-SA-Fe_3O_4. (c), (d) TEM images of PNIPAM-SA-Fe_3O_4. Taken from R. Regmi *et al.*, *J. Mater. Chem.,* **20**, 6158 (2010).

globules appear to almost completely coated, while others are completely devoid of the nanoparticles. This inhomogeneous distribution of magnetic nanoparticles may adversely affect the response of the composite, since only a fraction of the PNIPAM polymer will be directly affected by nanoparticle heating. There is also evidence for the presence of small Fe_3O_4 nanoparticle agglomerations that are not bound to the PNIPAM-SA framework. This heterogeneous distribution of Fe_3O_4 on the PNIPAM-SA globules may develop due to surface-mediated nanoparticle agglomeration.

To further probe the geometry of the microgels and to determine the LCST for the PNIPAM-SA and the magnetic PNIPAM-SA-Fe_3O_4 samples, we performed

dynamic light scattering (DLS) measurements at different temperatures, as shown in Figure 4.3.

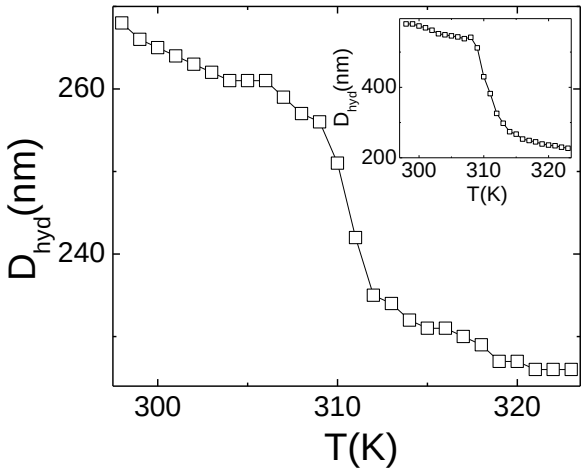

Figure 4.3: Hydrodynamic diameter as a function of temperature for the PNIPAM-SA-Fe_3O_4 composite, as determined using dynamic light scattering measurements. Inset: Hydrodynamic diameter versus temperature for PNIPAM-SA.

It is known that pure PNIPAM has a LCST of 305 K, which we find increases to 310 K with the addition of hydrophilic sodium acrylate [124]. This is shown in the inset to Figure 4.3, which illustrates the volume collapse from a hydrodynamic size of almost 540 nm to approximately 240 nm at this temperature. The addition of Fe_3O_4 nanoparticles shifts the LCST very slightly to 311 K. More remarkably, the size of the PNIPAM-SA-Fe_3O_4 microgel is considerably reduced compared to the parent compound, to only 270 nm, and the fraction change in volume is also much smaller, only 12% for PNIPAM-SA-Fe_3O_4 as compared to 56% for PNIPAM-SA. The reduction in the size of PNIPAM-SA after incorporating Fe_3O_4 nanoparticles may be because of an increased cross-link density due to the presence of iron oxide nanoparticles [40]. Steric hindrance and nanoparticle-nanoparticle interaction

caused by the presence of iron oxide nanoparticles might have hampered the polymer aggregation during LCST, which increased the LCST of PNIPAM-SA-Fe_3O_4 slightly and also caused a smaller change in volume during LCST in PNIPAM-SA-Fe_3O_4 [40]. The microgel sizes extracted from DLS measurements are somewhat larger than what we obtain from SEM and TEM images (Fig. 4.2), which reflects the fact that DLS is sensitive to the hydrodynamic radius of the composites in solution while the electron microscopy images may reflect some volume collapse in the microgel out of solution.

The heat flow out of the sample as a function of temperature for the PNIPAM-SA and PNIPAM-SA-Fe_3O_4 composites and for bare Fe_3O_4 is shown in Fig. 4.4.

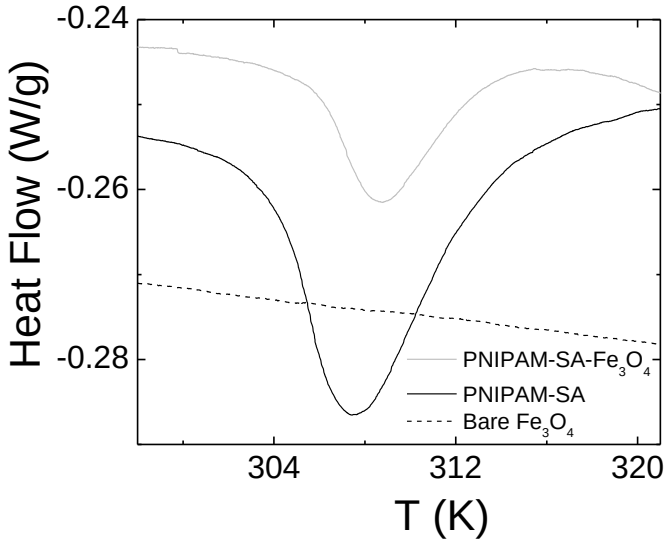

Figure 4.4: Heat flow as a function of temperature measured by differential scanning calorimetry for bare Fe_3O_4 (dotted line), PNIPAM-SA (dashed line), and PNIPAM-SA-Fe_3O_4 (solid line) samples.

For the PNIPAM-SA and PNIPAM-SA-Fe_3O_4 traces, endothermic peaks occur near 308 K and 309 K with changes in enthalpy of approximately 2.34 J/g and 1.04 J/g respectively. The temperatures of these peaks are consistent with the LCST of PNIPAM-SA and PNIPAM-SA-Fe_3O_4 found using DLS measurements, and the magnitude of the enthalpy for the PNIPAM-SA sample is consistent with previous results in the literature [125]. The smaller change in enthalpy for the PNIPAM-SA-Fe_3O_4 sample, as compared to PNIPAM-SA, can be associated with a change in the hydration state of the PNIPAM chains arising from the attachment of Fe_3O_4 nanoparticles. The bare Fe_3O_4 sample does not show any endothermal peak, confirming that the features observed at 308 K and 309 K are due to a structural change in the PNIPAM polymer component.

The magnetic relaxation time τ for the system depends on both Brownian and Néel relaxation, so the frequency dependence of the magnetic susceptibility yields information on changes in these mechanisms. We have measured the in-phase and out-of-phase components of the complex susceptibility of the PNIPAM-SA-Fe_3O_4 ferrofluid as a function of temperature and applied field frequency through the LCST transition. Fig. 4.5a shows the out-of-phase component of the ac susceptibility as a function of temperature for this sample, measured at a frequency of 1000 Hz. This curve shows a clear maximum close to 308 K, corresponding to the LCST of the microgel. At this transition temperature, the PNIPAM-SA polymer changes to a hydrophobic state producing a sharp drop in the hydrodynamic volume of the microgel. In turn, this increases the frequency of Brownian relaxation given

by [126] $f_B=k_BT/3\eta V_H$, producing a peak in the magnetic dissipation. This anomaly in the magnetic dynamics can also be seen by considering the variation of the resonant frequency with temperature. The inset to Fig. 4.5a plots the resonant frequency, determined from the peak in *M"* versus *f* plots (not shown), at different temperatures.

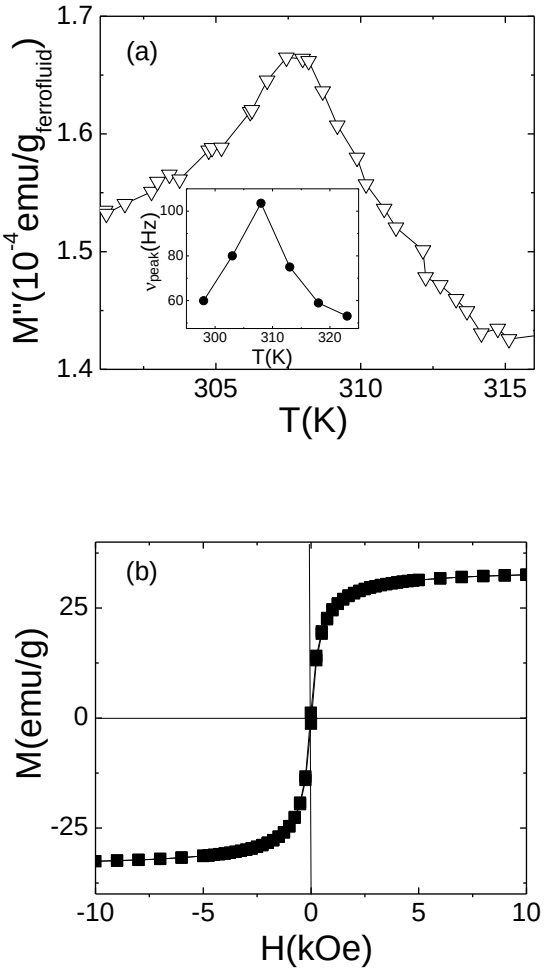

Figure 4.5: (a) Out-of-phase component of the ac magnetic susceptibility measured as a function of temperature for PNIPAM-SA-Fe_3O_4. Inset: Peak frequency as a function of temperature. (b) Room temperature magnetization curve measured for PNIPAM-SA-Fe_3O_4.

The saturation magnetization M_s, remnant magnetism M_r and coercivity H_c are the most important parameters for assessing the suitability of magnetic materials for applications. We plot the room temperature *M (H)* curve measured for lyophilized PNIPAM-SA-Fe_3O_4 in Fig. 4.5b. The saturation magnetization of the composite is 33 emu/g of composite, as compared to approximately 68 emu/g for the bare Fe_3O_4 nanoparticles used in the composite. This implies PNIPAM-SA-Fe_3O_4 contains approximately 50% iron oxide by mass, which is consistent with our estimates of the composition using TGA (see Fig. 4.1). Because of the higher concentration of iron oxide in PNIPAM-SA-Fe_3O_4, the M_s value is relatively large as compared to typical M_s values of such a hybrid material such as 10 emu/g for Fe_{18}PNIPAM-AAS to 20 emu/g for Fe_{38}PNIPAM-AAS [40] consistent with the larger mass fraction of Fe_3O_4 in the microgel. The advantage of the higher value of magnetization of the sample is that it can readily respond to the externally applied alternating magnetic field, although higher iron oxide fractions can negatively impact drug loading fractions in some composites [127]. The sample is also non-coercive at room temperature, which is typical for superparamagnetic nanoparticles, making the composite suitable for biomedical applications.

Having established that a conformal transition occurs in the PNIPAM-SA-Fe_3O_4 microgel at approximately 311 K, we investigated the possibility of using external magnetic fields to heat this composite on short timescale. We plot the increase in the temperature of PNIPAM-SA-Fe_3O_4 samples having different concentrations of magnetic nanoparticles during the application of an external

magnetic field in Fig. 4.6. There is some increase in temperature for the background buffer solution, which may be associated with resistive heating in the induction coil. There is a systematic increase in the magnetic component of heating with nanoparticle concentration. On this plot, the LCST for the composite (see Fig. 4.3) corresponds to a ΔT of approximately 13 K, which is reached within 3 min of applying the external magnetic field. We also note that local temperatures of 314-

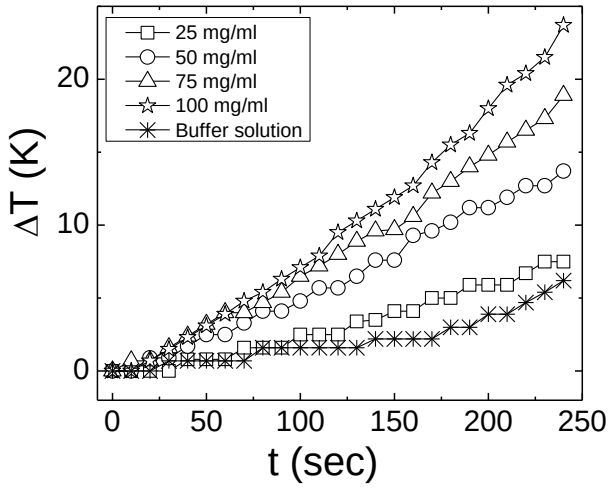

Figure 4.6: Change in temperature of PNIPAM-SA-Fe_3O_4 as a function of time under magnetic hyperthermia, for nanoparticle concentrations ranging from 25 mg/mL to 100 mg/mL as indicated. The open symbols show the response of buffer solution, used as a background control.

318 K are sufficient to kill cancer cells [128], which are obtained within 4 min for the samples having higher concentrations of magnetic nanoparticles.

Having established that magnetic hyperthermia can be used to heat the sample above the LCST, we investigated the loading and release of the anticancer drug mitoxantrone in both the PNIPAM-SA and PNIAPM-SA-Fe_3O_4 composites. To load the samples, we stirred a mixture consisting of 1 mg/ml of mitoxantrone and 25

mg/ml of microgel for 12 hours under ambient conditions. The drug loading fraction was determined to be 100% in PNIPAM-SA-Fe_3O_4 and 65% in PNIPAM-SA. It is unclear why drug loading is more efficacious in the magnetic composite, although this may be related to the electrostatic effects discussed in the following. The drug-loaded PNIPAM-SA-Fe_3O_4 composite was heated using only an applied magnetic field from 298 to 323 K in 4 min, while the drug-loaded PNIPAM-SA sample was heated over the same range of temperatures in 30 min using a water bath. While the drug release fraction determined by following this particular measurement protocol represents a convolution of the release rate at different temperatures with the warming rate, we believe that it provides a useful insight into the release dynamics that will be relevant for clinical applications. However, as the heating rate is relatively constant, as illustrated in Fig. 4.6 for the PNIPAM-SA-Fe_3O_4 composite, we can identify qualitative changes in the temperature dependence of the drug release rate by measuring the amount of drug released as a function of temperature. The integrated amount of drug released from each of these samples at different temperatures is shown in Fig. 4.7a. Recalling that the measuring time for the PNIPAM-SA-Fe_3O_4 sample is only 4 min compared to 30 min for the PNIPAM-SA sample, the release rate for the sample with magnetic nanoparticles is roughly a factor of 8 larger than for the parent sample. This is reflected in Fig. 4.7b, which plots the estimated total drug release *rate* as a function of temperature, assuming a constant heating rate for both measurements. The higher rate of drug release in Fig 4.7b is important for clinical applications because it will deliver large amount of

drug in short time scale avoiding longer exposure of alternating magnetic field. Rather unexpectedly, we do not see any sharp change in the inferred drug release rate at the LCST for either sample, although there may be a slight anomaly for the PNIPAM-SA-Fe_3O_4 sample. This apparent insensitivity of the release rate to the volume change may arise, at least in part, from electrostatic interactions between the positively charged secondary amine groups on the mitoxantrone with the negatively charged carboxylic acid and

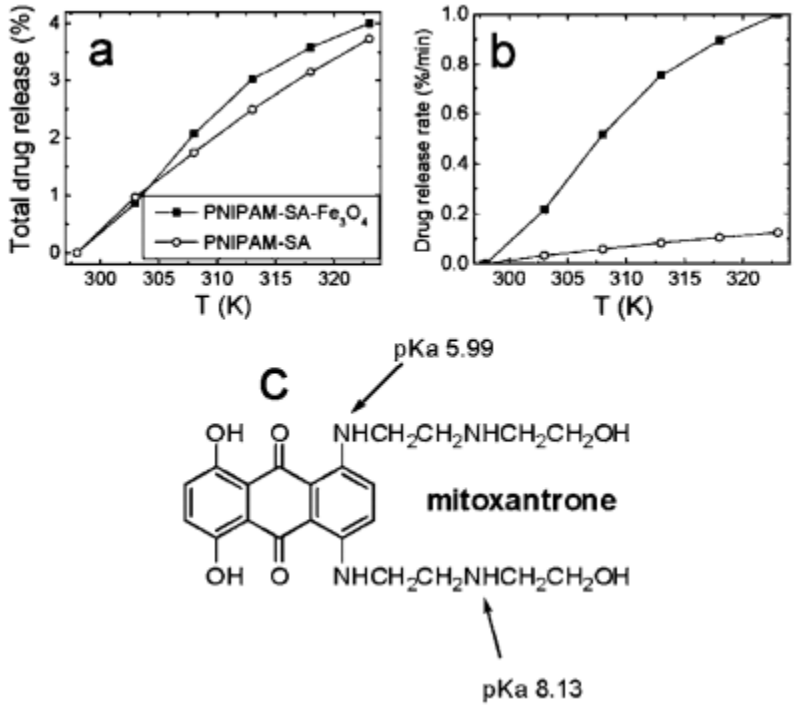

Figure 4.7: (a) Integrated fractional drug release (%) as a function of temperature for mitoxantrone loaded PNIPAM-SA and PNIPAM-SA-Fe_3O_4. (b) Estimated integrated drug release rate for mitoxantrone loaded PNIPAM-SA and PNIPAM-SA-Fe_3O_4 as a function of temperature assuming a constant heating rate over 4 min total for PNIPAM-SA-Fe_3O_4 and 30 min total for PNIPAM-SA. (c) Structure of mitoxantrone. Taken from R. Regmi *et al.*, *J. Mater. Chem.,* **20**, 6158 (2010).

sulfonate groups on the microgel. Such electrostatic interactions could obscure changes in release rate from the conformal effects produced by hyperthermia. As

shown in Fig. 4.7c, mitoxantrone has two amine groups having dissociation constants of pKa=5.99 and pKa=8.13 [129]. pK_a is $-\log_{10}K_a$, where K_a is the acid dissociation constant defined as the ratio of the product of concentration of ionized molecule to the concentration of unionized molecules given in units of mol/L. At the pH used in these investigations (pH=7.4), the protonation for the amine group is calculated by using the following relation [130]:

$$pH = pKa + \log\left(\frac{1-\theta}{\theta}\right) \quad \text{.....(4.1)}$$

Where θ is the degree of protonation. Using equation (4.1), we found the protonation for amine group having pK_a=5.99 and pK_a = 8.13 as 3.74 % and84.3 % respectively . This will lead to an overall positive charge at physiological pH. Conversely, we find a zeta potential of -21.6 mV for the bare PNIPAM–SA polymer, which drops to -13.9 mV with the incorporation of Fe_3O_4 nanoparticles, consistent with a positive charge on the nanoparticles themselves. This zeta potential increases to -33.8 mV with the addition of sodium polystyrene sulfonate used to improve the colloidal stability, providing the negative charge to compensate the positive mitoxantrone molecules. Alexiou *et al.* [131] have also discussed ionic binding between cationic mitoxantrone and anionic ferrofluid. It could be possible to mitigate these electrostatic interactions by selecting a more suitable drug or developing a technique to covalently embed the magnetic nanoparticles in the microgel to allow a reduction of the sodium acrylate monomer content. While these electrostatic effects are expected to provide the dominant mechanism for controlling the drug release in these

composites, other interactions may also play a role and should be considered in future studies. A similar weak dependence of drug release on sample volume was observed in studies on doxorubicin loaded in PNIPAM [120]. Coughlan *et al.* [106] have also shown that drug release from the PNIPAM hydrogel depends on the solubility and chemical nature of drugs. The drug release rate from our PNIPAM-SA-Fe_3O_4 samples (1 %/min average over this temperature range) is about three times larger than that found by Purushotham *et al.* [120] (0.31 %/min), although the release rate from our PNIPAM-SA samples is smaller. Because the magnetic heating in the PNIPAM-SA-Fe_3O_4 composite is much faster than the water bath heating for PNIPAM-SA, the rate of drug release from the magnetic microgel is much faster than the rate of release from the parent sample. As the efficacy of mitoxantrone is improved at elevated temperatures [132], we speculate that in addition to providing for controlled release, the thermal effects arising from magnetic heating may also contribute to improved outcomes for therapies based on this PNIPAM-SA-Fe_3O_4 composite system.

4.2.3 CONCLUSIONS

We were able to successfully combine Fe_3O_4 nanoparticles with PNIPAM polymer to produce a magnetic microgel composite, which exhibits a conformal transition at an LCST of approximately 311 K. The composites have a relatively high saturation magnetization, on the order of 33 emu/g, allowing for magnetic heating. The magnetic microgels can be heated to temperatures above the LCST

with the application of an external alternating magnetic field for only a few minutes. We investigated the loading and release of the anti-cancer drug mitoxantrone into the PNIPAM-SA-Fe_3O_4 composite and into the parent PNIPAM-SA composite. Interestingly, the drug upload fraction was larger (100 %) for the magnetic microgel than for the non-magnetic PNIPAM-SA parent composite (65 %) , and the estimated release rate was much higher, being approximately a factor of 8 larger. Although the drug release does not appear to be particularly sensitive to the LCST transition in the PNIPAM-SA-Fe_3O_4 microgel, this system offers the possibility of combining the functionality of magnetic nanoparticles with the polymer matrix to allow controlled drug release using only non-invasive magnetic fields in a short interval of time.

4.3 DRUG RELEASE FROM DEXTRAN COATED IRON OXIDE

Motivated by the success in using the PNIPAM/Fe_3O_4 polymer/nanoparticles composites from drug loading and hyperthermia controlled release, we extended these investigations to other systems. Since dextran coated nanoparticles can evade RES system and can circulate inside body, drug release from dextran coated iron oxide nanoparticles is of great interest. Saboktakin *et al.* [133] has studied release of a model drug 5- aminosalicyclic acid from 70 kDa amine functionalzied dextran coated iron oxide nanoparticles and found a release of about 85 % in about 15 h. Babincova *et. al.* [134] observed substantial release of 6-carboxyfluorescein dye

triggered by laser from dextran-Fe_3O_4 encapsulated liposomes. In addition, Perlstein *et. al.* [135] have shown the possibility of drug delivery into the brain by using 35 to 45 kDa dextran coated iron oxide nanoparticles. In this context, we did the drug release study from different chain length dextran (15-20 kDa and 60-90 kDa) coated iron oxide nanoparticles to investigate whether the different chain length of dextran controls the drug release or not.

We synthesized iron oxide nanoparticles coated with 15-20 kDa and 60-90 kDa molecular mass dextran as described in section 2.1.3. An anticancer drug, camptothecin, was loaded by a solvent evaporation method. 1 mg of camptothecin was loaded in each of the two samples with a loading efficiency was 100 %. The drug release into PBS was monitored as a function of time using a Cary 50 Bio UV-Visible spectrophotometer.

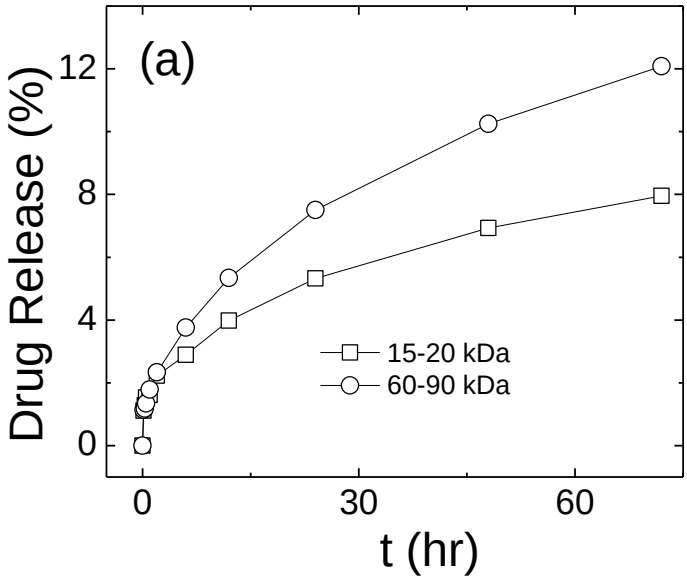

Figure 4.8: Drug release from 15-20 kDa and 60-90 kDa dextran coated sample.

The drug release profile for these two different samples is shown in Fig 4.8. The integrated fractional drug release from the 15-20 kDa and 60-90 kDa dextran coated nanoparticles samples was 8 and 12 % respectively in 72 h. At short time,

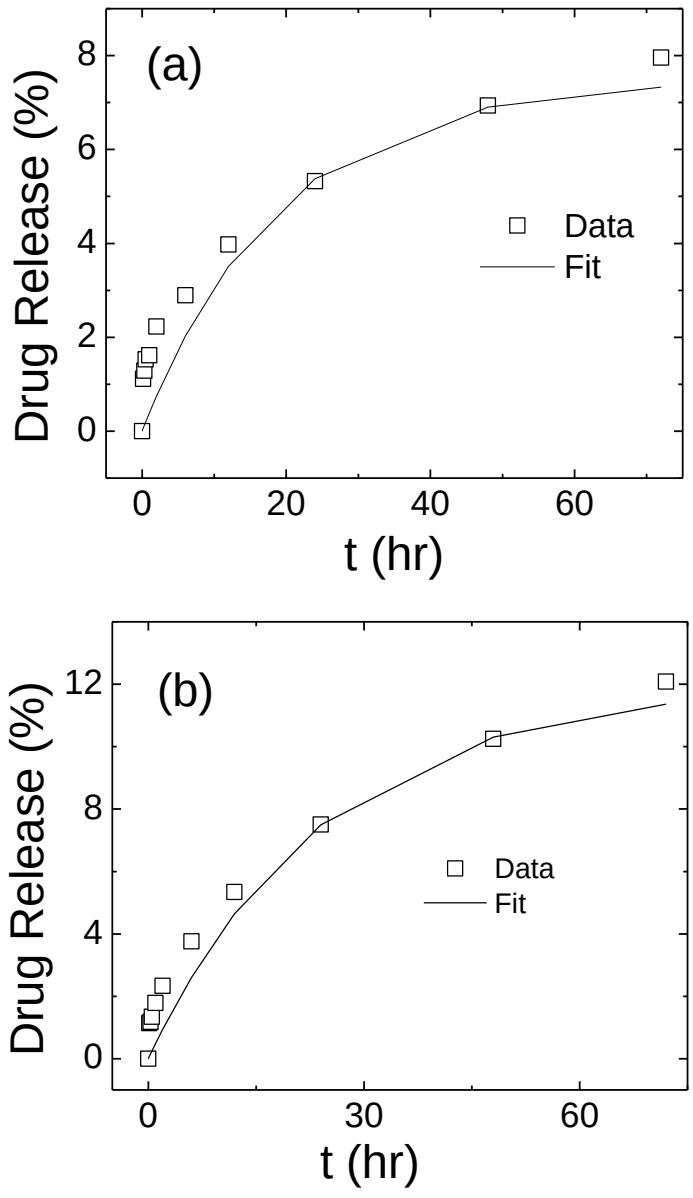

Figure 4.9: Fit of equation (1) to the drug release of (a) 15-20 kDa dextran coated sample and (b) 60-90 kDa dextran coated sample.

when the concentration of drug in the composite is highest, the release rate is large, while as the drug leaves the composite, the rate is reduced. These release profiles can be fit to an exponential relaxation, with different characteristic relaxation times for the two molecular masses as:

$$\text{Drug release} = A_o (1-e^{-t/\tau}) \quad \ldots\ldots\ldots\ldots\ldots\ldots\ldots\ldots\ldots\ldots\ldots\ldots (4.2)$$

Where A_o is saturation value of drug release and τ is the time constant for drug release. The fits to Eq. (4.2) for the 15-20 kDa dextran and 60-90 kDa dextran is shown in Figs. 4.9a and b respectively.

The value of A_o is near 7.5 and 12 % for 15-20 and 60-90 kDa dextran coated iron oxide respectively, which have relaxation times are close to 19 and 24.5 hrs. There are a number of factors that could influence the release rate from the composite. The number of binding sites for the drug to the polymer likely varies with chain length. Since the longer chain dextran has more sites, and these will be located further from the magnetic nanoparticle on average, we expect the asymptotic drug fraction released should be larger, as observed experimentally. However, we also expect that the diffusion rate for the drug through the polymer coating may be smaller for the high molecular mass dextran as compared to the lower mass dextran, leading to a larger time constant. Further studies will be required to properly determine the rate-limiting step responsible for drug release from dextran coated iron oxide nanoparticles.

To conclude, we studied drug release from different chain length dextran coated iron oxide nanoparticles and found higher drug release from longer chain length dextran coated samples. This offers an exciting possibility for controlled drug release from different chain length dextran coated nanoparticles, since the time constant for the release may be tuned by dextran mass, and also allows the possibility of engineering a very flat release rate by combining different molecular mass dextrans together.

4.4 CELL NUCLEUS TARGETING

While these previous studies of functionalized iron oxide nanoparticles in solution offer important insight into their physical properties, it is necessary to understand the interactions of these nanoparticles with living cells. As a first step in confirming that these nanoparticles may be viable for biomedical applications, we confirmed that they are non-toxic in sufficiently small quantities.

Having confirmed that these iron oxide nanoparticles are non-toxic, at least in sufficiently small concentrations, the next step was to determine whether the nanoparticles are able to penetrate into the cell. More specifically, many applications, including brachytherapy and transfection, require the nanoparticles to localize at the cell nucleus. For example, Polyakov *et al.* [136] has localized toxic radioisotope at the cell nucleus to improve radiotherapy. Snyder et al. [137] has used tat peptide for the enhanced delivery of therapeutic DNA into cell nucleus. Since tat peptide is known to target cell nucleus [136,137], we labeled dextran

coated iron oxide nanoparticles with tat peptide as described in section 2.1.4. The specific aim of this study is to localize iron oxide nanoparticles near the cell nucleus to enhance the effects of radiation brachytherapy treatment. Since glioblastoma multiforme (GBM) tumors show limited response to current therapies, our goal is to introduce iron oxide nanoparticles to the GBM cell nucleus, which will down-convert penetrating high energy x-rays to more damaging, lower energy radiation to kill the cancerous cells. As a first step in this project, we have conducted in vitro studies to target the nucleus of human glioblastoma cells by tat conjugated iron oxide nanoparticles.

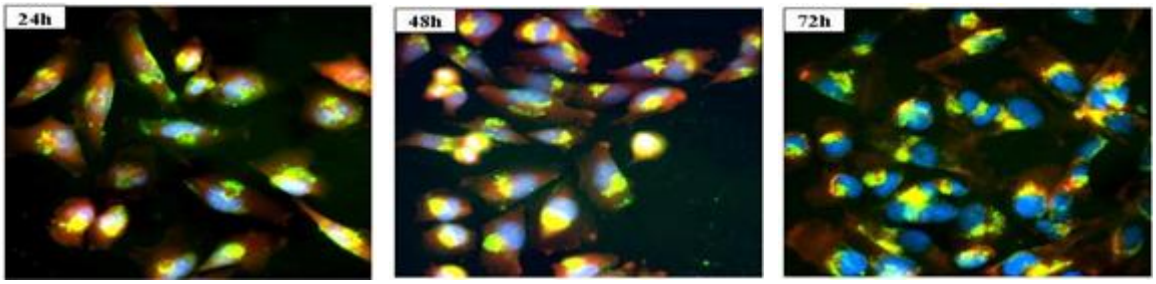

Figure 4.10: Time dependent study of Tat peptide labeled iron oxide nanoparticles penetrating cell nucleus.

We labeled tat counjugated iron oxide nanoparticles by fluoro isothicyanate (FITC) dye, which makes the nanoparticles visible in fluorescent imaging. To confirm that the iron oxide nanoparticles are reaching the cell nucleus, we stained the cell nucleus with blue colored DAPI and the cytoplasm by red phalloidin-TRITC. Figure 4.10 shows overlapping confocal microscopy images of green and blued (green + blue = cyan) 24 h after the injection, 48 h after injection, and 72 h after injection. These images establish that the iron oxide nanoparticles are mainly localized at the

cell nucleus, although there are residual nanoparticles in the surrounding cytoplasm. Maximum nanoparticles concentration at the cell nucleus occurs after 48 h. Since the green FITC dye was attached to the dextran coating, and not directly to the iron oxide nanoparticle , we also did a Prussian blue staining to map the iron distribution, as shown in Fig. 4.11. These images confirm that the iron oxide nanoparticles have reached the cell nucleus, eliminating the possibility that the dextran could have separated from the nanoparticles during the process.

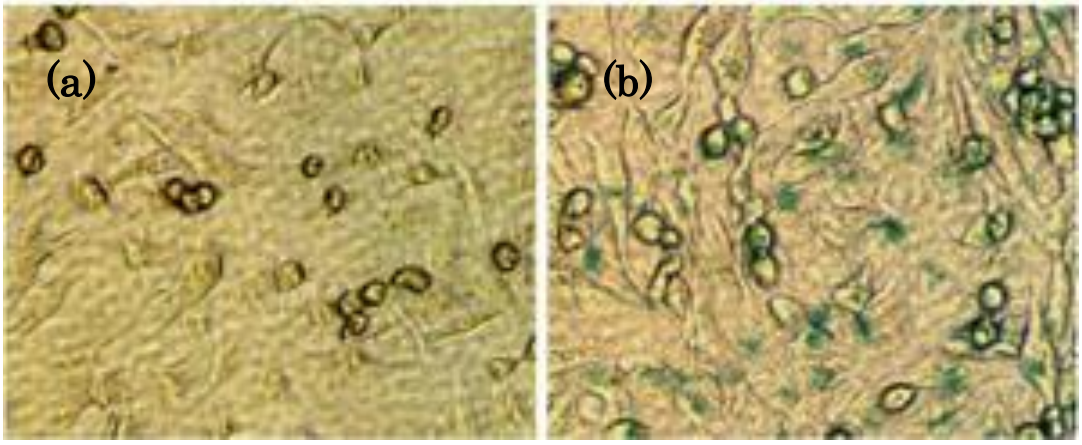

Figure 4.11: Prussian blue staining of (a) control glioblastoma cells without tat conjugated nanoparticls (b) glioblastoma cells with nanoparticles.

We see in Fig 4.11 that the control glioblastoma cells (left panel) do not show any signature after Prussian blue staining whereas the cells with tat conjugated nanoparticles (right panel) do show a clear blue staining inside the cell nucleus. We also did magnetic measurements on the cells using a SQUID magnetometer to quantify the iron oxide nanoparticles concentration inside the cell nucleus. The M(H) curve is shown in Fig 4.12. We have done the background subtraction in the M(H) of Fig 4.12. The saturation of the curve indicated the presence of

superparamagnetic iron oxide nanoparticles. Given that these iron oxide nanoparticles have a saturation magnetization of 60 emu/g, we calculated the number of iron oxide nanoparticles per cell from the saturation magnetization in

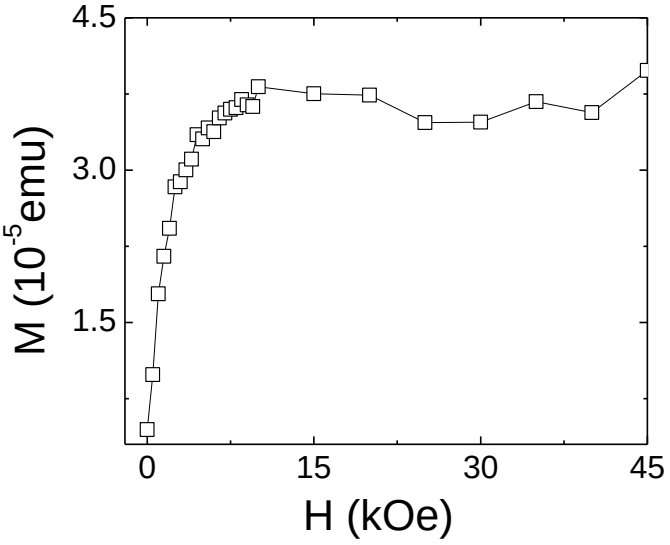

Figure 4.12: M(H) curve of human glioblastoma cells with iron oxide nanoparticles.

Fig. 4.12. The number of iron oxide nanoparticles per cell is close to 6 x 10^6, which is equivalent to 21 picogram of iron oxide per cell. It is important to know this value of the concentration in order to estimate the efficacy of using these nanoparticles to improve the outcomes for radiation brachytherapy. It is also crucial to have the right concentration of iron oxide into cell to avoid the toxicity due to iron oxide itself. We had done a cytoxicity study and had found the concentration 21 picogram iron oxide per cell is not toxic to cell. We had also done a separate study where we found 250 nanogram of iron oxide per cell was not toxic whereas concentrations above it were toxic to cells.

In conclusion, we successfully synthesized iron oxide nanoparticles labeled with tat peptide. Our preliminary studies also show, tat peptide has taken these nanoparticles to the nucleus of the cell and the internalization of iron oxide nanoparticles is highest after the incubation period of 48 h. We also confirmed the presence of iron oxide nanoparticles inside cells using magnetic measurement, which also help us to quantify the amount of iron oxide nanoparticles inside cells.

4.5 SUMMARY

We did the magnetic hyperthermia triggered in vitro drug release study. Drug release rate of mitoxantrone loaded into the magnetic thermosensitive polymer PNIPAM in the presence of alternating magnetic field of 70 Oe is 8 times larger compared to bare PNIPAM using water bath. This allows a short time exposure of an alternating magnetic field to get higher amount of drug release. We also did the camptothecin drug release from 15-20 kDa and 60 -90 kDa dextran coated sample as a function to time. We found higher drug release from higher molecular weight dextran coated sample.

We successfully synthesized the tat peptide labeled dextran coated iron oxide nanoparticles. In vitro studies suggest that these tat conjugated nanoparticles have penetrated the nucleus of the human glioblastoma cells, which has a great potential for the localized radiation therapy.

Chapter 5

MAGNETIC AND DIELECTRIC PROPERTIES OF NANOPARTICLES

5.1 INTRODUCTION

Nanocrystalline materials have high surface to volume ratios and can show properties different from their bulk counterparts. Bulk magnetic materials are comprised of a number of different domains. Spins in each domain are aligned in same direction, with these domains separated by walls having more complex spin arrangements. In single domain magnetic nanoparticles, behaviors arising from domain walls are absent, which gives different magnetic and electric properties than bulk materials. Since magnetic nanoparticles have many applications, including magnetic sensors and transducers, microwave adsorption, electromagnetic wave shielding, and high density information storage [138], it is of great interest to investigate the dielectric and magnetic properties of these systems. In addition, coating nanoparticles with surfactants and dispersing them in carrier liquids, producing a ferrofluid, offers the possibility of producing new functionalities. Dielectric studies of these ferrofluids can also give information about stability, homogeneity and structure of the particles in solution [139]. Magnetic measurement on these ferrofluids can provide information on the magnetization and dynamics of nanoparticles embedded in polymers. Finally, it has also been observed that

dielectric anomalies may accompany magnetic transitions [140], so dielectric studies of nanoparticles may allow additional insight into their magnetic properties.

Many widely studied magnetic nanoparticles are spinel oxides, which can be represented by the general form of AB_2O_4, with A and B representing the tetrahedral and octahedral sites respectively in the spinel lattice. These materials are attractive systems for the study of complex magnetic order. Both the tetrahedral A site ions and the octahedral B site ions can be magnetic, which, in combination with the fact that the B site ions sit on a pyrochlore lattice, leads to the opportunity to investigate a wide range of complex magnetic behaviors in spinels [141,142]. The magnetic and electric properties of these spinel oxides also depend on the choice and distribution of cations between the A and B sites. We have studied the magnetic and dielectric properties of bare Mn_3O_4 and dextran coated iron oxide nanoparticles.

5.2 SUPPRESSION OF LOW TEMPERATURE MAGNETIC STATES IN Mn_3O_4 NANOPARTICLES

The complex magnetic structures arising in Mn_3O_4, ideally having Mn^{2+} at the A sites and Mn^{3+} at the B sites, have been discussed theoretically [142-144], and studied experimentally [145-147]. Bulk Mn_3O_4 exhibits a tetragonal Jahn-Teller distortion at the Mn^{3+} site at high temperatures to the $I4_1/amd$ space group, and orders ferrimagnetically into a Yafet-Kittel phase at T_N=42 K. At lower temperatures, Mn_3O_4 undergoes a transition to an incommensurate phase at 40 K and a transition to a commensurate phase at 34 K, which is cell doubled relative to

the Yafet-Kittel phase. Recently, the magnetodielectric response in Mn_3O_4 has been investigated in both ceramic [148] and single crystal samples [149], where it is observed that dielectric anomalies accompany the magnetic transitions.

The suppression of magnetic ordering transitions in finite size systems has been studied theoretically and experimentally. The magnetic ordering temperature is predicted to vary with the system size according to [150]:

$$\frac{T_N(\infty)-T_N(d)}{T_N(\infty)}=\left(\frac{\xi_0}{d}\right)^{\lambda} \quad \text{.....(5.1)}$$

with $T_N(\infty)$ and $T_N(d)$ the bulk and nanoscale magnetic ordering temperatures respectively, ξ_0 the T=0 correlation length. λ is the exponent for finite size scaling, related to the critical exponent ν, which is expected to vary from λ=1 for mean field transitions [151] to λ=2 for Ising spins [152]. This relation has been experimentally confirmed in a number of antiferromagnets, including CoO [150] and Cr [153] films and Co_3O_4 nanoparticles [154].

Studies on other nanoscale magnetic materials have established that magnetic structures can be completely suppressed in nanoparticles, for example, the helical antiferromagnetic order developing in bulk FeP appears to be absent in FeP nanoparticles [155]. Mn_3O_4 is a particularly attractive system for the study of finite size effect on magnetic transition temperature, because it exhibits three distinct magnetic transitions. Although there have been several studies on nanomaterials incorporating Mn_3O_4, many of these have involved composite systems, such as

Mn/Mn_3O_4 [156] or MnO/Mn_3O_4 [157] core-shell nanoparticles, and focused on the ferrimagnetic transition on Mn_3O_4, which is found to be at most slightly suppressed in finite size systems [158]. Within this framework, we have carefully studied the magnetic and thermodynamic properties of Mn_3O_4 nanoparticles at low temperatures to investigate whether the transition temperature of the other two magnetic phases show additional suppression compared to the onset of ferrimagnetic order.

5.2.1 EXPERIMENTAL DETAILS

We used a co-precipitation method to synthesize Mn_3O_4 nanoparticles as described in section 2.1.10. We collected X-ray diffraction patterns using Cu Kα radiation on a Rigaku Ru2000 rotating anode diffractometer to confirm the crystalline structure of the nanoparticles. Raman spectra were taken at room temperature using a Ar^+-ion laser (514.5 nm) with a Triax 550 detector. AC and DC magnetization, and specific heat capacity measurement were taken using standard options on a Quantum Design Physical Property Measurement System (PPMS). For AC magnetization measurement, we packed about 20 mg of nanoparticles in a gelatin capsule and compressed with cotton to avoid the motion of the nanoparticles during measurement. For the specific heat capacity measurement, we mixed 60 mg of Mn_3O_4 nanoparticles with silver powder in 1:1 ration by weight and cold pressed into a solid pellet to ensure a good thermal contact.

5.2.2 RESULTS AND DISCUSSIONS

X-ray diffraction patterns are shown in Fig 5.1a and all the peaks can be labeled to the crystalline structure of Mn_3O_4. This implies that no impurity phases are present in these samples. We estimated the size of nanoparticles to be 15 nm using the Debye-Scherrer equation $d=0.9\lambda/\beta\cos\theta$, where β is full width half maximum (FWHM) of the peak. TEM images of Mn_3O_4 nanoparticles are shown in Fig 5.1c. These show some agglomeration and the nanoparticles are not uniformly spherical. The average diameter of these nanoparticles is 25 nm with a standard deviation of approximately 4 nm. The size of these nanoparticles determined from TEM images is greater than that found from XRD because of the amorphous surface layer on the particles. We also took Raman spectra for these Mn_3O_4 nanoparticles (compressed into a pellet) at room temperature. We found the same peaks observed as in bulk Mn_3O_4 with some redshift and broadening of the peaks, again confirming the phase purity of these Mn_3O_4 nanoparticles. Room temperature Raman spectra for nanoparticles and bulk Mn_3O_4 are shown in Fig. 5.1b. The high intensity peak at 654 cm^{-1} in bulk Mn_3O_4 is shifted to 640 cm^{-1} in Mn_3O_4 nanoparticles. Similarly, the low intensity peaks at 365 cm^{-1} , 313 cm^{-1} and 278 cm^{-1} in bulk Mn_3O_4 are shifted to 350 cm^{-1} , 295 cm^{-1}, and 272 cm^{-1} respectively in the Mn_3O_4 nanoparticles. Han *et al.* have also reported similar redshifts for Mn_3O_4 nanoparticles prepared in mesoporous silica [159]. We did zero field cooled (ZFC) and FC (field cooled) measurements at a field of 1 kOe. These ZFC and FC curves are shown in Fig. 5.2. The ZFC curve shows a peak at 40 K and a ferrimagnetic transition at 42 K with a

sharp rise in magnetization. We confirmed the ferrimagnetic transition falls between 42 and 43 K from an Arrot plot, as shown in the inset of Fig 5.2. The

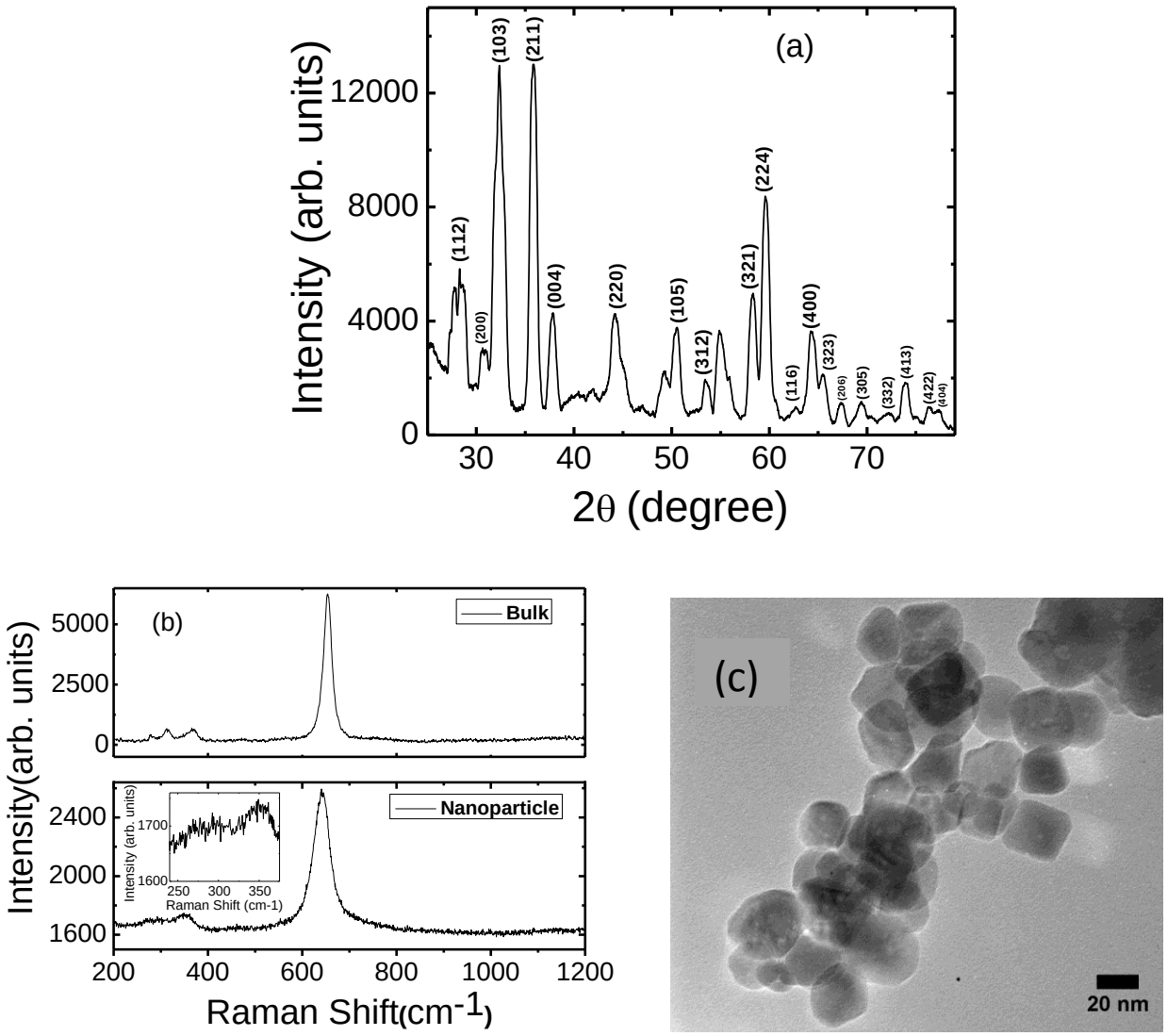

Figure 5.1: (a) X-ray diffraction spectrum for Mn_3O_4 nanoparticles (b) Raman spectra for bulk and nanoparticle Mn_3O_4. Inset: Magnified peaks of lower wave number (c) TEM images of Mn_3O_4 nanoparticles. Taken from *J. Magn. Magn. Mater.*, **321,** 2296 (2009).

ferrimagnetic transition has been observed in bulk Mn_3O_4 at 42 K [148]. The peak at 40 K is likely related to superparamagnetic blocking in the Mn_3O_4 nanoparticles;

this feature is not observed in bulk Mn_3O_4 [148]. However, bulk Mn_3O_4 does exhibit a splitting of ZFC and FC curve [148], but this may be associated with the incommensurate magnetic transition. Moreover, the rounded peak in the ZFC curve in the Mn_3O_4 nanoparticles, which was not observed in bulk Mn_3O_4, is consistent with the polydispersity of the nanoparticles. The saturation magnetization shown by FC curve in Mn_3O_4 nanoparticles is one third of that in bulk Mn_3O_4.

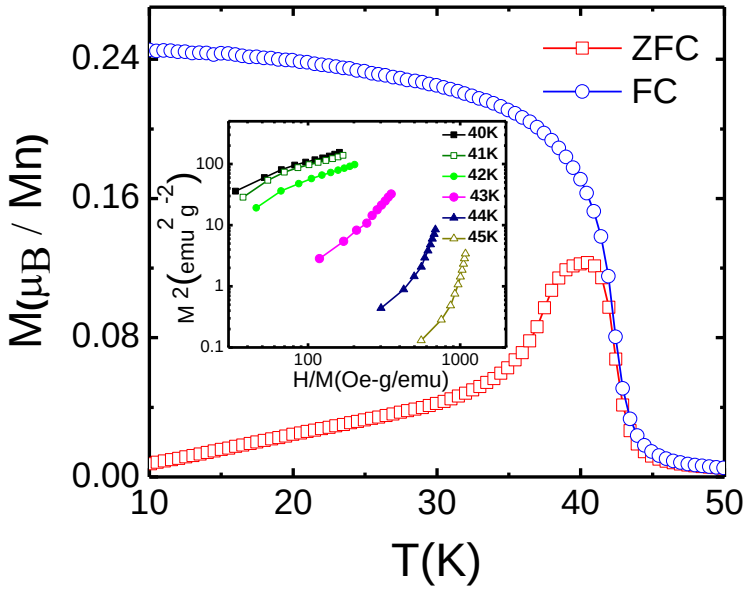

Figure 5.2: Zero field cooled (ZFC) and Field cooled (FC) magnetization curves for Mn_3O_4 nanoparticles measured at 1000 Oe. Inset: Arrot plot showing ferrimagnetic transition between 42 and 43 K.

This decrease in magnetization is likely due to the presence of disordered surface spins in magnetic nanoparticles [160,161]. Most significantly, we do not observe any other magnetic transition between 10 K and 42 K in Mn_3O_4 nanoparticles, while bulk samples are known to show other ordering transitions at 34 and 40 K [148].

We also measure the AC susceptibility as a function of temperature at 1 and

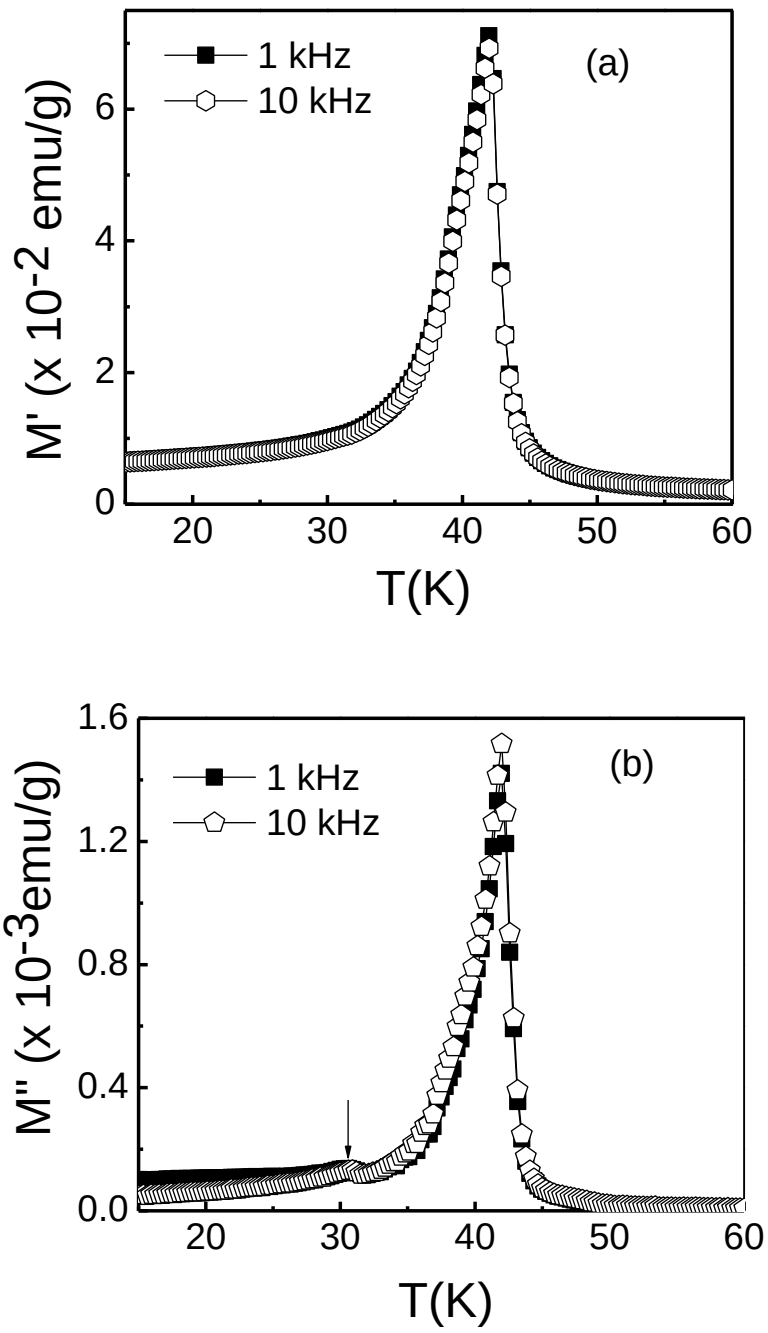

Figure 5.3: (a) Real and (b) imaginary ac susceptibility of the Mn_3O_4 nanoparticles measured at f=1 kHz and f=10 kHz. The arrow indicates the onset of the frequency dependent magnetic response we associate with surface spins.

10 kHz. Figs. 5.3 a and b show the real and imaginary parts of the AC susceptibility as a function of temperature at different frequencies. Both the real and imaginary

part of the AC susceptibility show peaks at 42 K corresponding to the Yafet-Kittel magnetic ordering transition. The in-phase component of AC susceptibility does not show a signature for any other magnetic transition from 15 K to 42 K. However, the out-of-phase component shows some anomaly near 30 K, below the cell doubled phase transition seen in bulk at 33 K [148]. This anomaly may instead be due to the freezing of surface spins in magnetic nanoparticles, which have been also reported in the literature for a number of different magnetic nanoparticles system [162,163].

We also measured the heat capacity measurement from 25 K to 50 K, which is plotted in Fig. 5.4. This heat capacity measurement shows a thermodynamic phase transition at 42 K corresponding to ferrimagnetic Yafet-Kittel ordering. There is no other thermodynamic transition in the temperature range, consistent

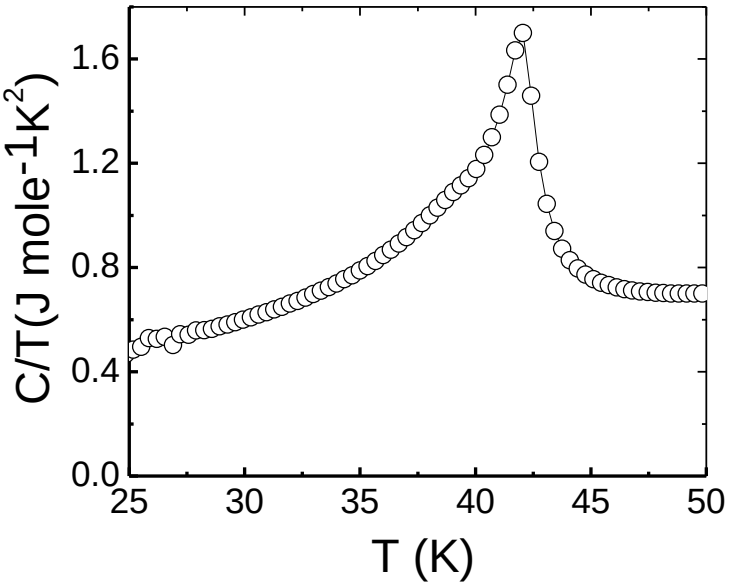

Figure 5.4: Specific heat plotted as a function of temperature for the Mn_3O_4 nanoparticle sample.

with the AC susceptibility measurements. The entropy associated with the magnetic ordering of the Mn_3O_4 nanoparticles is one half as large as that of bulk Mn_3O_4. This is roughly consistent with the reduction of the net magnetic moment by a factor of one third in nanoparticles as compared to bulk Mn_3O_4. This implies that there is a layer of spins that do not order magnetically at the Néel temperature but remain as an amorphous surface spin layer.

All these difference measurements suggest that the Mn_3O_4 nanoparticles have only the single ferrimagnetic Yafet-Kittel phase transition near 42 K, which is within the few percent of transition temperature observed in bulk Mn_3O_4. However, other two transitions observed in bulk Mn_3O_4 below 42 K are absent in nanoparticles. This may be partially because of finite size effect. The wavelength of the incommensurate magnetic structure exceeds tens of chemical unit cells, which is longer than 10-20 nm in case of Mn_3O_4 nanoparticles. Since the wavelength of incommensurate magnetic structure is larger than the magnetic size of the Mn_3O_4 nanoparticles, 15 nm, this incommensurate phase might not develop in these nanoparticles. The cell doubled phase, which develops below 34 K in bulk Mn_3O_4, has a c-axis of length 8 nm, which is about half the size of the Mn_3O_4 nanoparticles. While there is a possibility that these two low temperature magnetic transitions might be suppressed by finite size effects, there could be also other mechanisms responsible. Equation (5.1) parameterizes the suppression of magnetic transitions due to finite size effects. For the cell double phase, the magnetic transition temperature has been suppressed by much more than the factor of two. Using

equation (5.1), with ξ_0 approximately equal to the wavelength of the magnetic structure, we found a scaling exponent $\lambda>4$, which has no existing explanation. Therefore, we also propose that surface spins in Mn_3O_4 nanoparticles may also contribute to the suppression of the cell doubled magnetic transition in Mn_3O_4 nanoparticles.

These thermodynamic and magnetic measurements suggest that 30 % to 50 % of the Mn spins do not contribute to ordering at the ferrimangetic transition. Local interaction with amorphous surface spins may play a large role in the suppression of lower temperature magnetic transitions as compared to finite size effect. These surface spins might have a smaller effect on the ferrimagnetic transition since the transition is above the blocking temperature of Mn_3O_4 nanoparticles (Fig. 5.2) and the spins are fluctuating in paramagnetic phase. Below Yafet-Kittel transition, the surface spins starts freezing as indicated by Fig 5.3b. These freezing surface spins produce static random field, which might have provided the additional barrier to present the low temperature magnetic transition in Mn_3O_4 nanoparticles.

5.2.3 CONCLUSIONS

In Mn_3O_4 nanoparticles, the Yafet-Kittel phase transition is present while the incommensurate and cell doubled phase transition observed in bulk Mn_3O_4 are absent above at least 15 K. Both thermodynamic and magnetic measurements show the presence of a Yafet-Kittel transition and the suppression of other two

transitions. We also observed superparamagnetic blocking and surface spin freezing based on DC and AC magnetization respectively. We propose that the suppression of the low temperature magnetic transitions in Mn_3O_4 nanoparticles is due to disordered surface spins in addition to finite size effect.

5.3 DIELECTRIC MEASUREMENTS ON FERROFLUID

Considering the dielectric response, ferrofluids should be considered as a heterogeneous dielectric mixture consisting of magnetic nanoparticles coated with charged surfactant and dispersed in dielectric liquid. This allows several dielectric relaxation processes in this complex fluid. The distribution of counter-ions around the particles in the presence of electric field leads to the polarization of particles, which is responsible for low frequency dielectric relaxation [113]. At high frequencies and low temperature, an interfacial relaxation process occurs because the mobility of ions around the particles is insufficiently rapid to follow the change in electric fields [164]. Additional contributions to the dielectric response of ferrofluids come from relaxation in the carrier liquid and from the intrinsic properties of the magnetic nanoparticles comprising the ferrofluid. Dielectric studies on ferrofluid provide information about the structure, stability, homogeneity, and dielectric relaxation processes in the system [139]. Dielectric measurement while applying a magnetic field on ferrofluid can yield insight into the correlation between the dielectric behavior and pattern formation in the ferrofluid. Since magnetic nanoparticles in solution form chains under an applied magnetic

field, magnetic fields can change dielectric behavior of a ferrofluid. This can allow one to indirectly probe the distribution of nanoparticles in a ferrofluid under an applied magnetic field by measuring the dielectric behavior. In general, a change in dielectric behavior with an applied magnetic field is referred as a magneto-dielectric effect, and, in ferrofluids, these properties have generally only investigated only near or above room temperature. Malaescu *et al.* [165] has used dielectric spectroscopy of magnetite nanoparticles dispersed in kerosene to analyze the presence of particle agglomeration inside a ferrofluid. Nasri *et al.* [139] has observed magneto-dielectric anisotropy after applying continuous magnetic field on manganese ferrite based ferrofluid. We have studied the dielectric behavior of dextran coated Fe_3O_4 dispersed in 0.5 M NaOH as function of temperature, frequency, and applied magnetic field to investigate field-induced changes in the nanoparticles distribution and magnetodielectric coupling in the ferrofluid.

5.3.1 EXPERIMENTAL DETAILS

We synthesized dextran coated Fe_3O_4 nanoparticles that were dispersed in 0.5 M NaOH as described in the section 2.1.3. For the dielectric measurement, which required the ferrofluid be loaded into vacuum tight cell capable of withstanding low temperatures, we designed a custom dielectric cell. This brass cell is cylindrical with a diameter of ~ 18.5 mm (0.730") and a height of 10.6 mm (0.42"). It is fabricated from separate upper and a lower halves to allow the dielectric liquid to be loaded. Each half contains a circular conducting plate used an electrode, which

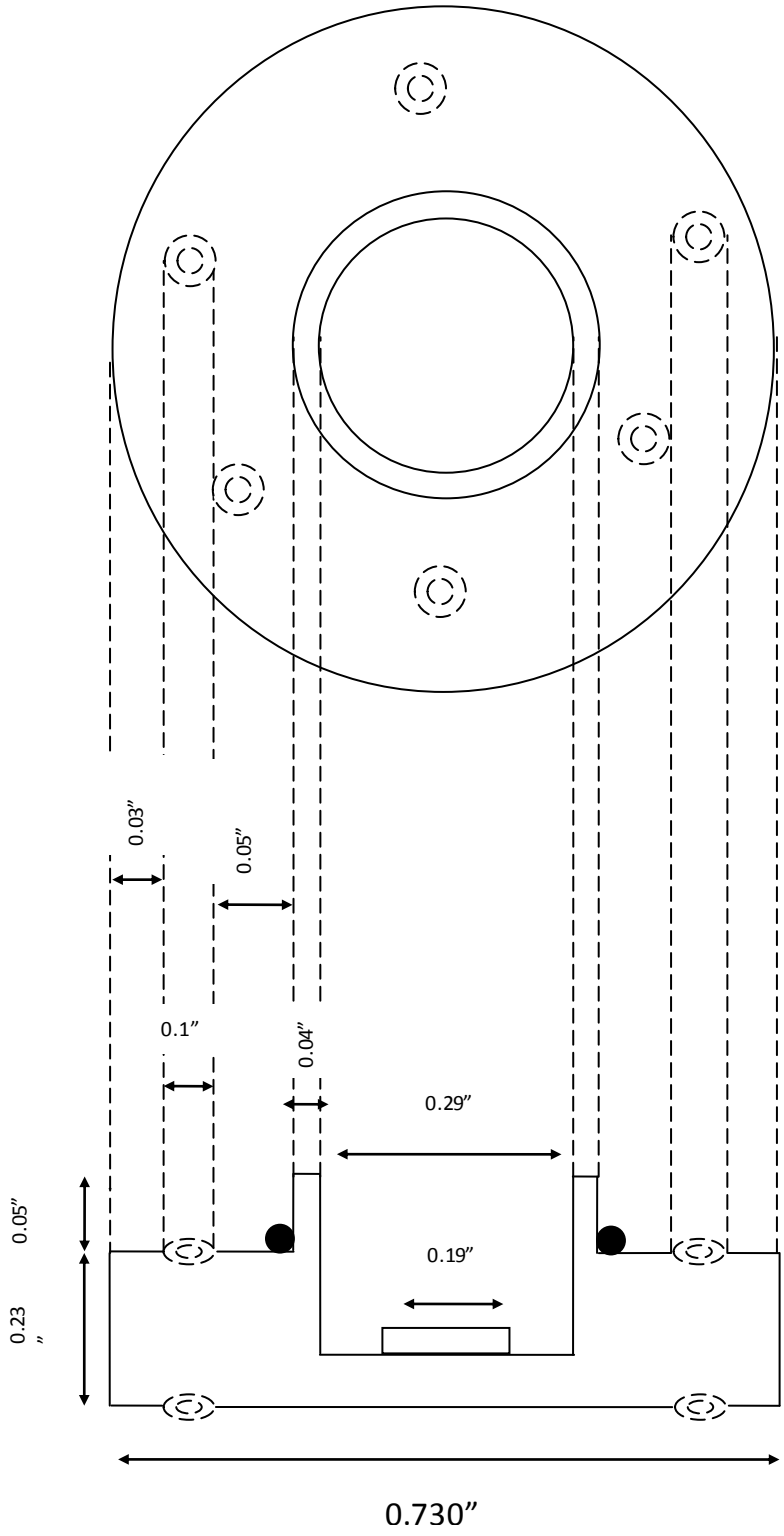

Figure 5.5: Lower part of dielectric cell

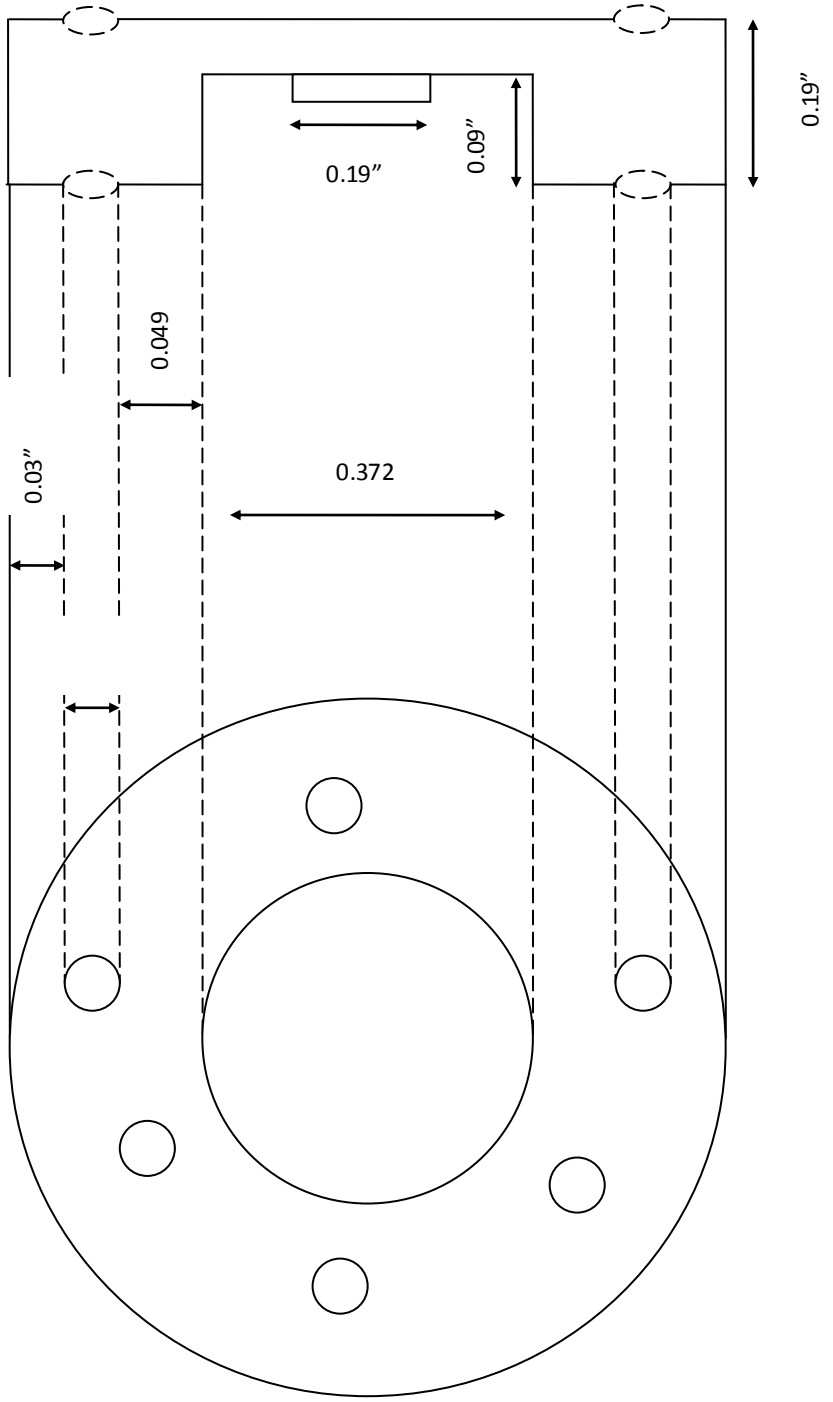

Figure 5.6: Upper part of dielectric cell

is electrically isolated from the rest of the cell by insulating black epoxy (Stycast 2850). An indium O-ring, which maintains its integrity at very low temperatures, is to seal the cell. Black epoxy was also used to make vacuum tight electrical feedthroughs to the electrodes. The spacing between the capacitor plates was adjusted to be ~ 1.5 mm when the cell is closed. The interior volume available for the ferrofluid of roughly ~ 30 mm^3.. This cell can be mounted in a Quantum Design PPMS, which provides temperature and magnetic field control. A schematic diagram of the cell is shown in Figs 5.5 and 5.6.

5.3.2 RESULTS AND DISCUSSIONS

We measured the dielectric response of dextran coated Fe_3O_4 ferrofluid in this dielectric cell over a temperature range from 10 K to 300 K. At lower temperature, we observe a frequency dependent peak in the dielectric loss as shown in Fig. 5.7 a.

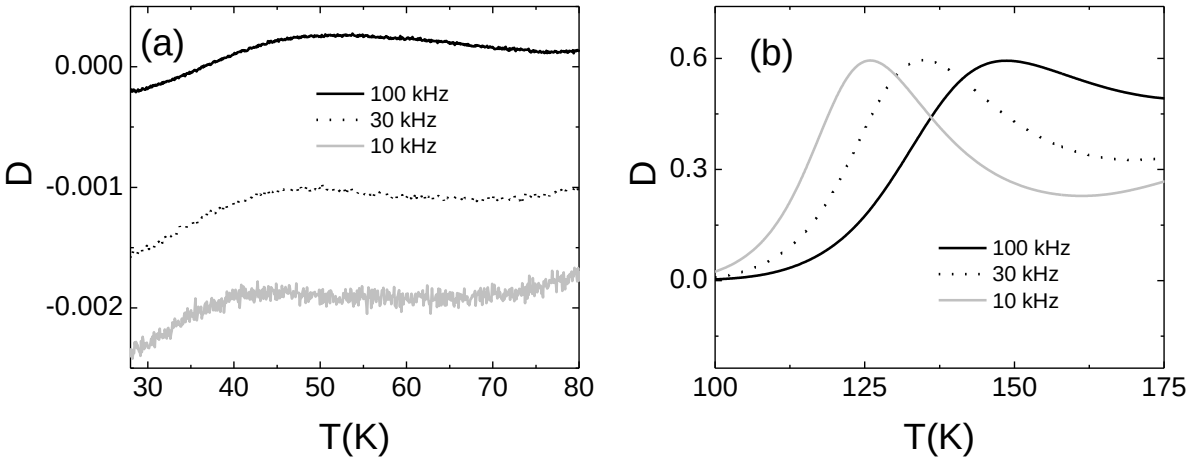

Figure 5.7: Dielectric loss as a function of temperature at different frequency in dextran-Fe_3O_4 ferrofluid (a) from 30 to 80 K and (b) from 100 to 175 K.

We fitted the temperature and frequency dependence of this peak to an Arrhenius equation, shown in Fig 5.7 a, and found an activation energy of 56 meV. We also observed a second frequency dependent peak near 125 K, shown in Fig 5.7 b. To confirm that the lower temperature peak is associated with some relaxation mechanism of the nanoparticles in solution, we also measured the AC susceptibility of this dextran Fe_3O_4 ferrofluid and conducted dielectric measurement on a pellet pressed from the residue of the freeze-dried ferrofluid. Neither of these measurements showed any frequency dependent peak near 125 K, suggesting that this higher temperature peak may an extrinsic artifact associated with a resonance

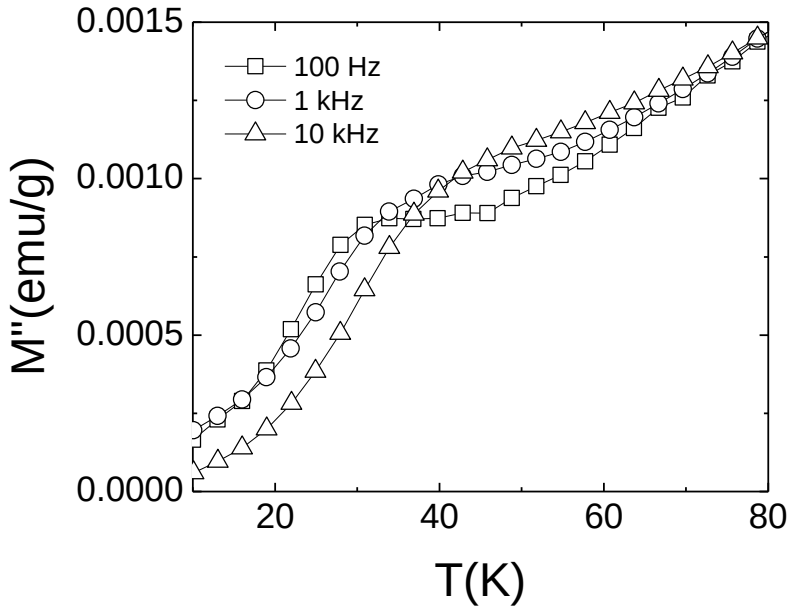

Figure 5.8: AC loss as a function of temperature at different frequency in dextran-Fe_3O_4 ferrofluid.

in the dielectric probe. However, these measurements confirm that the peaks observed at lower temperatures in the dielectric measurement, near 40 K, can be associated with magnetic relaxation of nanoparticles, as seen Fig. 5.8.

Furthermore, the fact that a sharp peak in the dielectric relaxation can be seen in the solid sample at the same temperature, as shown in Fig. 5.9, implies that this anomaly is a single-particle effect, and does not arise from any property of the nanoparticles in solution. We estimate the activation energy for the magnetic relaxation by fitting an Arrhenius equation to the frequency dependent peaks observed in AC susceptibility measurement of dextran-Fe_3O_4 ferrofluid. This yielded a value of 51 meV, which is consistent with the activation energy we obtained from dielectric measurement. This confirms that the same underlying mechanism is responsible for both features. The presence of coincident anomalies in both dielectric and magnetic measurements also confirms the presence of magneto-dielectric coupling in these iron oxide nanoparticles.

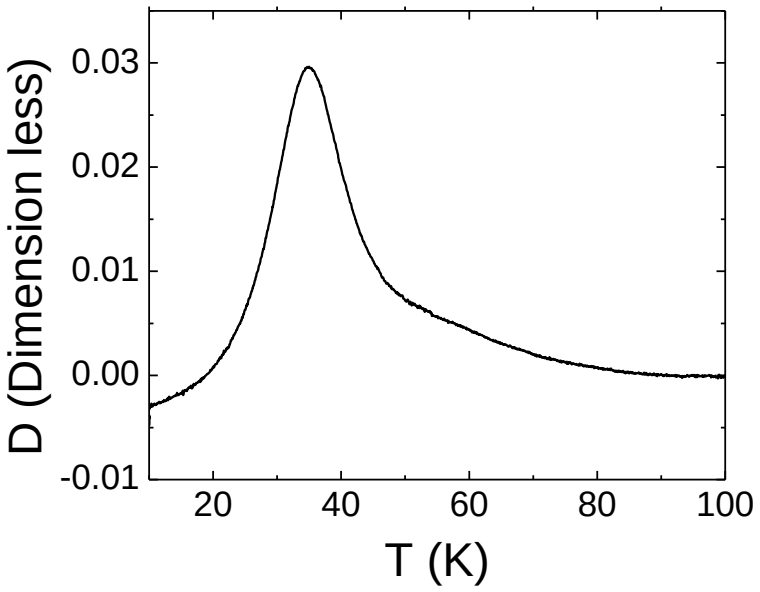

Figure 5.9: Dielectric loss as a function of temperature in dextran-Fe_3O_4 pellet.

In order to investigate the effects of chain formation on the dielectric response of the ferrofluid, we also measured the dielectric response by sweeping the frequency at different temperatures and magnetic field We plot the dielectric loss as a function of frequency normalized to the maximum value for these different measurements in Fig 5.10, where (0T, 0T) represents the sample was cooled at 0T and the measurement was also done at 0 T and (2T, 0T) represents the sample was cooled at 2 T and the measurement was done at 0 T. The reason for cooling the sample at applied field and zero filed was nanoparticles will form more chain like structure in the presence of applied magnetic field and will show different dielectric behavior than that of zero field cooled. Data in Fig 5.10 are generally analyzed in terms of the Casimir-du Pré relation with single relaxation time [166]. Since the relaxation curves at different temperature and magnetic fields coincide, as shown in Fig 5.10, the characteristic relaxation behaviour is identical. In particular, this analysis suggests that the formation of nanoparticles chains has no significant effect on the relaxation. We also investigated the dielectric response of the ferrofluid at the melting transition at fields of 0 T, 2 T and 5 T to study the effects of chain formation. These results are plotted in Fig 5.11 a, with Fig 5.11 b showing the difference between the high field and zero field data. Again, all the measurements were done at 0 T whereas sample was cooled at 0 T, 2 T, and 5 T as indicated in the legend of Fig 5.11 to investigate chain formation in ferrofluid. The sharp increase in dielectric loss on melting is associated with a dramatic increase in conductivity in

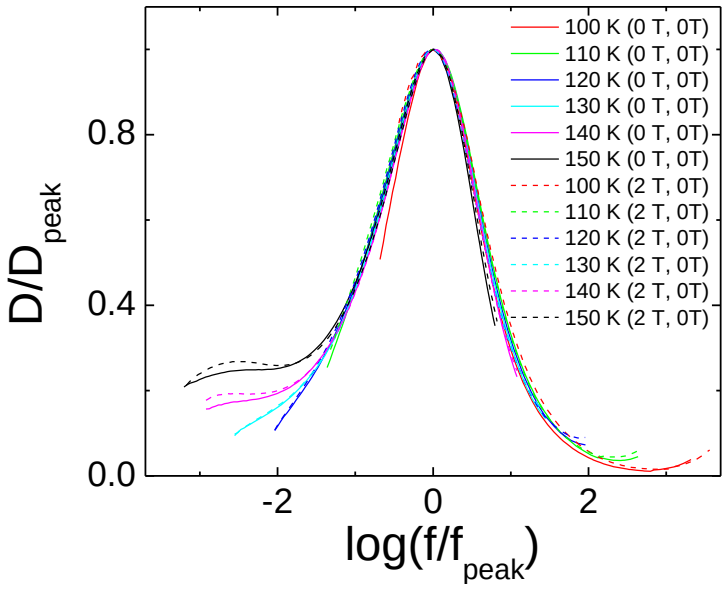

Figure 5.10: Dielectric loss as a function logarithm of frequency scaled to their maximum value at different temperature.

the liquid phase since the ferrofluid is only a good dielectric in the frozen state when electrical conductivity is suppressed. However, we didn't see any noticeable signature of chain formation from these data.

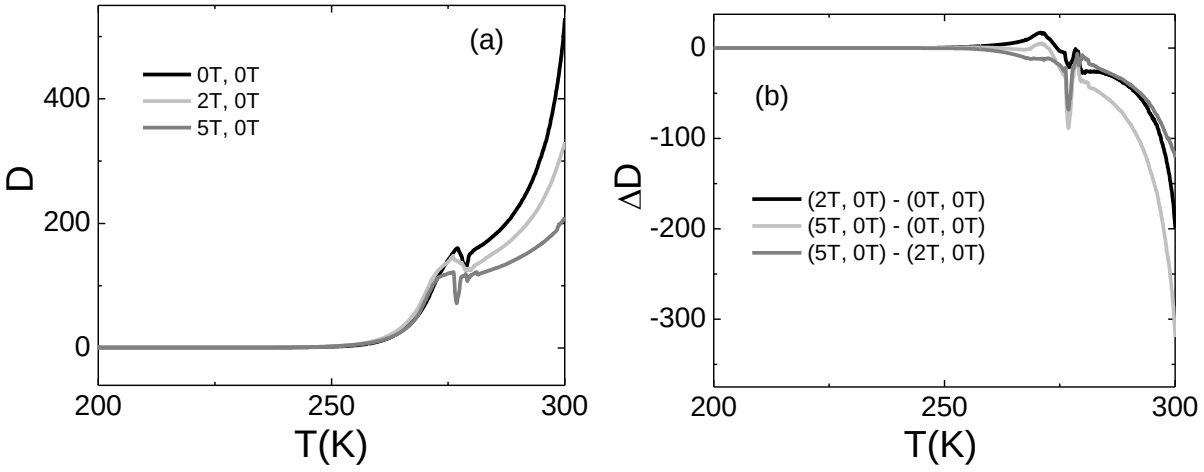

Figure 5.11: (a) Dielectric loss as a function of temperature at 0 T, 2 T and 5 T. (b) Difference in dielectric loss at 0 T, 2 T and 5 T as a function of temperature.

Measurements of the electrical properties of the ferrofluid on sweeping temperature can also yield information about the freezing and melting dynamics in this system. We measured the zero-field impedance as a function of temperature while warming and cooling through the phase transition at several different frequencies. The plots are shown in Fig 5.12. It shows that area of the loop at lower

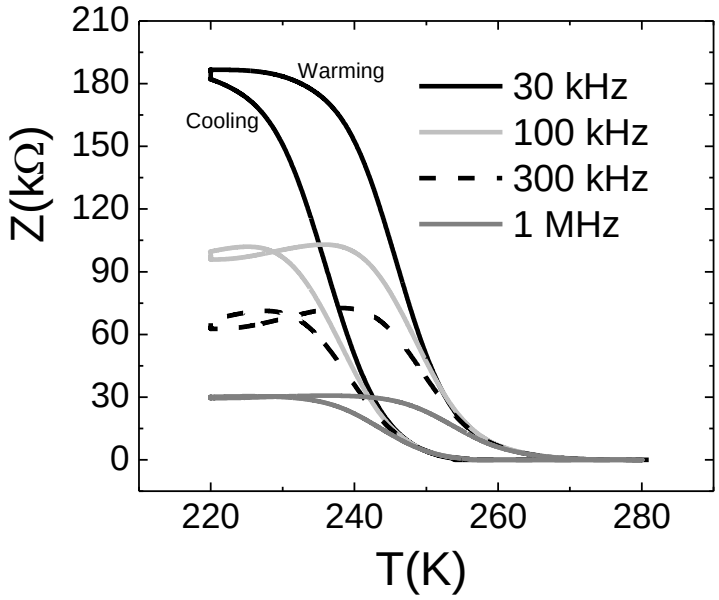

Figure 5.12: Impedance as a function of temperature while cooling and warming ferrofluid.

frequency is higher indicating more dielectric loss at lower frequency as compared higher one.

5.3.3 CONCLUSIONS

In summary, we designed a vacuum tight dielectric cell to do temperature dependent dielectric measurements on ferrofluids. Dielectric measurements at lower temperature showed relaxation peaks near 40 K consistent with AC

susceptibility measurement, which indicates the presence of magneto-dielectric coupling in this system. We also did zero field cooled and field cooled dielectric measurement to investigate chain formation in ferrofluid. However, we couldn't see any signature of chain formation from dielectric measurement. Frequency dependent study at different temperature implies iron oxide nanoparticles are monodispersed with single relaxation time. We also observed frequency dependent dielectric loss from the temperature sweep dielectric measurement at melting transition of ferrofluid.

5.4 SUMMARY

We investigated suppression of low temperature magnetic states in Mn_3O_4 nanoparticles. Only Yafet-Kittel phase transition at 42 K has been observed in Mn_3O_4 nanoparticles as compared to three different transition observed at 42 K, 40 K, and 34 K in bulk Mn_3O_4. Finite size effect and disordered surface spins might have suppressed low temperature magnetic states in Mn_3O_4 nanoparticles. We also studied the magnetic and dielectric properties of ferrofluid. We observed both dielectric and magnetic loss peak around 40 K in ferrofluid indicating same mechanism responsible for the feature, which also indicates magnetodielectric coupling in ferrofluid. We also did zero field and field cooled dielectric measurement in ferrofluid to investigate any signature of chain formation in ferrofluid but could see any noticeable feature regarding chain formation from these measurement. Zero

field impedance measurement on ferrofluid around melting transition shows higher loss at lower frequency.

Chapter 6

MAGNETIC CHARACTERIZATION OF NiMH BATTERY

6.1 INTRODUCTION

The transition from hydrocarbon based energy will require significant advances in energy storage. While there are a number of different technologies on the horizon, nickel metal hydride (NiMH) rechargeable represent a widely used and well established energy storage system. These batteries include a hydrogen-absorbing alloy as the negative electrode and nickel oxyhydroxide (NiOOH) as the positive electrode. These batteries are built on the fact that some metallic alloys form hydrides by absorbing a volume of hydrogen a factor of one thousand larger than their own [167]. This produces very high energy storage densities. In addition, these batteries can be cycled (charged and discharged) hundreds of times making them a viable long-term solution for energy storage. The charging and discharging scheme of these batteries is as follows:

$$\text{Alloy} + H_2O + e^- \rightleftharpoons \text{Alloy(H)} + OH^- \quad \ldots\ldots\ldots\ldots\ldots\ldots\ldots\ldots\ldots\ldots \quad (6.1)$$

While charging (the forward reaction in equation 6.1) with an electric potential applied, the water in the electrolyte decomposes and gives hydrogen ions, which in turn are absorbed by the alloy at the negative electrode. While discharging (the

reverse reaction in equation 6.1), the hydrogen desorbs from the alloy and combines with hydroxyl ions to form water. This process also contribute an electron to the circuit. The properties of these batteries can be improved by judicious selection of the electrode materials.. Some commonly used alloys are AB_2, AB_5 and A_2B_7. AB_2 alloys contain metals like titanium (Ti), zirconium (Zr) or hafnium (Hf) at the A site and transition metals like manganese (Mn), nickel (Ni) or chromium (Cr) at B sites. The AB_5 alloys contain hydride forming rare earth metal like lanthanum (La), Cerium (Cr) or Neodymium (Nd) at the A site and non hydride forming metals like Ni at the B site. A_2B_7 is typically based on the La-Mg-Ni system alloy with La and Mg at A site and Ni at B site.

Although NiMH batteries have a long track record, there remain considerable opportunities to improve their performance. It is crucial to understand the role of each element in the electrode through careful study of these alloys, which will give insight into how to improve their properties. It has been reported that metallic nickel nanoclusters embedded in the surface oxide of these alloys play an important role catalyzing the electrochemical reaction in Ni-MH batteries. These Ni based clusters affect the high-rate dischargeability (HRD) of the electrodes, and increase corrosion and passivation resistance [168,169]. Magnetic characterization can be used to help parameterize the surface catalytic activity of alloys since magnetic measurements give insight into the nanoscale structure of metallic clusters in the electrodes. In addition, the paramagnetic component of the magnetic susceptibility can be used to find the concentration of electrons in some alloys [170]. The size of

the nanoclusters can be obtained by fitting the room temperature magnetization curves using Langevin function [171]:

$$M(H) - \chi_B H = M_s \left\{ \coth\left(\frac{\mu H}{kT}\right) - \frac{kT}{\mu H} \right\} \quad \text{.....(6.2)}$$

where χ_B is the intrinsic paramagnetic susceptibility of the alloy, which is estimated by the value of the high field magnetization, M_S is the saturation magnetization of the ferromagnetic metallic Ni or Ni-alloy nanoparticles, μ is the net magnetic moment of each metallic cluster (assuming all the individual Ni spins are locked together ferromagnetically), k is the Boltzmann constant, and T is the absolute temperature. The mass fraction of metallic nickel was calculated from the ratio of the measured M_S and the known saturation magnetization of pure nickel metal (58.6 emu/g) while the size of the metallic nickel clusters was computed using μ together with the known moment per metallic Ni atom (0.6 μ_B/Ni). Within this framework, we calculated the size of Ni metal clusters and the fraction of Ni in different sample alloys having applications in NiMH batteries as described below. In addition, we have also investigated exchange bias effects on these system under the assumption that the Ni may have oxidized to form Ni-NiO (ferromagnetic-antiferromagnetic) nanocomposites.

6.2 COBALT SUBSTITUTED AB_2 ALLOYS

Cobalt substitution in Ni AB2 alloys has been investigated extensively to improve hydrogen storage and battery applications. Shaltiel et al. [172] found cobalt

content decreased the heat formation. Honda et al. [173] found the substitution of Co for Mn decreased the hydrogen storage capacity whereas Song et al. [174] has reported increase in capacity by partially replacing Ni with Co. The cycle durability has also increased by substituting Co as reported by Chen et al. Same group also mentioned the increase in heat formation (ΔH) with the increase in Co content. Similarly, Ji et al. [175] has found that cobalt content has increased cycle stability and self-discharge. We have done the magnetic studies on the different wt % cobalt substituted at the expense of Ni and correlated the wt. % of cobalt content as a function Ni cluster size with performance of battery investigated by other studies on the same samples.

Co substituted alloys were obtained from Ovonic Battery Company, Rochester Hills, Michigan. They provided six samples: CA01, CA02, CA03, CA04, CA05, and CA06. CA01 contains no cobalt, with the Co fraction having a sample-to-sample increase of 0.5 wt % up to sample CA06 with 2.5 wt% of cobalt. The amount of other constituents including cobalt on these alloys is given in the table 6.1, together with the Ni fraction and Ni cluster size estimated from the magnetic measurements. Since the atomic radii and electronegativity of Co and Ni are the same, Co substitution occurs at the expense of Ni and the overall radii and electronegativity of the alloys does not change. The magnetic susceptibility of metallic nickel clusters embedded in the surface layer of the electrodes is several orders of magnitude larger than from

Alloy	Ti	Zr	V	Ni	Cr	Mn	Co	Sn	Metallic Ni (%)	Ni cluster size (nm)
CA01	12	21.5	10	38.1	4.5	13.6	0	0.3	0.038	10.2
CA02	12	21.5	10	37.6	4.5	13.6	0.5	0.3	0.034	11.5
CA03	12	21.5	10	37.1	4.5	13.6	1	0.3	0.041	9.7
CA04	12	21.5	10	36.6	4.5	13.6	1.5	0.3	0.042	9
CA05	12	21.5	10	36.1	4.5	13.6	2	0.3	0.051	10
CA06	12	21.5	10	35.6	4.5	13.6	2.5	0.3	0.046	10

Table 6.1: Amount of constituents in the arc-melt prepared cobalt doped alloys.

nickel in the alloy due to the availability of unpaired electrons [171], so the amount of metallic nickel in this surface can be estimated from magnetization measurements. These non-destructive magnetic measurements can be done with a minimum of sample preparation, and measure the average properties over relatively large volumes, offering considerable advantages over other methods of probing the Ni nanoparticles concentrations, including TEM. Room temperature magnetization curves for each of these samples are plotted in Fig. 1. These curves can be fit to the Langevin function given by equation 6.2.

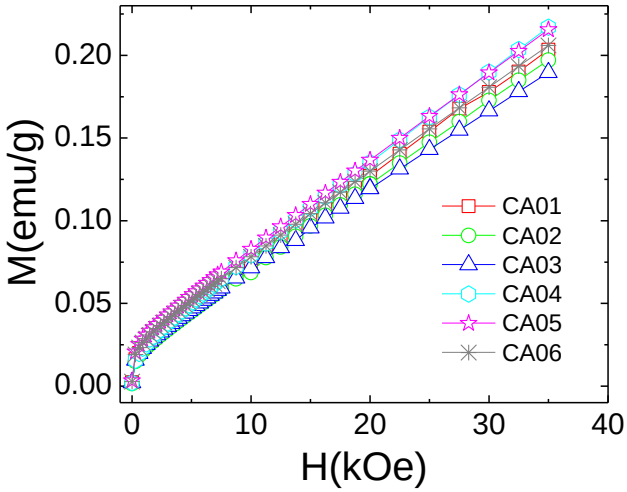

Figure 6.1: Room temperature magnetization curves for alloys CA01–CA06.

The Langevin fit depends on the saturation magnetization and net magnetic moment of the Ni clusters, from which we calculated fraction of metallic Ni and size

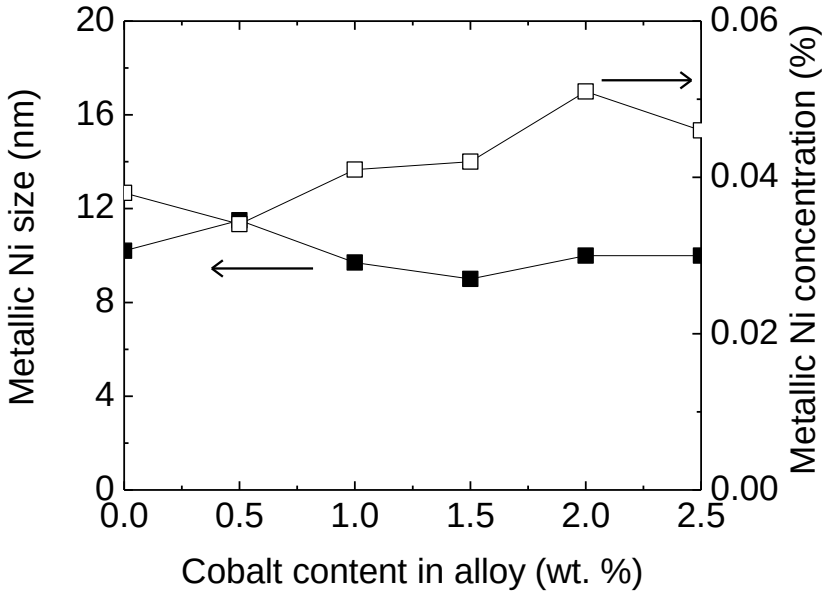

Figure 6.2: Average size and the concentration of metallic nickel cluster as a function of atomic percentage of Co in alloy.

of the Ni cluster respectively. These values are given in table 1 and plotted as a function of cobalt content in Fig 6.2. These investigations established that the content of metallic nickel increases while the cluster size decrease as Co is substituted into the alloy. Studies of hydrogen gas storage properties on these samples show that substitution of Co from 1 to 1.5 wt. % has increased the stability of hydride and hydrogen storage capability implying the importance of cobalt doping in higher charge storage [176]. 1.5 % cobalt doping has also lowest metallic Ni inclusions in the surface oxide.

6.3 ALUMINIUM SUBSTITUTED AB_2 ALLOYS

Relatively large size and less number of valence electron in Aluminium makes it an interesting element to study the substitution effect on NiMH battery. Inspite of its importance, there are limited number of studies about the Aluminium substitution in NiMH battery. Gamo and Moriwaki [177] have reported the reduction in flammability after substituting Aluminium at the expense of Zirconium (Zr). Wakao et. al. [178] found the durability of electrochemical cycling by the substitution of Aluminium. Yamamura et al. [179] found the voltage stand at high temperature has imporved after the substitution of Aluminium in AB2 alloy. We did magnetic measurements on different wt % Al substituted in AB2 alloy and have correlated the content of Al with size of Ni cluster to the battery performance obtained by other studies on the same samples.

Aluminium substituted alloys were also obtained from Ovonic Battery Company, Rochester Hills, Michigan, labeled as: CA01, CA07, CA08, CA09, CA10, and CA11. CA01 contains no aluminium and the Al fraction increase by 0.2 wt % for each sample to CA11 with 1 wt% of aluminium. The composition of these alloys, including information on the Ni content extracted from magnetic measurements, is given in the table 6.2.

Alloy	Ti	Zr	V	Ni	Cr	Mn	Al	Sn	Metallic Ni (%)	Ni cluster size (nm)
CA01	12	21.5	10	38.1	4.5	13.6	0	0.3	0.038	10.2
CA07	12	21.5	10	37.9	4.5	13.6	0.2	0.3	0.059	10.2
CA08	12	21.5	10	37.7	4.5	13.6	0.4	0.3	0.046	9.5
CA09	12	21.5	10	37.5	4.5	13.6	0.6	0.3	0.051	10.3
CA10	12	21.5	10	37.3	4.5	13.6	0.8	0.3	0.057	10.1
CA11	12	21.5	10	37.1	4.5	13.6	1	0.3	0.061	10.1

Table 6.2: Amount of constituents in the arc-melt prepared aluminium doped alloys.

As with the measurements on Co substituted alloys, magnetic measurements can be used to quantify the amount of metallic nickel on the surface. Room temperature magnetization curves measured as a function of applied magnetic field for these

samples are plotted in Fig. 6.3. These curves are fit to equation 6.2 to determine the saturation magnetization and magnetic moment of each nanocluster, which were then used to calculate the percentage of metallic Ni and size of Ni cluster. Concentration of metallic Ni and size of Ni cluster for each of the alloy are given in table 2 and plotted in Fig 6.4. The amount of metallic nickel present shows a sudden

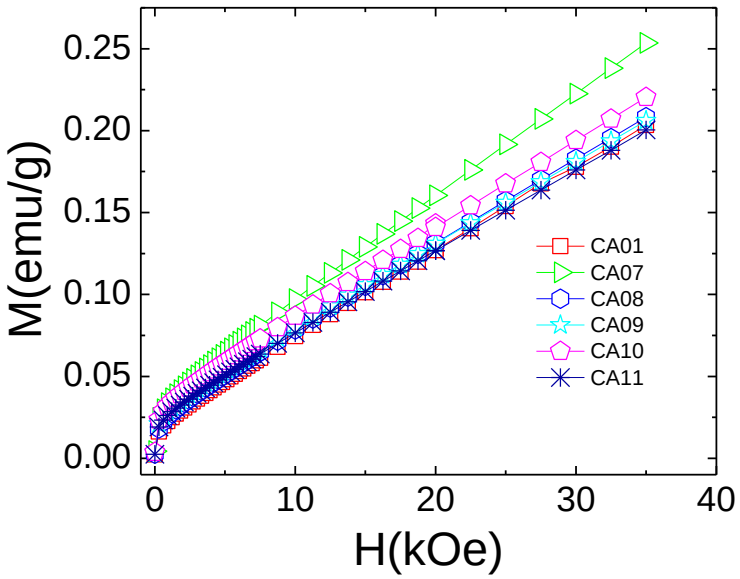

Figure 6.3: Room temperature magnetization curves for alloys CA01 and CA07–CA11.

jump as Al is added and then increases steadily with Al fraction, while the average size of the nickel clusters remains constant at roughly 10 nm. Incorporating Al into the alloys has increased the number of surface metallic nickel clusters, which contributes to a high HRD, but does not change the size of Ni clusters. 0.4 % Aluminium co-substituted with 1.5 % cobalt improves charge retention, high rate dischargeability, cycle life, specific power, and low temperature performance of

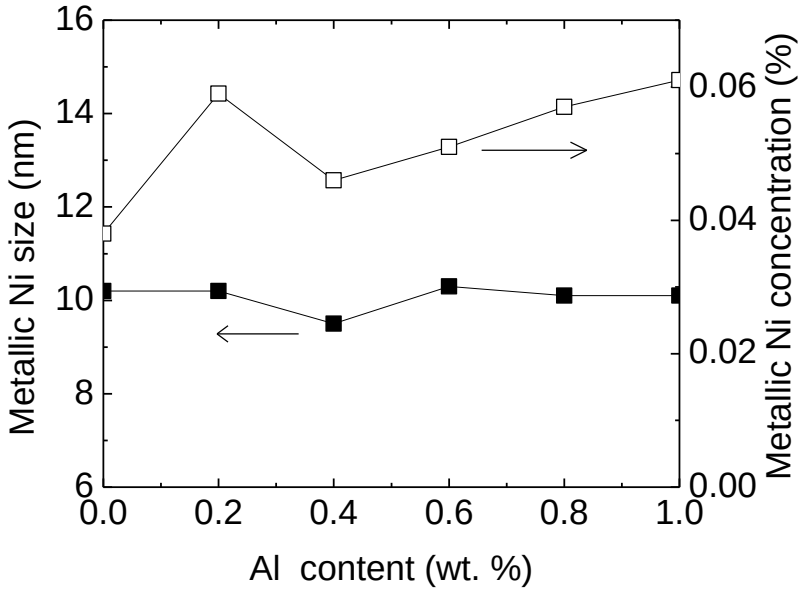

Figure 6.4: Average size and the concentration of metallic nickel cluster as a function of atomic percentage of Ni in alloy.

alloy. So, the combination of 1.5 % cobalt and 0.4 % Aluminium is the best substitution in alloy to improve the quality of the NiMH battery.

6.4 COMPARISONS OF METALLIC CLUSTERS EMBEDDED IN THE SURFACE OF AB_2, AB_5, and A_2B_7 ALLOYS

AB2, AB5 and AB7 are the alloys used in NiMH battery. Careful comparison of structural and physical properties of these alloys is necessary to identify the differences between them and suggest the method to improve their properties. There are a number of open questions concerning the interplay of composition and catalytic activity, which is strongly affected by Ni nanoclusters, in alloys for NiMH

battery electrodes. In particular, there is considerable interest in exploring how chemical etching affects the Ni distribution. In order to measure the size of the Ni nanoclusters along with the total fraction of metallic Ni, we did magnetic

Alloy	Composition	Alloy system	Saturation magnetization (memu/g)	Normalized cluster size
A	$Ti_{12}Zr_{21.5}Ni_{36.2}V_{9.5}Cr_{4.5}Mn_{13.6}Sn_{0.3}Co_2Al_{0.4}$	AB_2	33	1
B	$La_{10.5}Ce_{4.3}Pr_{0.5}Nd_{1.4}Ni_{60.0}Co_{12.7}Mn_{5.9}Al_{4.7}$	AB_5	434	0.93
C	$La_{16.3}Mg_{7.0}Ni_{65.1}Co_{11.6}$	A_2B_7	369	1.06
D	$Nd_{18.8}Mg_{2.5}Ni_{65.1}Al_{13.6}$	A_2B_7	132	0.95

Table 6.3: Compositions and summary of Alloys A-D.

measurement on four alloys A, B, C and D described below, prepared with different etching time: 0 h, 0.5 h, 1h, 2 h, 3 h and 4 h of each. Etching was done at 100 ^{o}C in 30 % KOH at above mentioned time intervals to activate the surface of alloys. We obtained these samples from Ovonic Battery Company, Rochester Hills, Michigan. The nominal composition and structure are given in the table 3 for these samples.

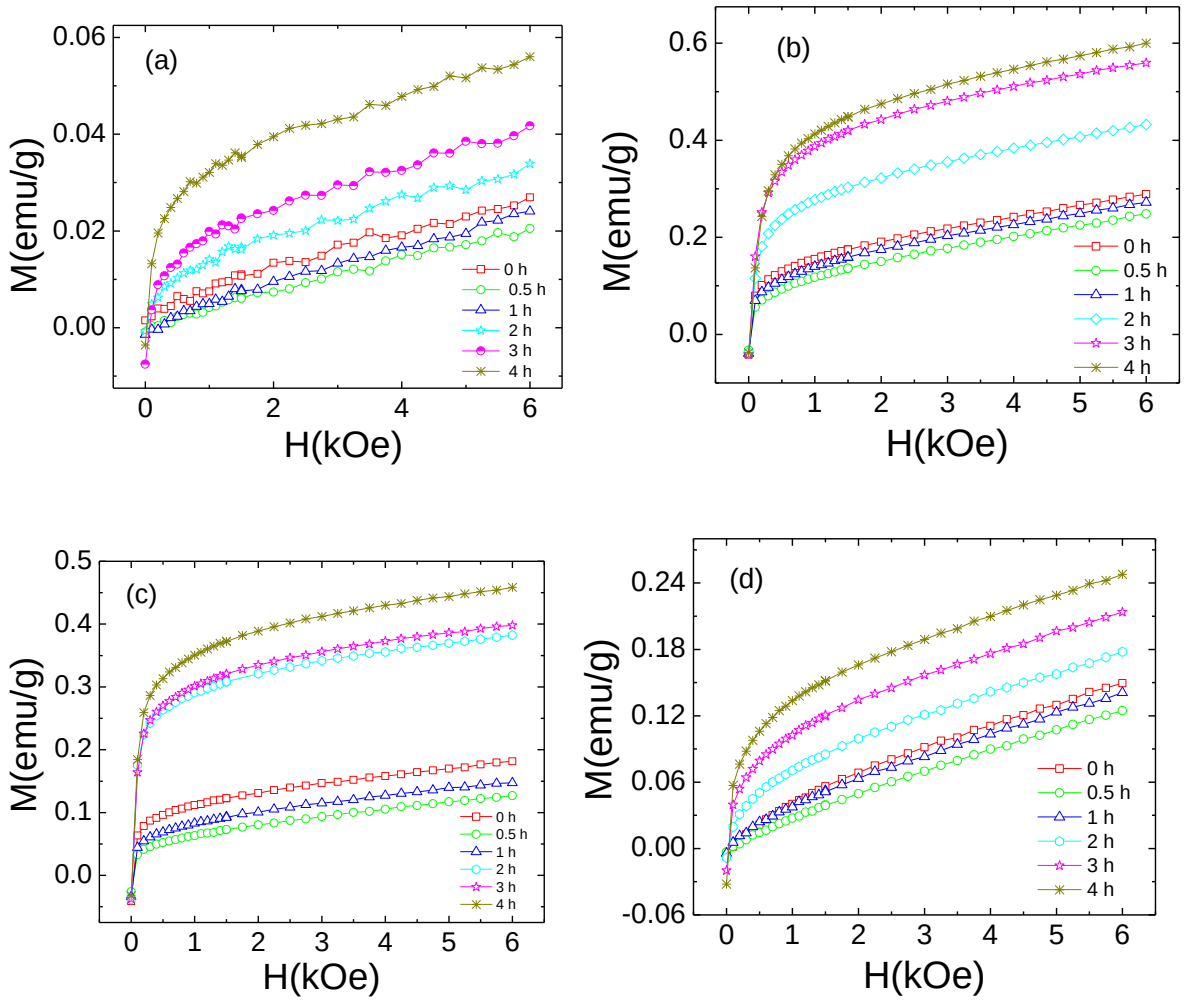

Figure 6.5: The magnetic susceptibility curves measured at room temperature for alloys A (a), B (b), C (c), and D (d).

The characteristics of the nanoscale metallic nickel clusters embedded in the surface oxide were studied by probing the magnetic susceptibility, The magnetization values associated with the ferromagnetic metallic nickel nanoclusters is a few orders of magnitude larger than that from the paramagnetic nickel atoms [171]. Room temperature magnetization curves were measured as a function of applied magnetic field for the etched powder sample. These curves are

plotted in Fig. 6.5 a–d for alloys A–D, respectively. The saturation magnetization and magnetic moment of each nanocluster were obtained by fitting equation 6.2 from which the percentage of metallic Ni and size of the Ni clusters were calculated. For easy comparison, values are normalized to cluster size of 4 h etched Alloy A. Both the M_S values and the normalized sizes of the Ni clusters in the 4 h samples are listed for each alloy in Table 3 and plotted in Fig. 6.6 a and b. The M_S and the average size of the metallic clusters both decrease with the first half-hour of etching for all four alloys. This suggests a dissolution of the native oxide formed during powder processing [180]. After this time, a new oxide layer having a higher porosity due to selective leaching is formed. The thickness of this oxide layer increases with

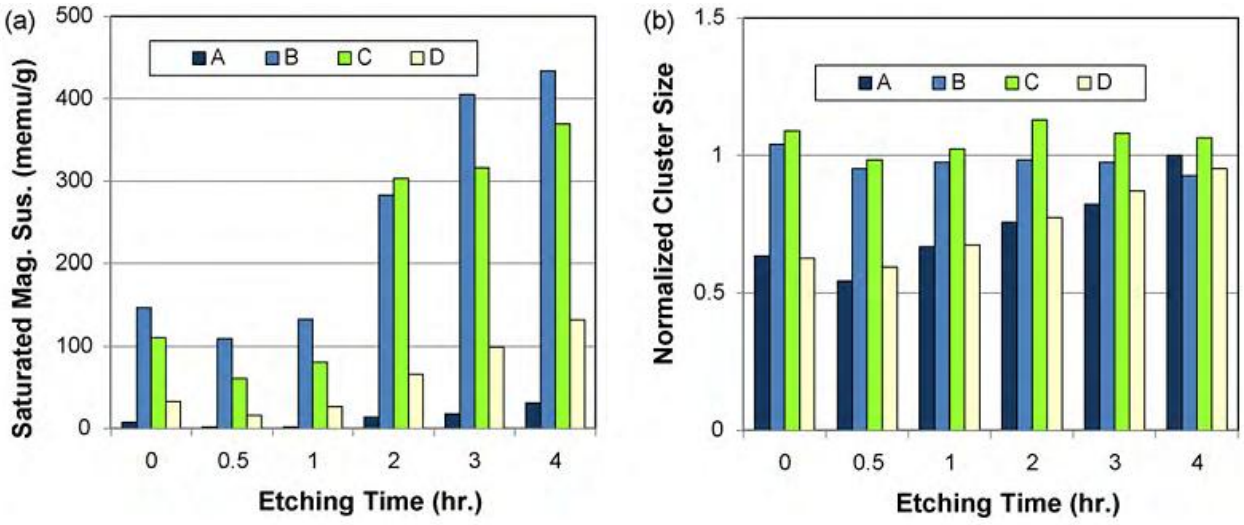

Figure 6.6: Evolution of the saturated magnetic susceptibility (a), and normalized cluster size (b) as functions of etching time for alloys A–D. Taken from *J. Alloys and Compd.*, **506**, 831 (2010).

the etching time until the accumulated hydrogen reduces any further oxidation of the bulk metal. After 4 h of etching, the magnitude of the saturation magnetization is largest for Alloy B, followed by the alloy sequence of C, D, and then A. This implies that the alloy having higher magnetization has high rate dischargeability associated with metallic nanoclusters but low total capacity which is just opposite in case of the sample with lowest magnetization.

6.5 SUMMARY

In order to parameterize the size and distribution of Ni nanoclusters in NiMH battery electrode materials, we measured the room temperature magnetization in cobalt doped and aluminium doped AB_2 alloys. In addition, we also determined the relative sizes of Ni clusters and saturation magnetization in three different alloys, namely, AB_2, AB_5, and A_2B_7. Sample with higher saturation magnetization has high rate dischargeability with low capacity and vice versa.

Chapter 7
SUMMARY

We investigated a number of different properties and biomedical applications of magnetic nanoparticles. We have focused primarily on biocompatible iron oxide nanoparticles, which can readily be prepared by a fast, simple, and efficient low temperature technique. Because of their small size, it is possible to fit millions of these nanoparticles inside each cell, which we confirmed using magnetic studies. The surfaces of these nanoparticle can be functionalized by attaching a variety of biologically active ligands, This offers the possibility of using these particles to carry biologically and therapeutically relevant molecules inside cells. By investigating the physical and biological properties of a variety of these functionalized iron oxide particles, we have clarified a number of important issues concerning the biomedical applications of magnetic nanoparticles.

We used a wide range of biocompatible surfactants to coat these nanoparticles including fatty acids, dextran, and hyaluronic acid. We used different tools to characterize these nanoparticles, such as Transmission Electron Microscopy (TEM) to get the core size of nanoparticles, X-ray diffraction (XRD) to confirm the crystal structure, Dynamic Light Scattering (DLS) and Fluorescent Correlation Spectroscopy (FCS) to obtain the hydrodynamic size in solution, Thermogravimetry analysis (TGA) to establish the number of surfactant layers and amount of coating, Zeta potential studies to find the surface charge, and magnetization measurements

to establish the magnetic properties of the nanoparticles. These nanoparticles synthesis techniques and studies on their fundamental properties provide a strong platform for continuing investigations on biomedical applications of magnetic nanoparticles. Some of the specific studies included in this work are investigations on magnetic hyperthermia, targeted drug delivery and radiation therapy.

We designed and built a magnetic hyperthermia apparatus to investigate the magnetic heating of these nanocomposites produced by an alternating magnetic field. This remote heating provides a non-invasive technique for controlling the nanoparticles properties. In one specific investigation, magnetic heating was used to trigger the release of an anticancer drug mitoxantrone from a thermosensitive polymer, poly N-isopropylacryl amide (PNIPAM). We heated PNIPAM-Fe_3O_4 above the lower critical solution temperature (LCST) of the nanocompostie, 38 ^oC, by applying an alternating magnetic field of 130 Oe for only four minutes. The drug release rate from PNIPAM-Fe_3O_4 was 1 % per minute, which is about 8 times larger as compared to the bare PNIPAM heated using a water bath as a control. Continuing with the theme of building targeted drug delivery applications around magnetic nanoparticles, we also studied the dynamics of drug release from nanoparticles coated by different chain length dextran. An anticancer drug camptothecin was loaded into 15-20 kDa and 60-90 kDa dextran coated sample and the loading effieciency was found to be 100 % for both samples. Time dependent drug release measurements in phosphate buffer saline (PBS) showed 12 % and 8 % drug release from 60-90 kDa and 15-20 kDa dextran coated sample respectively in

72 h implying that higher molecular mass coated iron oxide release more drug as compared to the lower molecular mass surfactant. As a more discriminating test of utilizing magnetic nanoparticles for targeted delivery, we labeled these iron oxide nanoparticles with tat peptide to target the cell nucleus. Our preliminary result shows that these particles have accumulated inside the cell nucleus, with a net nanoparticles concentration of approximately 6×10^6 nanoparticles per cell.

Iron oxide nanoparticles have been used for many biomedical application including MRI, magnetic hyperthermia, targeted drug delivery, magnetofection, and stem cell tracking but, to best of our knowledge, iron oxide nanoparticles have never been used for the localized radiation therapy. This novel idea of localizing iron oxide nanoparticles at the nucleus of the cell to produce higher linear energy transfer (LET) low enery X-ray and Auger electron to damage cell DNA offers an exciting opportunity to investigate novel applications of magnetic nanoparticles in radiation therapy. In addition, since iron oxide acts a contrast agent in MRI, combining iron oxide based radiation therapy with MRI brings one more promising possibility in the emerging area of image guided radiation therapy for cancer treatment.

In order to further investigate the properties of magnetic nanoparticles in solution, we also investigated the dielectric behavior of iron oxide based ferrofluid. This involved designing and building a vacuum tight dielectric cell capable of holding to low temperatures. Dielectric studies on iron oxide based ferrofluid showed relaxation peak at lower temperature of around 40 K, which was also accompanied by magnetic measurement, implying significant magnetodielectric

coupling in this system. We have also done field cooled and zero field cooled dielectric studies on the ferrofluid to investigate the chain formation but did not see any noticeable feature that could be associated with chain like structures in these measurements. Beyond studies of iron oxide nanoparticles, we also explored the properties of other types of magnetic nanoparticles. We established that several low temperature magnetic transitions are suppressed in Mn_3O_4 nanoparticles, plausibly due to surface spins. This has important implications for designing nanoscale devices based on novel magnetic materials, as it suggests that the desirable magnetic characteristics may not persist in reduced geometries. We also investigated the magnetic response of different alloys used for NiMH battery electrodes to explore the size and distribution of Ni nanoparticles in these systems. These Ni nanoparticles play an important role in catalyzing the electrochemical reaction and powering the NiMH batteries, so it is important to develop non-destructive techniques for studying these particles. We also extended these studies to probe the exchange bias effect in this system to indirectly characterize the properties of a Ni-NiO (ferromagnetic-anitferromagnetic) nanocomposite formed by the oxidation of the Ni nanoparticles.

In summary, the physical properties of nanoscale magnet, such as size, biocompatibility, ease of functionalization and the ability to manipulate them using non-invasive external magnetic field, make them promising agents for biomedical applications. This thesis has investigated many physical properties of iron oxide nanoparticles along with many biomedical applications.

BIBLIOGRAPY

[1] R. H. Kodama, *J. Magn. Magn. Mater.*, **200,** 359 (1999).

[2] L. F. Gamarra, G. E. S. Brito, W. M. Pontuschka, E. Amaro, A. H. C. Parma and G. F. Goya, *J. Magn. Magn. Mater.* **289**, 439 (2005).

[3] K. Muller, J. N. Skepper, M. Posfai, R. Trivedi, S. Howarth, C. Corot, E. Lancelot, P. W. Thompson, A. P. Brown and J. H. Gillard, *Biomaterials,* **28**, 1629 (2007).

[4] A. Aharoni, Introduction to the Theory of Ferromagnetism, 2nd ed., Oxford, 2000.

[5] J. R. Hook and H.E. Hall, Solid State Physics, 2nd ed. , John Wiley and Sons, NY, 1991.

[6] D. Jiles, Introduction to Magnetism and Magnetic Materials , Chapman and Hall, NY, 1989.

[7] S. Blundell, Magnetism in Condensed Matter, Oxford, 2001.

[8] D. L. Leslie-Pelecky and Reuben D. Rieke, *Chem. Mater.*, **8** , 1770 (1996).

[9] C. Luna, M. D. P. Morales, C. J. Serna and M. Vazquez, *Nanotechnology*, **14,** 268 (2003).

[10] N. A. D. Burke, H. D. H. Stöver, F. P. Dawson, J. D. Lavers, P. K. Jain, and H. Oka, *IEEE Trans. Magn.*, **37**, 2660 (2001).

[11] P. Gangopadhyay, S. Gallet, E. Franz, A. Persoons and T. Verbiest, *IEEE Trans. Magn.*, **41**, 4194 (2005).

[12] . S. Nishijima , F. Mishima, T. Terada, S. Takeda, *Physica C,* **463–465**, 1311 (2007).

[13] E. P. Furlani and K. C. Ng, *Phys. Rev. E*, **73** , 061919 (2006).

[14] S. K. Venkatasubramaniam, B. Han, B. E. Hammer, T. W Shield and J. C. Bischof, *Nanotechnology*, **16,** 1221 (2005).

[15] Q. A. Pankhurst, J. Connolly, S. K. Jones and J. Dobson.

[16] S. Maenosono and S. Saita, *IEEE Trans. Magn.*, **42**, 1638 (2006).

[17] S. Bae, S. Lee, Y. Takemura, E. Yamashita, J. Kunisaki, S. Zurn and C. S. Kim, *IEEE Trans. Magn*, **42**, 3566 (2006).

[18] I. Baker, Q. Zeng, W. Li and C. R. Sullivan, *J. Appl. Phys.*, **99**, 08H106 (2006).

[19] M. Kallumadil, M. Tada, T. Nakagawa, M. Abe, P. Southern, Q. A. Pankhurst, *J. Magn. Magn. Mater.*, **321**, 1509 (2009).

[20] A. Bjørnerud and L. Johansson, *NMR Biomed.*, **17**, 465 (2004).

[21] K. N. Joshipura, S. Gangopadhyay, C. G. Limbachiya and M. Vinodkumar, *J. Phys.: Conf. Ser.,* **80**, 012008 (2007).

[22] D. Leaver and C. M. Washington, Principal and Practice of Radiation Therapy, Second Edition (2004).

[23] R. Massart, *IEEE Trans. Magn.*, **17**, 1247 (1981).

[24] I Martinez-Mera, M. E. Espinosa-Pesqueira, R. Perez-Hernandez and J. Arenas-Alatorre, *Mater. Lett.*, **61**, 4447 (2007).

[25] Li, B. Tan, M. Allix, A. I. Cooper and M. J. Rosseinsky, *Small*, **4**, 231 (2008).

[26] Y. Lee, J. Lee, C. J. Bae, J. G. Park, H. J. Noh, J. H. Park and T. Hyeon, *Adv. Funct. Mater.* **15**, 503 (2005).

[27] A. H. Latham and M. E. Williams, *Acc. Chem. Res.* **41**, 411 (2008).

[28] P. Tartaj, T. Gonzalez-Carreño, A. F. Rebolledo, O. Bomatí-Miguel and C. J. Serna, *J. Colloid Interface Sci.*, **309**, 68 (2007).

[29] A. G. Roca, R. Costo, A. F. Rebolledo, S. Veintemillas-Verdaguer, P. Tartaj, T González- Carreño, M. P. Morales and C. J. Serna, *J. Phys. D: Appl. Phys.* **42**, 224002 (2009).

[30] H. Iida, K. Takayanagi, T. Nakanishi and T. Osaka, *J. Colloid Interface Sci.*, **314**, 274 (2007).

[31]] M. Andres-Vergés, R. Costo, A. G. Roca, J. F. Marco, G. F. Goya, C. J. Serna and M. P. Morales, *J. Phys. D: Appl. Phys.* **41**, 134003 (2008).

[32] T. Sugimoto and E. Matijevic, *J. Colloid Interface Sci.* **74**, 227 (1980).

[33] R. Y. Hong, Z. Q. Rena, Y. P. Han, H. Z. Li, Y. Zheng, J. Ding., *Chem. Eng. Sci.*, **62**, 5912 (2007).

[34] S. H. Choi, K. H. Kim, W. K. Moon, H. C. Kim, J. H. Cha, J. H. Paik, and K. H. Chang, *J. Magn. Reson. Imaging*, **31**, 134 (2010).

[35] L. Josephson, C. H. Tung, A. Moore, R. Weissleder, *Bioconjugate Chem.*, **10**, 186 (1999).

[36] S. Palmacci and L. Josephson, United States Patent Number 5,262,176 (1993).

[37] P. Wunderbaldinger, L. Josephson and Ralph Weissleder, *Bioconjugate Chem.*, **13**, 264 (2002).

[38] Y. Lee, H. Lee, Y. B. Kim, J. Kim, T. Hyeon, H. W. Park, P. B. Messersmith, and T. G. Park, *Adv. Mater.*, **20**, 4154 (2008).

[39] Y. Guan and Y. Zhang, *Soft Matter*, **7**, 6375 (2011).

[40] J. Rubio-Retama, N. E. Zafeiropoulos, C. Serafinelli, R. Rojas-Reyna, B. Voit, E. L. Cabarcos, and M. Stamm, *Langmuir,* **23**, 10280 (2007).

[41] W. L. Bragg, *Proceedings of the Cambridge Philosophical Society*, **17**, 43 (1913).

[42] P. Scherrer, *Göttinger Nachrichten Gesell.*, **2**, 98 (1918).

[43] G. S. Rajan, K. A. Mauritz, S. L. Stromeyer, T. Kwee, P. Mani, J. L. Weston, D. E. Nikles, M. Shamsuzzoha, Journal of Polymer Science, **43**, 1475 (2005).

[44] L. Mu, P. H. Seow, S. N. Ang, S. S. Feng, *Colloid. Polym. Sci.* **58**, 283 (2004).

[45] B. J. Frisken, *Applied Optics*, **40**, 4087 (2001).

[46] W. B. Russel, D. A. Saville, W. R. Schowalter, Colloidal Dispersions, paperback ed., Cambridge University Press, Cambridge 1992, 525 pp.

[47] P. Schwille, U. Haupts, S. Maiti, and W. W. Webb, *Biophys. J.*, **77,** 2251 (1999).

[48] W. R. Browne and J. J. McGarvey, *Coord. Chem. Rev.*, **251**, 454 (2007).

[49] C. Rinaldi, Arlex Chaves , Shihab Elborai , Xiaowei (Tony) He , Markus Zahn, *Curr. Opin. Colloid In.*, **10**, 141 (2005)

[50] W. B. Russel, D. A. Saville, W. R. Schowalter, *Colloidal Dispersions*, paperback ed., Cambridge University Press, Cambridge 1992, 525 pp.

[51] S. Will and A. Leipertz, Progr. Colloid Polym. Sci., **104**, 110 (1997).

[52] P. Schwille, U. Haupts, S. Maiti, and W. W. Webb, *Biophys. J.,* **77,** 2251 (1999).

[53] A. P. Herrera, M. Rodríguez, M. Torres-Lugo and C. Rinaldi, J. Mater. Chem., **18**, 855 (2008).

[54] T. S. Chow, *Phys. Rev. E*, **48** , 1977 (1993).

[55] P. Degen, A. Shukla, U. Boetcher, and H. Rehage, *Colloid. Polym. Sci*., **286**, 159, (2008).

[56] O. Thompson Mefford, M. R. J. Carroll, M. L. Vadala, J. D. Goff, R. Mejia-Ariza, M. Saunders, R. C. Woodward, T. G. St. Pierre, R. M. Davis and J. S. Riffle, *Chem. Mater*. **20**, 2184 (2008).

[57] Y. Zhang, N. Kohler, and M. Zhang, *Biomaterials,* **23**, 1553 (2001)

[58] B. Yoza, M. Matsumto, T. Matsunaga, *J. Biotechnology*, **94**, 217 (2002)

[59] D.H. Chen, M.H. Liao, *J. Mol Catal. B: Enzym*., B16, 283 (2002)

[60] J. Chatterjee, Y. Haik, and C.J. Chen, *J. Magn. Mag. Mater*. **246**, 382 (2002)

[61] B.J. De Gans, C. Blom, J. Mellema, and A.P. Philipse, *J. Magn. Mag. Mater*., **201**, 11 (1999).

[62] H. Pardoe, W. Chua-Anusorn, T.G. St Pierre, and J. Dobson, *J. Magn. Magn. Mater.,* **225**, 41 (2001)

[63] C.E. Sjogren, C. Johansson, A. Novestad, P.C. Sontum, K. Briely_Saebo, A.K. Fahlvik, *Magn. Reso. Imaging*, **15**, 55 (1997)

[64] M. De Cuyper, M. Joniau, *Eur. Biophys. J*., **15**, 311 (1988).

[65] Y. Sahoo, H. Pizem, T. Fried, D. Golodnitsky, L. Burstein, C. N. Sukenik, G. Markovich, *Langmuir*, **17**, 7909 (2001)

[66] L. Fu, V. P. Dravid, D. L. Johnson, *Appl. Surf. Sci.*, **181**, 173 (2001).

[67] M. Mikhaylova, D. K. Kim, N. Bobrysheva, M. Osmolowsky, V. Semenov, T. Tskalakos, M. Muhammed, *Langmuir*, **20**, 2472 (2004).

[68] C. Caizer, *J. Phys. Condens. Matter* **15**, 765 (2003)

[69] E. Kneller, *Ferromagnetismus* (Berlin:Springer) 1962, p422

[70] L. Vekas, D. Bica, and O. Marinica, *Rom. Rep. Phys*. **58**, 257 (2006).

[71] Q. A. Pankhurst, N. K. T. Thanh, S. K. Jones and J. Dobson, *J. Phys. D: Appl. Phys.*, **42,** 224001 (2009).

[72] C. L. Dennis, A. J. Jackson, J. A. Borchers, R. Ivkov, A. R. Foreman, P. J. Hoopes, R. Strawbridge, Z. Pierce, E. Goerntiz, J. W. Lau and C. Gruettner, *J. Phys. D: Appl. Phys*. **41**, 134020 (2008).

[73] Y. K. Lee, S. B. Lee, Y. U. Kim, K. N. Kim, S. Y. Choi, K. H. Lee, I. B. Shim and C. S. Kim, *J. Mater. Sci.,* **38**, 4221 (2003).

[74] R. Hergt , R. Hiergeist, I. Hilger, W.A. Kaiser, Y. Lapatnikovc, S. Margel and U. Richter, *J. Magn. Magn. Mater*., **270**, 345 (2004).

[75] K. J. Miller, K. N. Collier, H. B. Soll-Morris, R. Swaminathan and M. E. McHenry, *J. Appl. Phys*., **105**, 07E714 (2009).

[76] T. Druzhinina, W. Weltjens, S. Hoeppener and U. S. Schubert, *Adv. Funct. Mater.,* **19**, 1287 (2009).

[77] M. Zeisberger, S. Dutz, R. Muller, R. Hergt, N. Matoussevitch and H. Bonnemann, *J. Magn. Magn. Mater.*, **311**, 224 (2007).

[78] G. Glöckl, R. Hergt, M. Zeisberger, S. Dutz, S. Nagel and W. Weitschies, *J. Phys. Condens. Matter*, **18**, S2935 (2006).

[79] K. Okawa, M. Sekine, M. Maeda, M. Tada, and M. Abe, N. Matsushita, K. Nishio and H. Handa, *J. Appl. Phys.*, **99**, 08H102 (2006).

[80] R. E. Rosensweig, *J. Magn. Magn. Mater.*, **252**, 370 (2002).

[81] M. S. Seehra, V. Singh, P. Dutta, S. Neeleshwar, Y. Y. Chen, C. L. Chen, S. W. Chou and C. C. Chen, *J. Phys. D: Appl. Phys.* **43**, 145002 (2010)

[82] L.-M. Lacroix, R. B. Malaki, J. Carrey, S. Lachaize, M. Respaud, G. F. Goya and B. Chaudret, *J. Appl. Phys.*, **105**, 023911 (2009)

[83] R. Hergt, S. Dutz and M. Zeisberger, Nanotechnology **21**, 015706 (2010)

[84] R. Mehvar, *J. Controlled Release*, **69**, 1 (2000).

[85] M. C. Bautista, O. Bomati-Miguel, M. D. P. Morales, C. J. Serna, S. Veintemillas-Verdaguer, *J. Magn. Magn. Mater.*, **293**, 20 (2005).

[86] L. Shen, P. E. Laibinis, and T. A. Hatton, *Langmuir*, **15**, 447 (1999).

[87] T. Kawaguchi and M. Hasegawa, J. *Mater. Sci.: Mater. Med.*, **11**, 31, (2000).

[88] A. K. Gupta and M. Gupta, *Biomaterials* **26**, 3995 (2005).

[89] OxyChem Caustic Soda Handbook, Occidental Chemical Corporation 2009.

[90] S. Will and A. Leipertz, *Progr. Colloid Polym. Sci*., **104**, 110 (1997).

[91] T. S. Chow, *Phys. Rev. E*, **48** , 1977 (1993).

[92] A. D. Yancy, A. R. Olzinski, T. C. C. Hu, S. C. Lenhard, K. Aravindhan, S. M. Gruver, P. M. Jacobs, R. N. Willette, B. M. Jucker, *J. Mag. Res. Imaging*, **21**, 432 (2005).

[93] S. Zhang, J. Li., G. Lykotrafitis, G. Bao, S. Suresh, *Adv. Mater*., **21**, 419 (2009).

[94] A. R. Muxworthy and E. McClelland, *Geophys. J. Int*. **140**, 101 (2000).

[95] J. M. D. Coey, *Phys. Rev. Lett*. **27**, 1140, (1971).

[96] Yüksel Köseoğlu, *J. Magn. Magn. Mater.,* **300**, e327 (2006).

[97] A. E. Berkowitz, J. A. Lahut, I. S. Jacobs, L. M. Levinson, and D. W. Forester, *Phys. Rev. Lett.* **34**, 594(1975).

[98] C. Rablau, P. Vaishnava, C. Sudakar, R. Tackett, G. Lawes, and R. Naik, *Phys. Rev. E*, **78**, 051502 (2008).

[99] T.C. Halsey, and W. Toor, *Phys. Rev. Lett*. **65**, 2820 (1990)

[100] J. E. Martin, KM. Hill, and C.P. Tigges, Phys. Rev E, **59,** 5676 (1999)

[101] C. Rablau, P. Vaishnava, C. Sudakar, R. Tackett, G. Lawes, R. Naik, *Proceedings of SPIE*, **7032**, 70320Z (2008).

[102] A. S. Silva, R. Bond, F. Plouraboue, and D. Wirtz, *Phys. Rev. E,* **54**, 5502 (1996)

[103] S. Cutillas and J. Liu, *Phys. Rev., E* **64**, 011506 (2001)

[104] R. Toussaint, G. Helgesen, and E. G. Flekkoy, *Phys. Rev. Let*. **93**, 108304 (2004).

[105] F. Eeckman, A. J. Moes, K. Amighi, *J. Control. Release*, **88**, 105 (2003).

[106] D. C. Coughlan, F.P. Quility, O.I. Corrigan, *J. Control. Release*, **98**, 97 (2004).

[107] T. G. Park, A.S. Hoffman, *J. Biomed. Mater. Res.*, **24**, 21 (1990).

[108] M. A. Cooperstein and H. E. Canavan, *Langmuir, 26, 7695 (2010)*.

[109] M. Yamazaki, M. Tsuchida, K. Y. Kobayashi, T. Takezawa, Y. Mori, *Biotechnol. Bioeng.*, **44**, 38 (1994).

[110] G. Chen and A. S. Hoffman, *Nature*, **373**, 49 (1995).

[111] V. Nerapusri, J. L. Keddie, B. Vincent and I. A. Bushnak, *Langmuir,* **22***,* 5036 (2006).

[112] S. Juodkazis, N. Mukai, R. Wakaki, A. Yamaguchi, S. Matsuo Hiroaki Misawa, *Nature,* **408**, 178 (2000).

[113] H.G. Schild, *Prog. Polym. Sci.*, **17***,* 163 (1992).

[114] A. Gutowska, J. S. Bark, I. C. Kwon, Y. H. Bae, Y Cha, S. W. Kim, *J. Control. Release*, **48** ,141 (1997).

[115] C. S. Brazel, N. A. Peppas, *J. Control. Release*, **39**, 57 (1996).

[116] D. Muller-Schultea, T. Schmitz-Rodeb, *J. Magn. Magn. Mater.* **302**, 267 (2006).

[117] N. S. Satarkar, J. Z. Hilt, *Acta Biomaterialia*, **4,** 11 (2008).

[118] C. Liu, J. Guo, W. Yang, J. Hu, C. Wang and S. Fu, *J. Mater. Chem.*, **19**, 4764 (2009).

[119] T. Hoare, J. Santamaria, G. F. Goya, S. Irusta, D. Lin, S. Lau, R. Padera, R. Langer and D. S. Kohane, *Nanoletters*, **9**, 3651 (2009).

[120] S. Purushotham, P. E. J. Chang, H. Rumpel, I. H. C. Kee, R. T. H. Ng, P. K. H. Chow, C. K. Tan and R. V. Ramanujan, *Nanotechnology*, **20,** 305101 (2009).

[121] N. S. Satarkar, J. Z. Hilt, *J. Control. Release*, **130**, 246 (2008).

[122] S. R. Sershen, S. L. Westcott, N. J. Halas, J. L. West, *J. Biomed. Mater. Res.*, **51**, 293 (2000).

[123] E. M. Schopman, C. B. Van, P. J. Bakker, J. B. Kipp, G. W. Barendsen., *Int. J. Hyperthermia*, **12,** 241 (1996).

[124] M. Prevot, C. Déjugnat, H. Möhwald, and G. B. Sukhorukov, *ChemPhysChem* **7**, 2497 (2006).

[125] Yue Cui, Cheng Tao, Suping Zheng, Qiang He, Sufen Ai, Junbai Li, *Macromol. Rapid Commun.*, **26**, 1552 (2005).

[126] S. Kalele, R. Narain, K. M. Krishnan, *J. Magn. Magn. Mater.,* **321**, 1377 (2009).

[127] C. Sudakar, A. Dixit, R. Regmi, R. Naik, G. Lawes, V. M. Naik, P. P. Vaishnava, U. Toti and J. Panyam, *IEEE Trans. Magn.*, **44**, 2800 (2008).

[128] S. B. Field, *Phys. Med. Biol.*, **32**, 789 (1987).

[129] A. R. Gennaro, Remington: The Science and Practice of Pharmacy, 19th Ed., (1995)

[130] C. Thompson, Pharmaceutics (Part I) – Spring 2004

[131] C. Alexiou, W. Arnold, R. J. Klein, F. G. Parak, P. Hulin, C. Bergemann, W. Erhardt, S. Wagenpfeil and A. S. Lubbe, *Cancer Res.*, **60**, 6641 (2000).

[132] T.S. Herman, B.A. Teicher, A. Varshney, V. Khandekar, T. Brann, *Anticancer Res.*, **12**, 827 (1992).

[133] M. R. Saboktakin, R. M. Tabatabaie, A. Maharramov, M. A. Ramazanov, *Carbohydrate Polymers,* **80**, 695 (2010).

[134] M. Babincova, P. Sourivong, D. Chorvat, P. Babinec, J*. Magn. and Mag. Mater.*, **194**, 163 (1999).

[135] B. Perlstein, Z. Ram, D. Daniels, A. Ocherashvilli, Y. Roth, S. Margel, and Y. Mardor, *Neuro-Oncology,* **10**, 153 (2008).

[136] V. Polyakov, V. Sharma, J. L. Dahlheimer, C. M. Pica, G. D. Luker and D. Piwnica-Worms, *Bioconjugate Chem*. **11**, 762 (2000).

[137] E. L. Snyder, S. F. Dowdy, *Curr. Opin. Mol. Ther*. **3**, 147 (2001).

[138] I. H. Gul, A. Maqsood, *J. Alloys and Compd*., **465**, 227 (2008).

[139] R. Nasri, A. Siblini, L. Jorat and G. Noyel, *J. Magn. Magn. Mater.,* **161**, 309 (1996).

[140] G. Lawes, R. Tackett, B. Adhikary, and R. Naik, O. Masala and R. Seshadri, *Appl. Phys. Lett*., **88**, 242903 (2006).

[141] E. J. W. Verwey and E. L. Heilmann, *J. Chem. Phys*. **15**, 174 (1947).

[142] A. P. Ramirez, Annu. Rev. Mater. Sci. 24, 453 (1994).

[142] T.A. Kaplan, *Phys. Rev.* **116**, 888 (1959).

[143] T.A. Kaplan, K. Dwight, D. Lyons, N. Menyuk, *J. Appl. Phys*. **32**, 13S (1961)

[144] N. Menyuk, K. Dwight, D. Lyons and T. A. Kaplan, *Phys. Rev*. **127**, 1983 (1962).

[145] K. Dwight and N. Menyuk, *Phys. Rev*. **119**, 1470 (1960).

[146] G B Jensen and O V Nielsen, *J. Phys. C: Solid State Phys*. **7**, 409 (1974).

[147] B. Boucher, R. Buhl and M. Perrin, Journal of Applied Physics **42**, 1615(1971).

[148] R. Tackett, G. Lawes, B. C. Melot, M. Grossman, E. S. Toberer, and R. Seshadri, *Phys. Rev. B* **76**, 024409(2007).

[149] Takehito Suzuki and Takuro Katsufuji, *Phys. Rev. B,* **77**, 220402(2008).

[150] T. Ambrose and C. L. Chien, *Phys. Rev. Lett*. **76**, 1743(1995).

[151] Michael E. Fisher and Michael N. Barber, *Phys. Rev. Lett*. **28**, 1516 (1972).

[152] Oscar Iglesias and Amilcar Labarta, Phys. Rev. B **63**, 184416 (2001).

[153] Eric E. Fullerton, K. T. Riggs, C. H. Sowers and S. D. Bader and A. Berger, *Phys. Rev. Lett*. **75**, 330(1995).

[154] Lin He, Chinping Chen, Ning Wang, Wei Zhou, and Lin Guo, *J. Appl. Phys*. **102**, 103911 (2007).

[155] Susanthri C. Perera, Petru S. Fodor, Georgy M. Tsoi, Lowell E. Wenger, and Stephanie L. Brock, *Chem. Mater*. **15***,* 4034 (2003).

[156] P. Z. Si, D. Li, J. W. Lee, C. J. Choi, Z. D. Zhang, D. Y. Geng and E. Brück, *Appl. Phys. Lett.* **87**, 133122 (2005).

[157] A. E. Berkowitz, G. F. Rodriguez, J. I. Hong, K. An, T. Hyeon, N. Agarwal, D. J. Smith and E. E. Fullerton, *Phys. Rev. B* **77**, 024403 (2008).

[158] Y.Q. Chang, X.Y. Xu, X.H. Luo, C.P. Chen, D.P. Yu, *Journal of Crystal Growth,* **264**, 232 (2004).

[159] Y. F. Han, F. Chen, Z. Y. Zhong, K. Ramesh, E. Widjaja and L. W. Chen, *Catal. Commun.* **7**, 739 (2006).

[160] A. Millan, A. Urtizberea, N.J.O. Silva, F. Palacio, V.S. Amaral, E. Snoeck, V. Serin, *J. Magn. Magn. Mater.,* **312**, L5 (2007).

[161] R. H. Kodama and A. E. Berkowitz, E. J. McNiff, Jr. and S. Foner, *Phys. Rev. Lett.* **77**, 394 (1996).

[162] S. D. Tiwari and K. P. Rajeev, *Phys. Rev. B*, **72**, 104433 (2005).

[163] T. Jonsson, P. Nordblad, and P. Svedlindh, *Phys. Rev. B,* **57**, 497(1998)

[164] P. C. Fannin, C. N. Marin, I. Malaescu and N. Stefu, *J. Phys.: Condens. Matter.,* **19**, 036104 (2007).

[165] I. Malaescu and C. N. Marin, *J. Coll. Inter. Sci.,* **251**, 73 (2002).

[166]J. Snyder, J. S. Slusky, R. J. Cava and P. Schiffer, *Nature*, **413**, 48 (2001).

[167] C. Park, K. J. Kim, J. Gottschlich and Q. Leland, *Proceedings of IMECE'05*.

[168] K. Young, M.A. Fetcenko, T. Ouchi, F. Li, J. Koch, *J. Alloys Compd.* **469** (2009 406.

[169] R. Kikuyama, *Japan Patent Publication,* 2000-90920 (2000).

[170] A. N. Lassegne-Jackson, B. Mishra and D. L. Olsen, *Mater. Manuf. Processes* ,**22**, 433 (2007).

[171] F. Stucki and L. Schlapbach, *J. Less-Commun. Met.* **74**, 143 (1980).

[172] D. Shaltiel, I. Jacob, D. Davidov, *J. Less-Common Met.* **53**, 117 (1977).

[173] N. Honda, N. Furukawa, S. Fujitani, I. Yonezu, US Patent 4,913,879 (1990).

[174] M.Y. Song, D. Ahn, I.H. Kwon, S.H. Chough, *J. Electrochem. Soc.* 148, A1041 (2001).

[175] S. Ji, S. Li, J. Sun, *Chin. J. Rare Met.* **28**, 657 (2004).

[176] K. Young, T. Ouchi, B. Reichman, W. Mays, R. Regmi, G. Lawes, M.A. Fetcenko and A.Wuc, *J. Alloys Compd.* **489**, 202 (2010).

[177] T. Gamo, Y. Moriwaki, US Patent 4,946,646 (1990).

[178] S.Wakao, H. Sawa,M.Miyamura, H. Ishikawa, *J. Less-CommonMet.* **172–17**, 1211 (1991).

[179] Y. Yamamura, H. Seri, Y. Tsuji, T. Iwaki, US Patent 5,541,018 (1996).

[180] B. Reichman, W.C. Mays, K. Young, M.A. Fetcenko, S.R. Ovshinsky, T. Ouchi*, Electrochem. Soc. Proc.,* **98–15**, (1998) 111.

ABSTRACT

PROPERTIES AND BIOMEDICAL APPLICATIONS OF MAGNETIC NANOPARTICLES

by

RAJESH KUMAR REGMI

August 2011

Advisor: Dr. Gavin Lawes

Major: Physics

Degree: Doctor of Philosophy

Magnetic nanoparticles have a number of unique properties, making them promising agents for applications in medicine including magnetically targeted drug delivery, magnetic hyperthermia, magnetic resonance imaging, and radiation therapy. They are biocompatible and can also be coated with biocompatible surfactants, which may be further functionalized with optically and therapeutically active molecules. These nanoparticles can be manipulated with non-invasive external magnetic field to produce heat, target specific site, and monitor their distribution *in vivo*. Within this framework, we have investigated a number of biomedical applications of these nanoparticles. We synthesized a thermosensitive microgel with iron oxide adsorbed on its surface. An alternating magnetic field applied to these nanocomposites heated the system and triggered the release of an

anticancer drug mitoxantrone . We also parameterized the chain length dependence of drug release from dextran coated iron oxide nanoparticles, finding that both the release rate and equilibrium release fraction depend on the molecular mass of the surfactant. Finally, we also localized dextran coated iron oxide nanoparticles labeled with tat peptide to the cell nucleus, which permits this system to be used for a variety of biomedical applications.

Beyond investigating magnetic nanoparticles for biomedical applications, we also studied their magnetohydrodynamic and dielectric properties in solution. Magnetohydrodynamic properties of ferrofluid can be controlled by appropriate selection of surfactant and deielctric measurement showed magnetodielectric coupling in this system. We also established that some complex low temperature spin structures are suppressed in Mn_3O_4 nanoparticles, which has important implications for nanomagnetic devices. Furthermore, we explored exchange bias effects in Ni-NiO core-shell nanoparticles. Finally, we also performed extensive magnetic studies in nickel metalhydride (NiMH) batteries to determine the size of Ni clusters, which plays important role on catalyzing the electrochemical reaction and powering Ni-MH batteries.

AUTOBIOGRAPHICAL STATEMENT

NAME: Rajesh Kumar Regmi

EDUCATION:

Ph. D. (Physics): Wayne State University, Detroit, MI, 2011

M. S. (Physics): Wayne State University, Detroit, MI, 2008

M. Sc. (Physics): Tribhuvan University, Nepal, 2003

B. Sc. (Physical Science): Tribhuvan University, Nepal, 2001

PUBLICATIONS

1. **Rajesh Regmi**, Shanta Raj Bhattarai, Chandran Sudakar, Amit S. Wani, Robert Cunningham, Prem P. Vaishnava, Ratna Naik, David Oupicky and Gavin Lawes, Hyperthermia controlled rapid drug release from thermosensitive magnetic microgels, J. Mater. Chem., **20** (2010) 6158.

2. K. Young, B. Huang, **R. K. Regmi**, G. Lawes and Y. Liu, Comparisons of metallic clusters imbedded in the surface oxide of AB_2, AB_5, and A_2B_7 alloys, J. of alloys and compounds, **506** (2010) 831.

3. K. Young, **R. Regmi**, G. Lawes, T. Ouchi, B. Reichman, M.A. Fetcenko, A. Wu, Effects of aluminum substitution in C14-rich multi-component alloys for NiMH battery application, J. of Alloys and Compounds, **490** (2010) 282.

4. K. Young, T. Ouchi, B. Reichman, W. Mays, **R. Regmi**, G. Lawes, M.A. Fetcenko and A. Wu, Optimization of Co-content in C14 Laves phase multi component alloys for NiMH battery application, J. of Alloys and Compounds, **489** (2010) 202.

5. **Rajesh Regmi**, Correy Black, C. Sudakar, P. H. Keyes, Ratna Naik, G. Lawes, Prem Vaishnava, Cornel Rablau, David Kahn, Melissa Lavoie, Vijayendra K. Garg and A. C. Oliveira, Effects of fatty acid surfactants on the magnetic and magnetohydrodynamic properties of ferrofluids J. Appl. Phys., **106** (2009) 113902.

6. **R. Regmi**, R.Tackett and G. Lawes, Suppression of low-temperature magnetic states in Mn_3O_4 nanoparticles, J. Magn. Magn. Mater., **321** (2009) 2296.

7. Chandran Sudakar, Ambesh Dixit, **Rajesh Regmi**, Ratna Naik, Gavin Lawes, Vaman M. Naik ,Prem P. Vaishnava, Udaya Toti and Jayanth Panyam, Fe_3O_4 incorporated AOT-Alginate Nanoparticles for Drug Delivery, I. Trans. Magn. **44** (2008) 2800.